Ultrafast dynamics of intra- and intermolecular interactions in liquids and films

Salamatova, Evgeniia

Ultrafast Dynamics of Intra- and Intermolecular Interactions in Liquids and Films

Evgeniia Salamatova

2018

rijksuniversiteit
groningen

Zernike Institute PhD thesis series 2018-32

ISSN: 1570-1530

ISBN: 978-94-034-1107-1 (Electronic version)

ISBN: 978-94-034-1108-8 (Printed version)

The work presented in this thesis was performed in the Optical Condensed Matter Physics research group of the Zernike Institute for Advanced Materials at the University of Groningen in the Netherlands

Cover art: Julia Khoroshevskaya (original concept by Evgeniia Salamatova)

Printed by: Ipskamp printing

rijksuniversiteit
groningen

Ultrafast Dynamics of Intra- and Intermolecular Interactions in Liquids and Films

Proefschrift

ter verkrijging van de graad van doctor aan de
Rijksuniversiteit Groningen
op gezag van de
rector magnificus prof. dr. E. Sterken,
en volgens besluit van het College voor Promoties.

De openbare verdediging zal plaatsvinden op
vrijdag 26 oktober 2018 om 16.15 uur
door

Evgeniia Salamatova

geboren op 22 februari 1990
te Volgograd, Sovjet-Unie

Promotor

Prof. dr. M. S. Pchenitchnikov

Copromotor

Dr. T. L. C. Jansen

Beoordelingscommissie

Prof. dr. R. A. Hoekstra

Prof. dr. H. J. Bakker

Prof. dr. K. Wynne

To my Family

&

To my Mom

Contents

Chapter 1

General introduction

Intra- and inter-molecular interactions determine a number of dynamical properties such as energy transfer, vibrational relaxation and exciton diffusion, in bio- and energy-related materials. An understanding of these processes is indispensable for predicting more complex properties (e.g. hydrogen bonding and structural organization) as well as for designing new materials with desirable properties.

This chapter introduces a general explanation of intra- and intermolecular interactions and the molecular systems in which these are experimentally studied. It further presents an overview of the principles of ultrafast spectroscopic techniques, which are used for unraveling the intra- and intermolecular contributions in the studied systems.

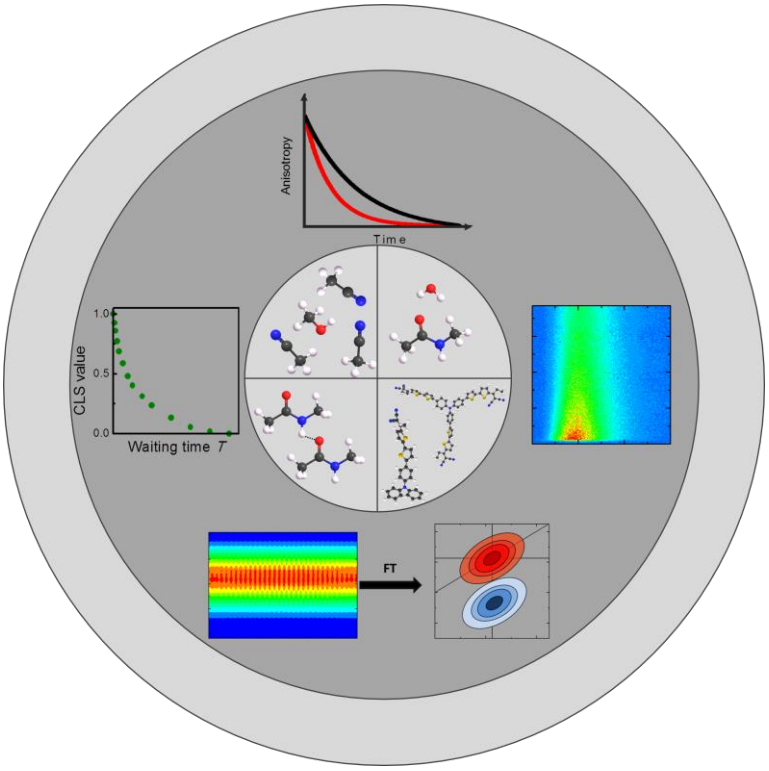

1.1 Intra- and Intermolecular interactions

On the molecular level, interactions can be characterized by their origin. Interactions between atoms within a single molecule or interactions between atoms in two (or more) molecules: intramolecular and intermolecular[1] (Figure 1.1). Both types of interactions control molecular and atomic movement thereby determining chemical, physical and dynamical properties of materials. Quite often, one of the two interactions plays a more essential role than the other in dynamical properties such as energy transfer[2–6], relaxation processes[5,7–10], exciton dynamics[11–14] etc.; other times, both are essential[13,15]. Therefore, it is important to understand the effect of intra- and/or intermolecular interactions on the chemical/physical as well as the dynamical properties of the materials.

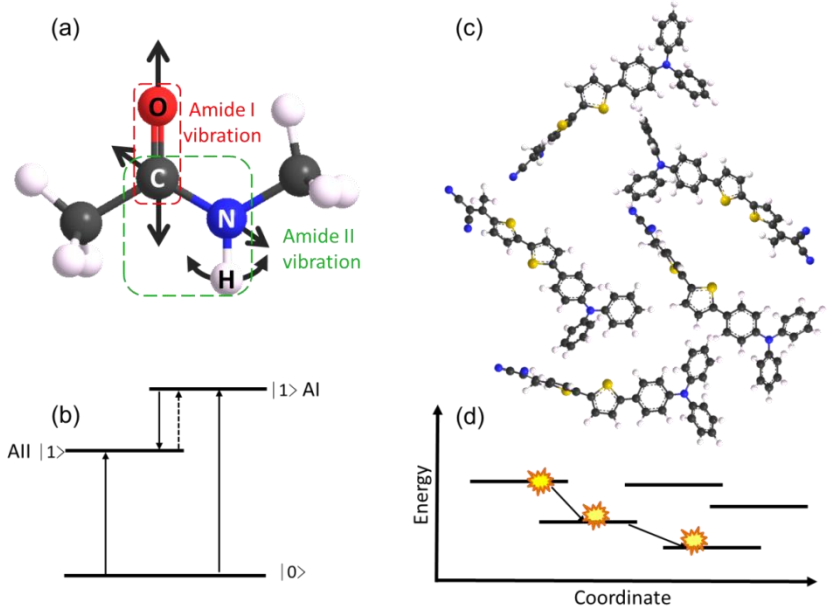

Figure 1.1 Schematic representation of (a) intramolecular interaction within N-methylacetamide molecule; amide I (CO stretching) and amide II modes (NH bending and CN-stretching) are highlighted by the red and green dashed boxes respectively; (b) schematic representation of the relaxation pathways between amide I and amide II modes within the peptide unit (detailed description can be found in Ref.16). (c) intermolecular interactions between small organic dye molecules TPA-2T-DCV-Me due to dense packing. (d) schematic representation of exciton (a delocalized electronic-hole pair[14]) diffusion due to intermolecular interactions in a densely packed film.

1.1.1 Intramolecular interactions

According to the classical definition, the intramolecular interactions occur within one molecule and exist between different atoms in a molecule as ionic, covalent

(both polar and nonpolar) and metallic bonds[17]. The intramolecular interactions determine the chemical behavior of a substance and they are typically much stronger than the intermolecular forces, resulting in stable molecules in well-defined configurations.

In the current Thesis the vibrational (Chapters 2-4) or electronic (Chapter 5) modes are of the primary interest. Vibrations interact with each other within one molecule[18–21] via potential anharmonicity ("through bond") as for example amide I and amide II modes[22–26] (Figures 1.1a and b), or "through" space as in small peptides/proteins[25,27]. Similarly, electronic wavefunctions that belong to different molecules, can be efficiently delocalized into exciton states or that can result in excitation transfer if the molecular states are near degenerate[28] (Figures 1.1c and d).

1.1.2 Intermolecular interactions

Intermolecular interactions are formed between individual molecules with the strongest interactions due to their charge distributions[17]. Intermolecular interactions determine not only the state of the matter (solid, liquid or gas) but also its photophysical properties, structural organization, and energy transfer between different molecules. Similarly to intramolecular interactions, the intermolecular interactions responsible for mixing of excited states can be approximated in terms of coupling of dipole moments (dipole-dipole interactions) of vibrational modes[29–32] (Chapters 2-4) or electronic wavefunctions[13,33,34] (Chapter 5).

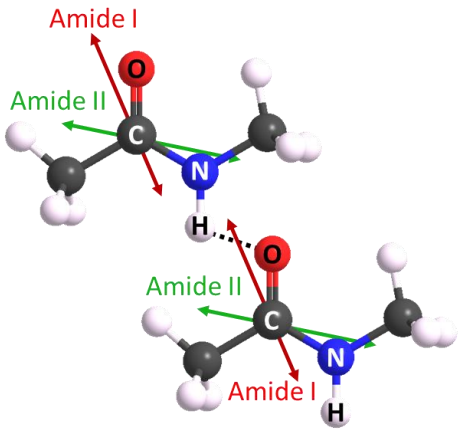

Figure 1.2 Schematic representation of dipole-dipole interactions between NMA molecules. The arrows show the transition dipoles which are associated with amide I (red arrow) and amide II modes (green arrow). The parameters of transition dipoles can be found in Ref.35.

1.1.3 Hydrogen bonding

Hydrogen Bonding (HB)[36] is a special kind of intermolecular interaction that occurs between specific atoms. HB is characterized by the interaction of hydrogen (H) in a polar bond and an electronegative atom: nitrogen (N), fluorine (F) or oxygen (O) (for example N-H, O-H, or F-H). A schematic representation of HB can be written as A-H···B or A-H···A, where are A and B represents an electronegative atom of O, N or F. These electronegative atoms have at least one lone pair, which facilitates the HB interactions. Different definitions of HB include geometric criteria involving various angles[37–39] (the classical one is the A-H···B angle) of HB; the length of the HB[40,41], and - more rigorously, but harder to determine - the binding energy[42,43]. The importance of HB in the structure and dynamics[31,44–46] of organic, inorganic, and hybrid materials promoted a great scientific interest in studying HB, using a variety of experimental techniques[47,48].

1.2 Intra- and Intermolecular Interactions in the Systems Under Study

1.2.1 Hydrogen bonding in biological systems

The first suggestion that HB plays a crucial role in peptide and protein structures dates back to 1936[49]. The discovery of α- helixes[50] and β-sheets[51], the high-resolution protein structure of myoglobin (1960) has shown that backbone HBs play a key role in peptides/protein structures. After obtaining the structure of myoglobin[52] the HB was described for many individual proteins in detail[26,53]. One of the basic HB group in proteins/DNA is the peptide unit (-CONH-), which is a part of the polypeptide chain. Therefore, the NH group can form one HB, acting as the HB donor, while the C=O group can accept up to two HBs, using the two lone pairs of oxygen.

The extensive studies of HB in proteins have shown that almost all of N-H and C=O groups tend to form HB. However, due to the bulky structure and high number of residues, which form intra- and intra-molecular HBs, the study of HB dynamical properties can be challenging. Simple molecules, for example, the small building blocks for the peptide linkage of polypeptides and proteins, can be used to overcome this complication. N-methylacetamide (NMA) is composed of a single peptide unit (Figure 1.3a) and can accept up to two HBs and donate up to two HBs. Therefore, an extensive HB network is formed between NMA-NMA and/or NMA-solvent molecules. Due to all these properties NMA is widely used in spectroscopic studies[30,54–62] as a simple model of the linkage between peptide units. Moreover, by varying the concentration of NMA molecules in a solution it becomes possible to

estimate the contribution of intra/intermolecular interactions to HB dynamics, energy transfer and structural properties.

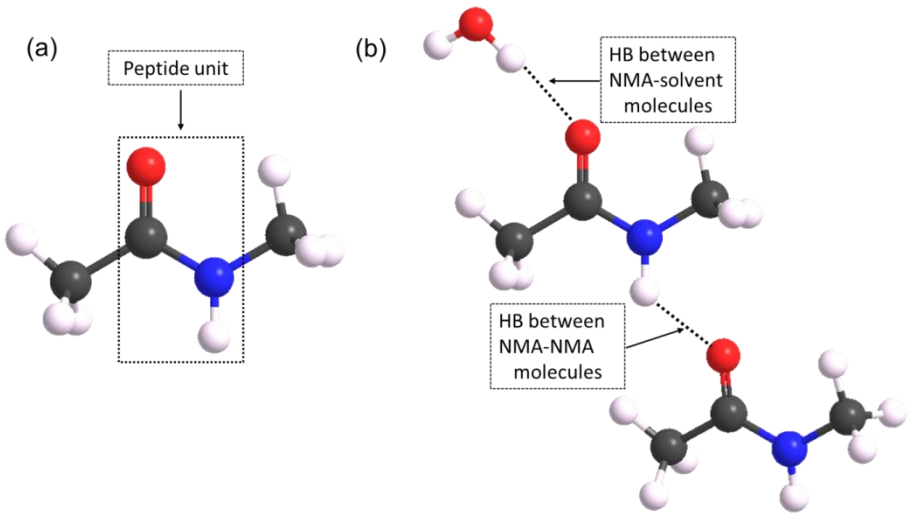

Figure 1.3 (a) NMA molecule, a single peptide unit is shown by the dashed box; (b) Schematic representation of HBs between NMA-NMA and NMA-solvent (as the solvent, a water molecule is considered) molecules.

1.2.2 Intra- and intermolecular HB in alcohols

An alcohol is any organic compound, containing one or more hydroxyl functional groups (-OH)[17], which is attached to the alkyl group R. Monoalcohols considered in this Thesis, form a sub-class of alcohols which has a general formula C_nH_{2n+1}-OH. In the alcohol molecules the OH group makes it possible to form an intermolecular HB between other alcohol molecules and a wide variety of polar solvents. There are several properties, which make the alcohols and solutions of alcohols very attractive for studying intermolecular HB dynamics by non-linear spectroscopy. Firstly, alcohol molecules are easily dissolved in a wide range of polar and non-polar solvents since the alcohol molecules contain both the polar (-OH) and non-polar groups (C_nH_{2n+1}). Secondly, the alcohol molecules accept up to two HBs and donate one. Therefore alcohol molecules do not form an extensive 3D HB network that is so characteristic for liquid water[63,64]. The balance between accepted/donated HBs in alcohols is the same as in NMA molecules (considered in the previous section), however, an important difference is that alcohol molecules do not contain peptide unit(s). Finally, the size and shape of alcohol molecules are easily varied by changing the length and branching of alkyl chain group.

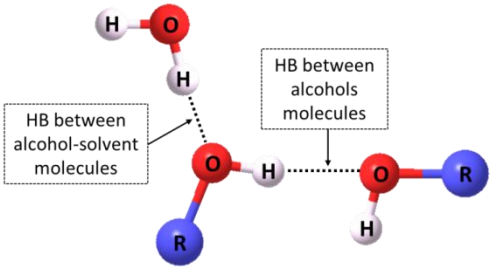

Figure 1.4 Schematic representation of intermolecular HBs which occur between alcohol and alcohol/solvent molecules

1.2.3 Intra- and intermolecular interactions in star-shaped molecules

Extensive chemical research resulted in the design of new molecules, which possess the desirable photophysical properties. Small molecules[14,65–68] (SMs) are attractive for their high purity, solubility, strong and broadband absorption coefficient which makes them a promising candidate for organic solar cell applications. Several extensive studies have been devoted to the star-shaped SMs (SSMs) that are based on a triphenylamine (TPA) core[13,14,69,70] (Figure 1.5a). The SSMs with their quasi-two-dimensional spatial structure[69] have been widely used in photovoltaics. The high symmetry of molecules leads to an increase in the pathways for light harvesting and due to their high symmetry, SSMs exhibit fascinating intramolecular photophysics[13,14]. Additionally, it was shown that the number of conjugated segments in the SSM arm influences the absorption band region, absorption coefficient and molecular orbital levels[71]. Therefore, intramolecular interactions are one of the keys to understanding the photophysical properties of the molecule. However, the weak intermolecular interactions such as π-π stacking, charge transfer, and van der Waals interactions play an important role as well, because they define the supramolecular architecture in solid films. Thus, it is crucial to understand how the structure of a designed molecule influences its physical and optical properties; how intra- and intermolecular interactions affect the charge/exciton dynamics in the SSM solid films.

The intra- and intermolecular photophysical characteristics of SSMs can easily be separated by studying them either in solid films or in diluted liquid/solid solutions, which extends the range of research methods available. Another possible approach to distinguish the intra- and intermolecular contributions is a chemical modification of the initial SSM (Figure 1.5b), which changes the molecular structure to a non-symmetric one. This result in diminished intramolecular interactions.

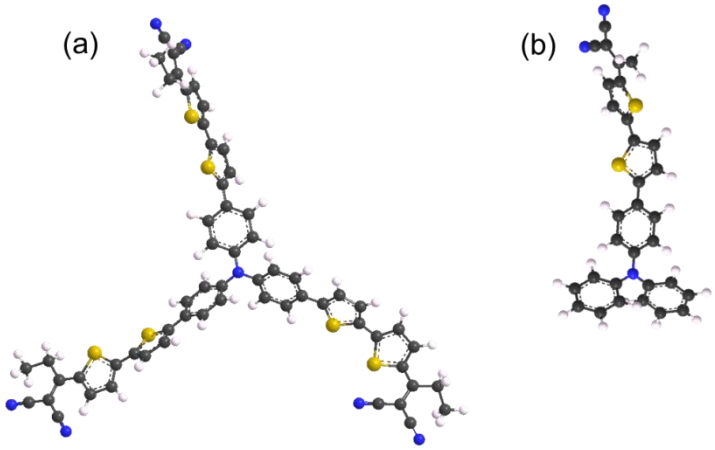

Figure 1.5 (a) An SSM molecule with the TPA core donor and dicyanovinyl acceptor end groups[13] and (b) its linear analogue[72].

1.3 Goals and Objectives of the Thesis

The current Thesis is devoted to a study of ultrafast dynamical processes, which occur in bio- and energy-related materials due to intra- and intramolecular interactions. The Thesis aims to provide an answer to the following question: what kind of interaction – intra- and/or intermolecular – mostly influences (or even determines) ultrafast dynamical properties (such as HB dynamics, energy transfer, exciton diffusion) in different materials.

To reach this goal, the following objectives are posed:

1) To evaluate energy transfer (Chapters 2) and exciton diffusion (Chapter 5) dynamics in condensed phase systems

2) To identify the difference in energy transfer pathways and dynamical properties between a homogeneous system (Chapter 2) in comparison with a heterogeneous system (Chapter 3)

3) To compare contributions of intramolecular interactions (Chapters 4 and 5) and intermolecular interactions (Chapters 2,3, and 5) to the following bulk systems: NMA (Chapters 2, 3) and SSMs (Chapter 5).

4) To demonstrate the importance of intermolecular interactions for HB dynamics by considering a strongly diluted system, where the intermolecular interactions are negligibly weak (Chapter 4)

To fulfill these objectives, time-resolved IR and visible spectroscopy were used as experimental tools. Their general description is given in the next Section.

1.4 Infrared Spectroscopy

The first detection of the infrared radiation[73] can be considered as a starting point of infrared (IR) spectroscopy. Generally speaking, infrared spectroscopy is the study of the interaction of matter with IR light. Infrared light has three well-defined regions: near infrared (13000-4000 cm^{-1}), mid-infrared (4000-400 cm^{-1}) and far-infrared (400-100 cm^{-1})[74]. The mid-IR region is widely used because molecules (both organic and inorganic) have the functional groups, which absorb light in this region. Therefore, the spectral features, which are characteristic for different vibrational modes makes it possible to obtain information about functional chemical groups. As a result of this, the linear and non-linear spectroscopic techniques based on IR are widely used for revealing the structures of the chemical compounds. Moreover, the time-resolved methods[75-77] provide information about bond dynamics occurring in the studied sample.

1.4.1 Linear spectroscopy

Linear IR spectroscopy is a technique based on the fact that chemical bonds inside a molecule absorb the energy of resonant photons (Figure 1.6). The most common method of obtaining the linear spectrum consists of passing the IR radiation through a sample and determining the fraction of the incident light transmitted/absorbed at a specific wavelength. The output is an absorption/transmission spectrum, where each peak (or band) corresponds to a specific vibration of the molecule[74].

Linear IR spectroscopy provides a lot of information about molecular composition through the vibrational frequencies. However, linear spectroscopy is a steady-state technique, which is not helpful in understanding dynamical processes, which occur in the system after the absorption of the IR light. To obtain such dynamical properties, non-linear methods are needed.

1.4.2 Time-resolved non-linear IR spectroscopy

Time-resolved non-linear spectroscopy provides information about the dynamics of the system via the temporal evolution of the spectrum after initial excitation. The use of short light pulses leads to a high temporal resolution of the system evolution. In the current thesis, ultrashort femtosecond (1 fs=10^{-15} s) laser pulses with a duration of ~100 fs are used[78], which allows one to track the system dynamics at sub-ps time scales.

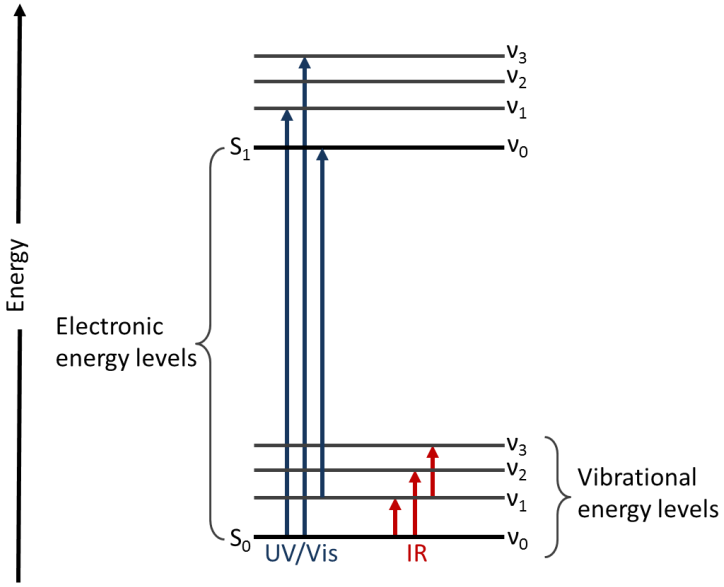

Figure 1.6 Energy levels diagram of a molecule, where S_n denotes the electronic energy level and V_n states for vibrational energy levels. The absorption of IR light (red arrows) leads to the vibration of chemical bonds. The absorption of UV/visible light causes an electron to move from ground state to higher energy level.

1.4.3 Time-resolved pump-probe spectroscopy

One of the most widely used time-resolved IR techniques is pump-probe spectroscopy. A schematic representation of the experimental setup is shown in Figure 1.7a[79]. The pump and probe pulses should have a spectrum which covers absorption lines of interest in the vibrational manifold.

The first intense pulse (the pump, the bold red arrow at the energy level diagram, Figure 1.7b) is used to bring the system to a non-equilibrium state by exciting a portion of the molecules from the ground state to first excited state. After the excitation, these molecules do not absorb light at the frequency of excitation any longer while the already-excited molecules can be stimulated to emit a photon; as the result, bleaching/stimulated emission appears at the frequency of |0>-|1> transition (the red-colored trace in Figure 1.7c). At the same time, the transition of the excited molecules from the first excited state to higher-lying states becomes possible, thereby producing an induced absorption signal (the blue-colored trace in Figure 1.7c). The frequency of the |0>-|1> transition is higher than the |1>-|2> transition due to anharmonicity so that the excited-state absorption can be readily separated from the bleaching/stimulated emission (and the anharmonicity value can also be obtained). The pump-probe signal decays with the increase in delay

time between the pump and probe pulses. The processes which lead to the signal decay include population relaxation, reorientation of molecules, and energy transfer. Therefore, the pump-probe signal contains contributions from different dynamical processes whence spectral-temporal characteristics may be retrieved.

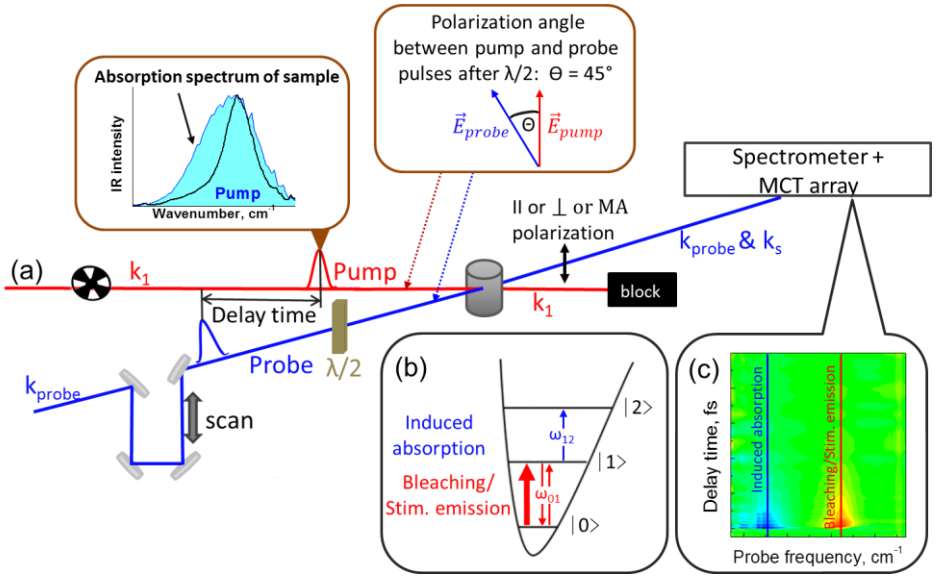

Figure 1.7 (a) Schematic representation of the pump-probe experimental setup. The polarizer after the sample selects the parallel, perpendicular or magic angle polarization component of the signal. (b) Three-level energy diagram of a vibrational mode. The first intense pulse (thick red arrow) transfers a part of the population from |0> ground state to a |1> excited state. The delayed probe pulse detects the bleaching/stimulated emission (the thin red arrows) at ω_{01} frequency or excited state absorption at frequency ω_{12} (blue arrow). (c) The resulting pump-probe signal where red and blue colors correspond to bleaching/induced absorption and induced absorption, respectively.

To exclude the contribution of molecular reorientation to relaxational dynamics, the time evolution of the so-called isotropic response should be obtained[80]. One of the methods to obtain the isotropic response $I_{iso}(t)$ is the polarization-resolved pump-probe measurements. $I_{iso}(t)$ can be constructed from parallel and perpendicular components of the pump-probe signal by the equation[80]:

$$I_{iso}(t) = \frac{I_{\parallel}(t) + 2 \cdot I_{\perp}(t)}{3} \qquad \text{(Eq. 1.1)}$$

where $I_{\parallel}(t)$ and $I_{\perp}(t)$ are the components of the probe, polarized parallel and perpendicular with respect to the pump, respectively. An alternative, but equivalent, approach to obtain the isotropic pump-probe signal is to use the 'magic angle' orientation between polarizations of the pump and probe pulses. In the

approximation of a single-dipole, isotropic three-dimensional distribution, the magic angle equals to 54.7° [81].

The second fundamental process which contributes to the decay of pump-probe signal is reorientation of the molecules (Figure 1.8a). Due to rotational diffusion the transition dipole orientation of the initially excited molecules changes in time, and therefore the pump-probe signal decays. The timescales of reorientational dynamics can be extracted from time-dependent anisotropy *r(t)*[80]*:*

$$r(t) = \frac{I_{\parallel}(t) - I_{\perp}(t)}{I_{\parallel}(t) + 2 \cdot I_{\perp}(t)} \qquad \text{(Eq. 1.2)}$$

where the population relaxation component is factorized out. Most of the liquids (Chapters 2-4) are characterized by high orientational disorder, which in turns leads to the anisotropy decay (Figure 1.8b).

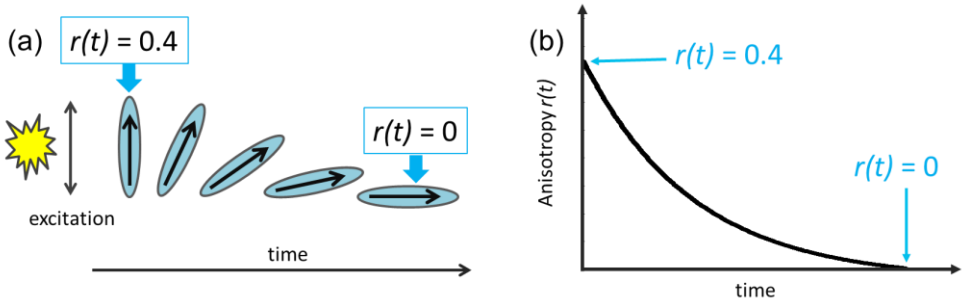

Figure 1.8 Schematic representation of rotational anisotropy decay in liquids

However, molecular reorientations are not the only factors that contribute to the anisotropy decay. When the molecules under study interact, the excitation could be transferred from one molecule to another due to dipole-dipole coupling, giving rise to intermolecular energy transfer[3,6,82] (Figure 1.9). The acceleration of the anisotropy decay is attributed to the fact that the energy transfer occurs from the preferentially excited vibrations to a molecule with random orientation[3,4,6,83]. The dipole-dipole interactions will be promoted in close packing of the molecules, e.g. in (concentrated) solutions or solid films. The energy transfer could also be mediated by HB, which keeps the distances between the vibrational oscillators short and may even maintain their mutual orientations[3,6,82].

A number of important dynamical properties of the system can be extracted from the pump-probe experiments. However, as was discussed above, the pump-probe spectrum is determined by a combination of many processes (e.g. population relaxation, reorientational dynamics, intermolecular energy transfer).

Therefore, it is crucial to separate all these processes from each other. Each Chapter of this Thesis concerns one or few processes, which occur in a given system under study, and the methods for extracting the timescales are discussed in detail. In this regard, the assignments of timescales and the very interpretation of the molecular processes call for close collaboration with theory such as molecular dynamics and spectral simulations.

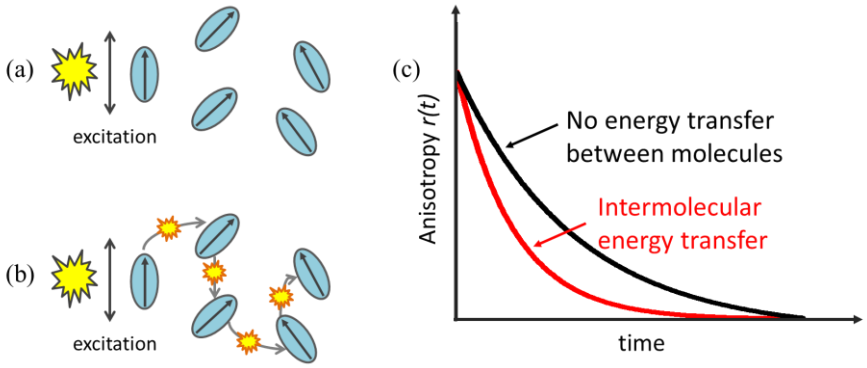

Figure 1.9 Schematic representations of the systems (a) without and (b) with intermolecular energy transfer. (c) Comparison of the transient anisotropy in the two systems, where intermolecular energy transfer does not occur (black line) and does occurs (red line). The decay of anisotropy in the system with intermolecular energy transfer accelerates as the result of energy transfer between differently-oriented dipoles.

1.4.4 2D spectroscopy

Linear spectroscopy provides static information about the |0>-|1> transitions, the pump-probe spectroscopy provides the timescales of relaxation and rotational dynamics. However, disentangling the information on, for instance, the coupling of different modes (e.g., chemical exchange), local environment fluctuations and HB rearrangement is not straightforward and typically requires multiple pump-probe experiments with a number of different pump frequencies. 2D-IR spectroscopy[75-77] is convenient and the easiest way to unravel the underlying information.

As was mentioned above, 2D-IR can be considered as a series of the pump-probe experiments[83] with many different excitation spectra, thereby providing spectral resolution along two frequency axis – one for the pump and another for the probe. While the probe frequency axis is naturally delivered by a spectrally-resolved probe, the easiest way to obtain the pump frequency axis is to use two pump pulses. By varying the time delay between these pulses, their interference pattern is imposed on the system excitation. The Fourier transform of this interference pattern provides the frequency axis of the pump.

For the 2D-IR experiments, the so-called “pump-probe” geometry (with two collinear pump and one probe pulse) is used (Figure 1.10). The pump frequency dimension (excitation frequency, ω_1) is obtained by varying the coherence time τ between two pump pulses. The system is allowed to evolve for a given waiting time T between the probe and one of the pumps. To obtain the probe frequency dimension ω_3, the spectrum of the probe pulse after the sample, is recorded. The real part of the Fourier transform over the coherence time provides the ω_1-dimension thereby producing the purely absorptive 2D spectra.

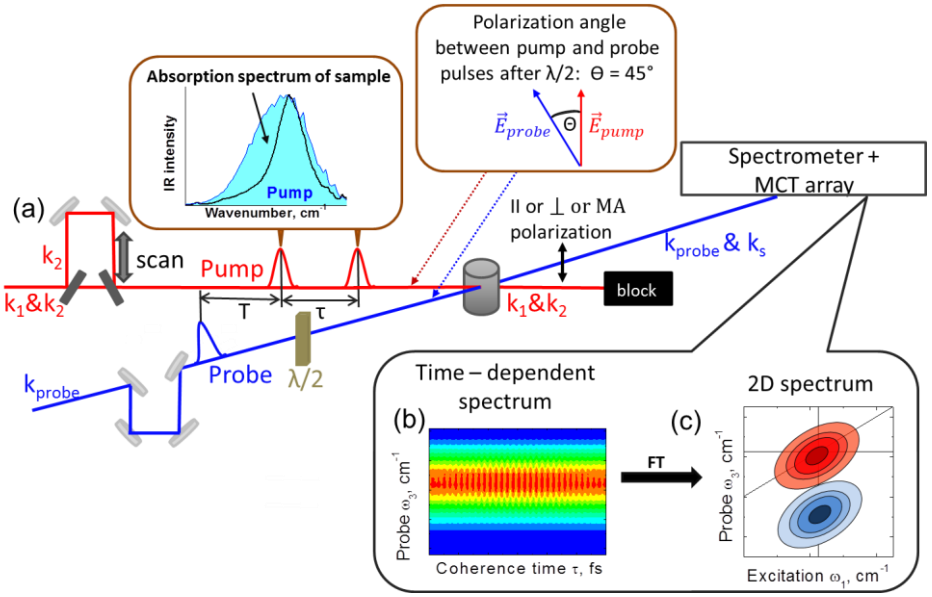

Figure 1.10 (a) Layout of 2D-IR setup in the pump-probe geometry. The probe frequency ω_3 is measured with a multichannel spectrometer. (b) The excitation frequency ω_1 is obtained from the Fourier transform over the coherent time τ the time-dependent spectrum, which contains the information about spectral fluctuations. (c) The 2D-IR spectrum obtained using a vibrational mode consists of bleaching/stimulated emission (|0>-|1> transition, red color) and induced absorption ((|1>-|2> transition, blue color) peaks; an energy level diagram is like the one in Figure 1.7)

One of the powerful features of 2D spectroscopy is the retrieval of dynamical information from the temporal frequency fluctuations of the reporter mode[75,84]. Given short waiting times, the correlation between the initial excitation of the system and its response is strong, i.e. the excitation and detection frequencies of the oscillators match very well. The result is that the 2D-IR spectrum has a diagonally elongated shape (Figure 1.11a). With the increase in waiting time, the local environment imposes fluctuations onto the system thereby changing its oscillation frequency. The correlation decreases, which results in evolving the spectral shape toward a more rounded one (Figure 1.11b). Given very long waiting

times, the correlation disappears completely, and the 2D-IR spectrum acquires a round shape (Figure 1.11c).

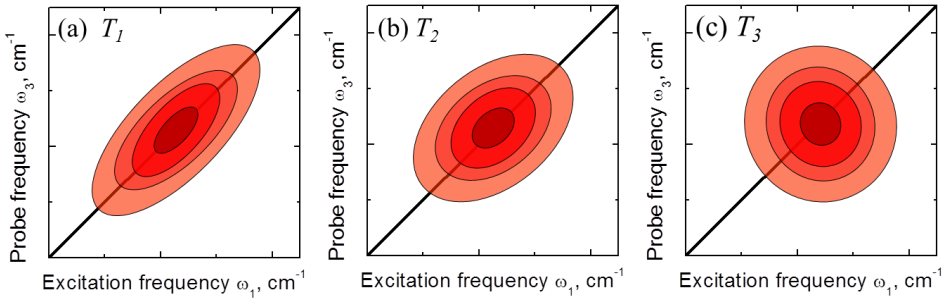

Figure 1.11 Evolution of a 2D-IR spectrum shape with increasing of waiting time *T*. (a) the diagonal elongation indicates strong correlation between excitation and probed frequencies. (b) as the system evolves in time, its frequency is randomized, and the shape becomes less elliptical; (c) the correlation is completely lost; the spectrum has a round shape.

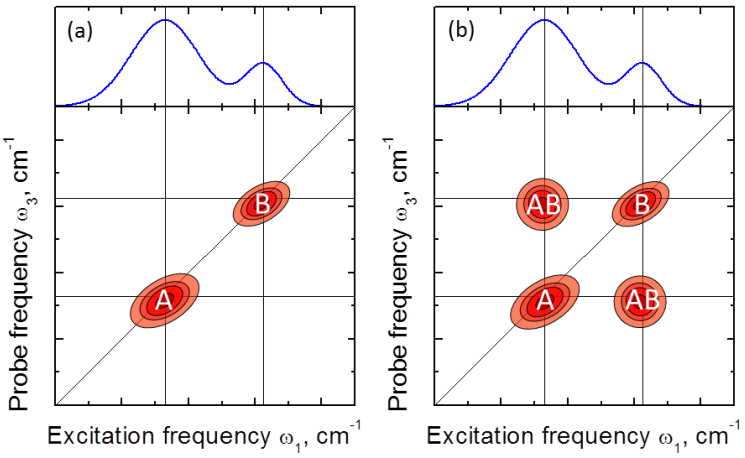

Figure 1.12 Schematic representation of a 2D-IR spectrum of (a) two uncoupled vibrational modes, (b) two coupled modes. Due to the coupling the cross-peaks AB appear. For the sake of simplicity, the induced absorption peaks are not shown.

Another powerful feature of 2D spectroscopy is the information on the coupling between vibrational modes within the studied system. The 2D spectrum consists of so-called diagonal peaks (A and B, Figure 1.12a), where the central frequencies of the peaks coincide with the central frequencies of the absorbing modes. If two or more modes are coupled, their interaction is easily detected because cross-peaks arise (AB, Figure 1.12b). One of the easiest explanations of the cross-peak occurrence due to coupling is two pendulums (oscillators) connected via a spring (electronic density). When we excite one of the oscillators, the other oscillator starts to move as well. The strength of the coupling determines the amplitude of the

cross-peak signal. Vary the waiting time *T* of the spectral shape, and signal intensities of the peaks evolve. These changes contain important information about the local environment of the respective vibrational mode.

1.4.5 Frequency-frequency correlation function and Center Line Slope analysis

The temporal evolution of 2D-IR spectra (Figure 1.11) contains information about the spectral diffusion (e.g. structural evolution of the system, environmental dynamics etc.)[85]. The spectral diffusion can be quantified[86] from the temporal evolution of the frequency-frequency correlation function (FFCF)[86]. However, the direct retrieval of the FFCF from the 2D-IR spectra is complex as it involves multiparameter nonlinear fitting optimization[85,87,88]. The computational complexity promoted the development of simpler methods, which allowed one to obtain the function directly from the experimental data. A large number of methods, such as the inverse centerline slope[85], the 2D Gaussian correlation[89], nodal line slope[30,90,91], an analysis of the ellipticity[80,88,92–94], inhomogeneous index[95] and Center Line Slope (CLS)[86,96] analysis were designed; all of them approximate and each of them having their own advantages and disadvantages[97].

One of the easiest methods for analyzing the experimentally measured 2D-IR spectra is CLS analysis. CLS at time *T* is defined as the slope of the line that connects maxima $\omega_{3,max}$ of ω_1 cuts of the 2D spectrum, as a function of ω_1:

$$CLS|_T = \left.\frac{\partial \omega_{3,max}}{\partial \omega_1}\right|_T \qquad \text{(Eq. 1.3)}$$

The CLS function represents the FFCF fairly well[98]. The slope values vary in the range from 1 (for a system with perfect correlation between excitation and probe frequencies, Figure 1.11a) to 0 (a system with no correlation, Figure 1.11c). CLS is not significantly influenced by a small value of anharmonicity shift, which in turn can lead to the distortion of the band shapes[86,97]; CLS is not affected by solvent background absorption[86]. In the scope of this Thesis, I considered the CLS analysis for extracting quantitative information from the spectral dynamics derived from the experimental 2D-IR spectra. The quality of the extracted FFCF can be validated by performing the same procedure on the corresponding theoretical data, where the FFCF can be readily calculated directly as well.

Figure 1.13 illustrates the algorithm of obtaining the CLS value from 2D-IR spectrum over a given waiting time *T*. At each value of excitation frequency ω_1 a slice (Figure 1.13a, thick vertical black line) is taken through the 2D spectrum. Each slice is a spectrum (Figure 1.13b, blue circles) which has a maximum $\omega_{3,max}$ frequency (Figure 1.13b). This procedure repeats for a desirable range of ω_1

frequencies (Figure 1.13a, thick grey lines). The curve which connects the resulting (ω_1;$\omega_{3,max}$) points (Figure 1.13a, blue dots) is the "center line" (Figure 1.13a, thick black curve). The resulting center line is fitted with a linear function over ω_1 frequencies; the particular range depends on a system (Gaussian or non-Gaussian)[98].

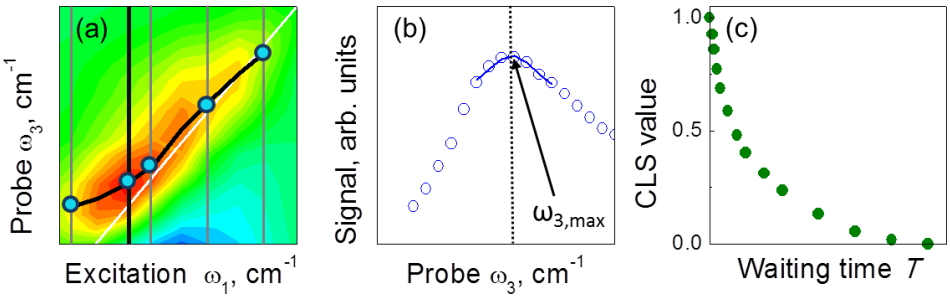

Figure 1.13 An illustration of the algorithm for extracting the CLS from a 2D-IR spectrum. (a) 2D-IR spectrum over a given waiting time T with superimposed center line (thick black curve); the black and grey lines correspond to a spectrum slices at different excitation frequencies; blue dots show (ω_1; $\omega_{3,max}$) points. (b) Spectrum of a "sliced" 2D-IR spectrum with denoted maximum $\omega_{3,max}$ frequency. (c) The temporal evolution of CLS values.

1.5 UV/Vis Spectroscopy and Time-Resolved Photoluminescence

In the previous Sections vibrational transitions were considered. Electronic transitions (Figure 1.6) occur when a molecule absorbs ultraviolet and visible (UV/Vis) light. The spectra of the electronic transitions contain important information about such simple optical properties[99] as the energy bandgap. Furthermore, one of the most powerful advantages of UV/Vis spectroscopy is its ability to unravel electron dynamics. For instance, in molecules with donor and acceptor groups the electronic transitions are accompanied by intramolecular and/or intermolecular energy transfer.

Similar to linear absorption experiments in the IR region, the steady-state absorption and photoluminescence (PL) spectra typically do not provide any dynamical information. In order to obtain this kind of information, time-resolved spectroscopy is used[100]. The approach, which allows tracking the evolution of PL signal in time, is called time-resolved PL spectroscopy. In the current Thesis, the time-resolved PL spectroscopy is used to determine timescales of intra- and inter-molecular energy migration in small molecules.

1.6 Scope of the Thesis

In the current Thesis, the dynamical properties of liquids and solid films are studied by ultrafast spectroscopy. It is shown that molecules with a single peptide unit (-CONH-) form well-organized structures that promote intermolecular energy transfer; this is atypical for liquids since liquids tend to be disordered. If such molecules are dissolved in water, the energy migration between molecules is largely unaffected but the molecules begin to experience a hydrophobic collapse. Similarly, spectroscopy on diluted alcohols demonstrates that the dynamical properties of bulk alcohols are determined by intermolecular interactions while the intramolecular ones play a minor role. In contrast, for solid films of organic photovoltaic materials, both intra- and intermolecular interactions are crucial for energy transfer and exciton dynamics.

The main findings of this Thesis are the following:

1) NMA molecules tend to form well-organized structures even in the liquid phase, which is very atypical for the liquid phase.
2) In water-NMA mixtures, a hydrophobic collapse is observed which suggests that this is an intrinsic property of the amino acid backbone units.
3) The HB dynamics of strongly dissolved linear alcohol molecules are similar for a wide range of alkyl group sizes.
4) The high symmetry of small star-shaped molecules promotes ultrafast intramolecular energy transfer, while the intermolecular energy transfer is almost independent of the molecular structure.

The thesis consists of 5 chapters, including this general introduction (Chapter 1). Each chapter considers a system in which *intra*- or/and *inter*-molecular interactions are studied with linear and/or non-linear spectroscopy.

In Chapter 2, the bulk liquid N-methylacetamide (NMA) is studied by 2D-IR spectroscopy. NMA is chosen as a model system for peptides and proteins due to its convenient properties such as i) NMA contains a single peptide unit (-CONH), and ii) NMA forms intermolecular HBs. Through a comparison of the linear and non-linear (2D) IR spectra obtained experimentally, with the results of spectral and molecular dynamical simulations, I unravel the most abundant NMA species, which appeared to be chains of HB NMA molecules. Diffusion of vibrational excitations between NMA molecules is determined from a comparison of experimental anisotropy decay with theoretical rotational correlation function and population transfer function. Although NMA is a liquid, NMA molecules tend to form well-aligned chains via intermolecular HBs. In turn, such a structure facilitates the

diffusion of vibrational excitation along these ordered chains instead of random migration thereby retaining orientations of transient dipoles

Chapter 3 extends the study of NMA to a more realistic model of biological systems, NMA-water mixtures. The NMA-water mixture is studied by 2D-IR spectroscopy combined with molecular dynamical-spectral simulations. In a striking contrast to hydrogen-bonded chains of NMA molecules in condensed phase, the NMA molecules in the mixture tend to form clusters. Biological systems show a similar behavior, when a polypeptide interacts with a polar solvent; the polypeptide tends to form an energetically favorable structure as a cluster with a hydrophobic core and a hydrophilic surface (the so-called "hydrophobic collapse"). Calculated radial distribution functions of pure NMA, water, and NMA-water samples confirm the occurrence of the “hydrophobic collapse” in such a simple system.

In Chapter 4, the contribution of *intra*molecular interactions to the hydrogen bonding (HB) dynamics in strongly diluted primary, secondary and tertiary alcohols are discussed. Previous studies of bulk alcohols where both intramolecular and intermolecular interactions exist showed a strong dependence of HB dynamics on the size of the alkyl chain group. Here, the alcohol molecules are strongly diluted in a polar solvent (acetonitrile) to avoid clusterization of the alcohol molecules and thereby to exclude the effect of intermolecular interactions. The HB dynamics are investigated by pump-probe and 2D-IR spectroscopy on the OH stretching mode and supported by theoretical spectral calculations. All studied alcohols show similar vibrational lifetimes of the OH stretching mode and similar HB dynamics, which is described by the fast (~200 fs) and slow components (~4 ps). The sharp contrast with the bulk alcohols, where both intra- and intermolecular interactions take place, suggests that in the bulk alcohols the difference in dynamics originates from intermolecular interactions.

Chapter 5 concerns intra- and intermolecular contributions to exciton dynamics in densely packed films of linear and star-shaped small molecules. These molecules have recently attracted great interest due to their application in photovoltaic devices, in particular, in organic solar cells. Two different molecules were studied: a star-shaped molecule N(Ph-2T-DCV-Et)$_3$ with a symmetric structure and its single-arm analogue TPA-2T-DCV-Me with a non-symmetric structure. In the former, the excitation energy is redistributed within the molecule via intramolecular interactions while in the former such a process is not present. To control the intermolecular coupling as a function of distance, the molecules were dissolved in a solid matrix at different concentrations, and their time and polarization-resolved photoluminescence was measured. Both molecules demonstrated similar trends at shorter intermolecular distances: i) the population

relaxation accelerates due to self-quenching; ii) the transient anisotropy speeds up due to Förster-like intermolecular energy transfer. The only but substantial difference between the molecules is that the anisotropy of the star-shaped molecules is rapidly (faster than the experimental resolution) scrambled even at long distances due to high molecular symmetry.

1.7 References

(1) Chang, R. *Chemistry*; McGraw-Hill Companies: New York, 2009.

(2) Asbury, J. B.; Steinel, T.; Fayer, M. D. Hydrogen Bond Networks: Structure and Evolution after Hydrogen Bond Breaking. *J. Phys. Chem. B* **2004**, 108, 6544–6554.

(3) Piatkowski, L.; Eisenthal, K. B.; Bakker, H. J. Ultrafast Intermolecular Energy Transfer in Heavy Water. *Phys. Chem. Chem. Phys.* **2009**, 11, 9033–9038.

(4) Cowan, M. L.; Bruner, B. D.; Huse, N.; Dwyer, J. R.; Chugh, B.; Nibbering, E. T. J.; Elsaesser, T.; Miller, R. J. D. Ultrafast Memory Loss and Energy Redistribution in the Hydrogen Bond Network of Liquid H2O. *Nature* **2005**, 434, 199–202.

(5) Cringus, D.; Bakulin, A.; Lindner, J.; Vöhringer, P.; Pshenichnikov, M. S.; Wiersma, D. A. Ultrafast Energy Transfer in Water - AOT Reverse Micelles. *J. Phys. Chem. B* **2007**, 111, 14193–14207.

(6) Woutersen, S.; Bakker, H. J. Resonant Intermolecular Transfer of Vibrational Energy in Liquid Water. *Nature* **1999**, 402, 507–509.

(7) Shinokita, K.; Cunha, A. V.; Jansen, T. L. C.; Pshenichnikov, M. S. Hydrogen Bond Dynamics in Bulk Alcohols. *J. Chem. Phys.* **2015**, 142, 212450.

(8) Bakulin, A. A.; Pshenichnikov, M. S.; Bakker, H. J.; Petersen, C. Hydrophobic Molecules Slow Down the Hydrogen-Bond Dynamics of Water. *J. Phys. Chem. A* **2011**, 115, 1821–1829.

(9) Hunger, J.; Buchner, R. Femto- to Nanosecond Dynamics in Ionic Liquids: From Single Molecules to Collective Motions; 2016; pp 53–71.

(10) Lock, A. J.; Gilijamse, J. J.; Woutersen, S.; Bakker, H. J. Vibrational Relaxation and Coupling of Two OH-Stretch Oscillators with an Intramolecular Hydrogen Bond. *J. Chem. Phys.* **2004**, 120, 2351–2358.

(11) Luponosov, Y. N.; Min, J.; Solodukhin, A. N.; Chvalun, S. N.; Ameri, T.; Brabec, C. J.; Ponomarenko, S. A. Design of Low Band Gap Small Molecules with Alkyldicyanovinyl Acceptor and Different Donor Groups for Efficient Bulk Heterojunction Organic Solar Cells. *SPIE Org. Photonics+ Electron.* **2015**, 9567, 95670W–95670W.

(12) Ni, W.; Li, M.; Liu, F.; Wan, X.; Feng, H.; Kan, B.; Zhang, Q.; Zhang, H.; Chen, Y. Dithienosilole-Based Small-Molecule Organic Solar Cells with an Efficiency over 8%: Investigation of the Relationship between the Molecular Structure and Photovoltaic Performance. *Chem. Mater.* **2015**, 27, 6077–6084.

(13) Kozlov, O. V; Liu, X.; Luponosov, Y. N.; Solodukhin, A. N.; Toropynina, V. Y.; Min, J.; Buzin, M. I.; Peregudova, S. M.; Brabec, C. J.; Ponomarenko, S. A.; et al.

Triphenylamine-Based Push-Pull Molecule for Photovoltaic Applications: From Synthesis to Ultrafast Device Photophysics. *J. Phys. Chem. C* **2017**, 121, 6424–6435.

(14) Kozlov, O. V; Luponosov, Y. N.; Ponomarenko, S. A.; Kausch-Busies, N.; Paraschuk, D. Y.; Olivier, Y.; Beljonne, D.; Cornil, J.; Pshenichnikov, M. S. Ultrafast Charge Generation Pathways in Photovoltaic Blends Based on Novel Star-Shaped Conjugated Molecules. *Adv. Energy Mater.* **2015**, 5, 1401657.

(15) Baiz, C. R.; Reppert, M.; Tokmakoff, A. Introduction to Protein 2D IR Spectroscopy. In *Ultrafast Infrared Vibrational Spectroscopy*; Fayer, M. D., Ed.; Taylor & Francis: New York, 2013; pp 361–404.

(16) Piatkowski, L.; Bakker, H. J. Vibrational Relaxation Pathways of Amide I and Amide II Modes in N -Methylacetamide. *J. Chem. Phys.* **2012**, 136, 164504.

(17) Chang, R. *General Chemistry*; New York, 2011.

(18) Buck, U.; Huisken, F. Infrared Spectroscopy of Size-Selected Water and Methanol Clusters. *Chem. Rev.* **2000**, 100, 3863–3890.

(19) Cringus, D.; Bakulin, A.; Lindner, J.; Vöhringer, P.; Pshenichnikov, M. S.; Wiersma, D. A. Ultrafast Energy Transfer in Water - AOT Reverse Micelles. *J. Phys. Chem. B* **2007**, 111, 14193–14207.

(20) Shaw, D. J.; Panman, M. R.; Woutersen, S. Evidence for Cooperative Vibrational Relaxation of the NH-, OH-, and OD-Stretching Modes in Hydrogen-Bonded Liquids Using Infrared Pump-Probe Spectroscopy. *Phys. Rev. Lett.* **2009**, 103, 227401.

(21) Woutersen, S.; Emmerichs, U.; Bakker, H. J. Femtosecond Mid-IR Pump-Probe Spectroscopy of Liquid Water: Evidence for a Two-Component Structure. *Science* **1997**, 278, 658–660.

(22) DeFlores, L. P.; Ganim, Z.; Ackley, S. F.; Chung, H. S.; Tokmakoff, A. The Anharmonic Vibrational Potential and Relaxation Pathways of the Amide I and II Modes of N-Methylacetamide. *J. Phys. Chem. B* **2006**, 110, 18973–18980.

(23) Dijkstra, A. G.; Jansen, T. L. C.; Bloem, R.; Knoester, J. Simulation of Vibrational Energy Transfer in Two-Dimensional Infrared Spectroscopy of Amide I and Amide II Mode in Solution. *J. Chem. Phys.* **2007**, 127, 194505.

(24) Bloem, R.; Dijkstra, A. G.; Jansen, T. L. C.; Knoester, J. Simulation of Vibrational Energy Transfer in Two-Dimensional Infrared Spectroscopy of Amide I and Amide II Mode in Solution. *J. Chem. Phys.* **2008**, 129, 055101.

(25) Barth, A.; Zscherp, C. What Vibrations Tell about Proteins. *Q. Rev. Biophys.* **2002**, 35,369-430.

(26) Wahl, M. C_H…O Hydrogen Bonding in Biology. *Trends Biochem. Sci.* **1997**, 22, 97–102.

(27) Bandekar, J. Amide Modes and Protein Conformation. *Biochim. Biophys. Acta.* **1992**, 1120, 123–143.

(28) Thakkar, A. J. *Quantum Chemistry*; Morgan & Claypool Publishers, San Rafael, CA, 2017.

(29) Jansen, T. L. C.; Cringus, D.; Pshenichnikov, M. S. Dissimilar Dynamics of Coupled Water Vibrations. *J. Phys. Chem. A* **2009**, 113, 6260–6265.

(30) Kwac, K.; Cho, M. Molecular Dynamics Simulation Study of N-Methylacetamide in Water. II. Two-Dimensional Infrared Pump-Probe Spectra. *J. Chem. Phys.* **2003**, 119, 2256–2263.

(31) Cringus, D.; Yeremenko, S.; Pshenichnikov, M. S.; Wiersma, D. A. Hydrogen Bonding and Vibrational Energy Relaxation in Water-Acetonitrile Mixtures. *J. Phys. Chem. B* **2004**, 108, 10376–10387.

(32) Mazur, K.; Bonn, M.; Hunger, J. Hydrogen Bond Dynamics in Primary Alcohols: A Femtosecond Infrared Study. *J. Phys. Chem. B* **2015**, 119, 1558–1566.

(33) Kagan, C.; Murray, C.; Bawendi, M. Long-Range Resonance Transfer of Electronic Excitations in Close-Packed CdSe Quantum-Dot Solids. *Phys. Rev. B* **1996**, 54, 8633–8643.

(34) Reed, A. E.; Curtiss, L. A.; Weinhold, F. Intermolecular Interactions from a Natural Bond Orbital, Donor—Acceptor Viewpoint. *Chem. Rev.* **1988**, 88, 899–926.

(35) Isoda, H.; Furukawa, Y. Infrared Spectroscopic Study on Electric-Field-Induced Dynamics of Polymer Chains in a Ferroelectric Melt-Quenched Cold-Drawn Film of Nylon-12. *Vib. Spectrosc.* **2016**, 84, 30–37.

(36) Arunan, E.; Desiraju, G. R.; Klein, R. A.; Sadlej, J.; Scheiner, S.; Alkorta, I.; Clary, D. C.; Crabtree, R. H.; Dannenberg, J. J.; Hobza, P.; et al. Definition of the Hydrogen Bond. *Pure Appl. Chem.* **2011**, 83, 1637–1641.

(37) Thar, J.; Kirchner, B. Hydrogen Bond Detection. *J. Phys. Chem. A* **2006**, 110, 4229–4237.

(38) Cuff, A. L.; Janes, R. W.; Martin, A. C. Analysing the Ability to Retain Sidechain Hydrogen-Bonds in Mutant Proteins. *Bioinformatics* **2006**, 22, 1464–1470.

(39) Liu, A.; Wang, J.; Lu, Z.; Yao, L.; Li, Y.; Yan, H. Hydrogen-Bond Detection, Configuration Assignment and Rotamer Correction of Side-Chain Amides in Large Proteins by NMR Spectroscopy through Protium/Deuterium Isotope Effects. *Chembiochem* **2008**, 9, 2860–2871.

(40) Torshin, I. Y.; Weber, I. T.; Harrison, R. W. Geometric Criteria of Hydrogen Bonds in Proteins and Identification of `bifurcated' Hydrogen Bonds. *Protein Eng. Des. Sel.* **2002**, 15, 359–363.

(41) Chen, C.; Zhong Li, W.; Chen Song, Y.; Weng, L. D.; Zhang, N. The Effect of Geometrical Criteria on Hydrogen Bonds Analysis in Aqueous Glycerol Solutions. *J. Mol. Imaging Dyn.* **2011**, 1, 1000101.

(42) Li, X.-Z.; Walker, B.; Michaelides, A. Quantum Nature of the Hydrogen Bond. *Proc. Natl. Acad. Sci. U.S.A.* **2011**, 108, 6369–6373.

(43) Del Bene, J. E.; Ajith Perera, S.; Bartlett, R. J. Hydrogen Bond Types, Binding Energies, and 1 H NMR Chemical Shifts. *J. Phys. Chem. A* **1999**, 103, 8121–8124.

(44) Laenen, R.; Gale, G. M.; Lascoux, N. IR Spectroscopy of Hydrogen-Bonded Methanol: Vibrational and Structural Relaxation on the Femtosecond Time Scale. *J. Phys. Chem. A* **1999**, 103, 10708–10712.

(45) Cringus, D.; Lindner, J.; Milder, M. T. W.; Pshenichnikov, M. S.; Vöhringer, P.; Wiersma, D. A Femtosecond Water Dynamics in Reverse-Micellar Nanodroplets. **2005**, 408, 162-168.

(46) Filarowski, A.; Koll, A. Specificity of the Intramolecular Hydrogen Bond. The Differences in Spectroscopic Characteristics of the Intermolecular and Intramolecular H-Bonds. *Vib. Spectrosc.* **1998**, 17, 123–131.

(47) Jeffrey, G. A. *An Introduction to Hydrogen Bonding*; Oxford University Press: New York, 1997.

(48) Kollman, P. A.; Allen, L. C. Theory of the Hydrogen Bond. Chem. Rev. 1972, 72, 283–303.

(49) Mirsky, A. E.; Pauling, L. On The Structure of Native, Denatured, and Coagulated Proteins. *Proc.Nat.Acad.Sci.,* **1936**, 22, 439–447.

(50) Pauling, L.; Corey, R. B.; Branson, H. R. The Structure of Proteins: Two Hydrogen-Bonded Helical Configurations of the Polypeptide Chain. *Proc. Natl. Acad. Sci. U.S.A.* **1951**, 37, 205–211.

(51) Pauling, L.; Corey, R. B. Configurations of Polypeptide Chains With Favored Orientations Around Single Bonds: Two New Pleated Sheets. *Proc. Natl. Acad. Sci. U.S.A.* **1951**, 37, 729–740.

(52) Kendrew, J. C.; Dickerson, R. E.; Strandberg, B. E.; Hart, R. G.; Davies, D. R.; Phillips, D. C.; Shore, V. C. Structure of Myoglobin: A Three-Dimensional Fourier Synthesis at 2 Å. Resolution. *Nature* **1960**, *185*, 422.

(53) Baker, E. N.; Hubbard, R. E. Hydrogen Bonding in Globular Proteins. *Prog. Biophys. Mol. Biol.* **1984**, *44*, 97–179.

(54) Zanni, M. T.; Asplund, M. C.; Hochstrasser, R. M. Two-Dimensional Heterodyned and Stimulated Infrared Photon Echoes of N-Methylacetamide-D. *J. Chem. Phys.* **2001**, 114, 4579–4590.

(55) Chen, X. G.; Schweitzer-Stenner, R.; Krimm, S.; Mirkin, N. G.; Asher, S. A. N-Methylacetamide and Its Hydrogen-Bonded Water Molecules Are Vibrationally Coupled. *J. Am. Chem. Soc.* **1994**, 116, 11141–11142.

(56) Farag, M. H.; Bastida, A.; Ruiz-López, M. F.; Monard, G.; Ingrosso, F. Vibrational Energy Relaxation of the Amide I Mode of N-Methylacetamide in D2O Studied through Born-Oppenheimer Molecular Dynamics. *J. Phys. Chem. B* **2014**, 118, 6186–6197.

(57) Kwac, K.; Cho, M. Molecular Dynamics Simulation Study of N-Methylacetamide in Water. I. Amide I Mode Frequency Fluctuation. *J. Chem. Phys.* **2003**, 119, 2247–2255.

(58) Woutersen, S.; Mu, Y.; Stock, G.; Hamm, P. Hydrogen-Bond Lifetime Measured by Time-Resolved 2D-IR Spectroscopy: N-Methylacetamide in Methanol. *Chem. Phys.* **2001**, 266, 137–147.

(59) Noda, I.; Liu, Y.; Ozaki, Y. Two-Dimensional Correlation Spectroscopy Study of Temperature-Dependent Spectral Variations of N-Methylacetamide in the Pure Liquid State. 2. Two-Dimensional Infrared Analysis. *J. Phys. Chem.* **1996**, 100, 8674–8680.

(60) Roseman, M. A. Hydrophobicity of the Peptide C=O...H-N Hydrogen-Bonded Group. *J. Mol. Biol.* **1988**, 201, 621–623.

(61) DeCamp, M. F.; DeFlores, L.; McCracken, J. M.; Tokmakoff, A.; Kwac, K.; Cho, M. Amide I Vibrational Dynamics of N-Methylacetamide in Polar Solvents: The Role of Electrostatic Interactions. *J. Phys. Chem. B* **2005**, 109, 11016–11026.

(62) Hamm, P.; Lim, M.; Hochstrasser, R. M. Structure of the Amide I Band of Peptides Measured by Femtosecond Nonlinear-Infrared Spectroscopy. *J. Phys. Chem. B* **1998**, 102, 6123–6138.

(63) Ludwig, R. Water: From Clusters to the Bulk. *Angew. Chem. Int. Ed.* **2001**, 40, 1808–1820.

(64) Smith, J. D.; Cappa, C. D.; Wilson, K. R.; Cohen, R. C.; Geissler, P. L.; Saykally, R. J. Unified Description of Temperature-Dependent Hydrogen-Bond Rearrangements in Liquid Water. *Proc. Natl. Acad. Sci. U.S.A.* **2005**, 102, 14171–14174.

(65) Kim, K. H.; Chi, Z.; Cho, M. J.; Jin, J. Il; Cho, M. Y.; Kim, S. J.; Joo, J. S.; Choi, D. H. Soluble Star-Shaped Molecules Based on Thiophene Derivatives as Organic Semiconductors for Field-Effect Transistor Applications. *Chem. Mater.* **2007**, 19, 4925–4932.

(66) Wang, J. L.; Tang, Z. M.; Xiao, Q.; Ma, Y.; Pei, J. Star-Shaped D-π-A Conjugated Molecules: Synthesis and Broad Absorption Bands. *Org. Lett.* **2009**, 11, 863–866.

(67) Lloyd, M. T.; Anthony, J. E.; Malliaras, G. G. Photovoltaics from Soluble Small Molecules. *Materials Today*. 2007, pp 34–41.

(68) Zhang, Q.; Kan, B.; Liu, F.; Long, G.; Wan, X.; Chen, X.; Zuo, Y.; Ni, W.; Zhang, H.; Li, M.; et al. Small-Molecule Solar Cells with Efficiency over 9%. *Nat Phot.* **2015**, 9, 35–41.

(69) Luponosov, Y. N.; Solodukhin, A. N.; Mannanov, A. L.; Trukhanov, V. A.; Peregudova, S. M.; Pisarev, S. A.; Bakirov, A. V; Shcherbina, M. A.; Chvalun, S. N.; Paraschuk, D. Y.; et al. Highly Soluble and Thermally Stable Alkyl-Free Star-Shaped D-π-A Oligomer with Electron-Withdrawing Phenyldicyanovinyl Groups for Organic Photovoltaics. *Org. Electron. physics, Mater. Appl.* **2017**, 51, 180–189.

(70) Min, J.; Luponosov, Y. N.; Ponomarenko, S. A.; Ameri, T.; Li, Y.; Brabec, C. J. Interface Design to Improve the Performance and Stability of Solution-Processed Small Molecule Conventional Solar Cells. *Adv. Energy Mater.* **2014**, 4, 1400816.

(71) Shiau, S. Y.; Chang, C. H.; Chen, W. J.; Wang, H. J.; Jeng, R. J.; Lee, R. H. Star-Shaped Organic Semiconductors with Planar Triazine Core and Diketopyrrolopyrrole Branches for Solution-Processed Small-Molecule Organic Solar Cells. *Dye. Pigment.* **2015**, 115, 35–49.

(72) Salamatova, E.; Kozlov, O. V.; Luponosov, Y. N.; Solodukhin, A. N.; Toropynina, V. Y.; Ponomarenko, S. A.; Pshenichnikov, M. S. Visualization of Molecular Excitons Diffusion. In *Proceedings of SPIE - The International Society for Optical Engineering*; **2016**; 9923, 99230K.

(73) Herschel, W. Experiments on the Refrangibility of the Invisible Rays of the Sun. By William Herschel, LL. D. F. R. S. *Philos. Trans. R. Soc. London* **1800**, 90, 284–292.

(74) Stuart, B. Infrared Spectroscopy. In *Kirk-Othmer Encyclopedia of Chemical Technology*; American Cancer Society, 2015; pp 1–18.

(75) Hamm, P.; Zanni, M. T. *Concepts and Methods of 2D Infrared Spectroscopy*; Cambridge University Press: Cambridge, U.K., 2011.

(76) Cho, M. *Two-Dimensional Optical Spectroscopy*; CRC Press: Boca Raton, FL, 2009.

(77) Cho, M. Coherent Two-Dimensional Optical Spectroscopy. *Chem. Rev.* **2008**, 108, 1331–1418.

(78) Yeremenko, S.; Baltuška, A.; de Haan, F.; Pshenichnikov, M. S.; Wiersma, D. A. Frequency-Resolved Pump-Probe Characterization of Femtosecond Infrared Pulses. *Opt. Lett.* **2002**, 27, 1171–1173.

(79) Yeremenko, S.; Wiersma, D. A. Water Dynamics Explored by Femtosecond Infrared Spectroscopy, University of Groningen, 2004.

(80) Gordon, R. G. Molecular Collisions and the Depolarization of Fluorescence in Gases. *J. Chem. Phys.* **1966**, 45, 1643–1648.

(81) Graener, H.; Seifert, G.; Laubereau, A. Direct Observation of Rotational Relaxation Times by Time-Resolved Infrared Spectroscopy. *Chem. Phys. Lett.* **1990**, 172, 435–439.

(82) Cunha, A. V.; Salamatova, E.; Bloem, R.; Roeters, S. J.; Woutersen, S.; Pshenichnikov, M. S.; Jansen, T. L. C. Interplay between Hydrogen Bonding and Vibrational Coupling in Liquid N-Methylacetamide. *J. Phys. Chem. Lett.* **2017**, 8, 2438-2444.

(83) Kraemer, D.; Cowan, M. L.; Paarmann, A.; Huse, N.; Nibbering, E. T. J.; Elsaesser, T.; Miller, R. J. D. Temperature Dependence of the Two-Dimensional Infrared Spectrum of Liquid H2O. *Proc. Natl. Acad. Sci. U.S.A.* **2008**, 105, 437–442.

(84) Naraharisetty, S. R. G.; Kurochkin, D. V; Rubtsov, I. V. C-D Modes as Structural Reporters via Dual-Frequency 2DIR Spectroscopy. *Chem. Phys. Lett.* **2007**, 437, 262–266.

(85) Kwak, K.; Park, S.; Finkelstein, I. J.; Fayer, M. D. Frequency-Frequency Correlation Functions and Apodization in Two-Dimensional Infrared Vibrational Echo Spectroscopy: A New Approach. *J. Chem. Phys.* **2007**, 127, 124503.

(86) Kwak, K.; Rosenfeld, D. E.; Fayer, M. D. Taking Apart the Two-Dimensional Infrared Vibrational Echo Spectra: More Information and Elimination of Distortions. *J. Chem. Phys.* **2008**, 128, 204505.

(87) Lazonder, K.; Pshenichnikov, M. S.; Wiersma, D. A. Two-Dimensional Optical Correlation Spectroscopy Applied to Liquid / Glass Dynamics. In *Ultrafast Phenomena XV, Proceedings of the 15th International Conference*; Corkum, P., Jonas, D. M., Miller, R. J. D. & Weiner, A. M., Ed.; BERLIN Springer: Berlin, 2006; Vol. 88, pp 356–358.

(88) Lazonder, K.; Pshenichnikov, M. S.; Wiersma, D. A. Easy Interpretation of Optical Two-Dimensional Correlation Spectra. *Opt. Lett.* **2006**, 31, 3354–3356.

(89) Candelaresi, M.; Gumiero, A.; Adamczyk, K.; Robb, K.; Bellota-Antón, C.; Sangal, V.; Munnoch, J.; Greetham, G. M.; Towrie, M.; Hoskisson, P. A.; et al. A Structural and Dynamic Investigation of the Inhibition of Catalase by Nitric Oxide. *Org. Biomol. Chem.* **2013**, 11, 7778–7788.

(90) Eaves, J. D.; Loparo, J. J.; Fecko, C. J.; Roberts, S. T.; Tokmakoff, A.; Geissler, P. L. Hydrogen Bonds in Liquid Water Are Broken Only Fleetingly. *Proc. Natl. Acad. Sci. U.S.A.* **2005**, 102, 13019–13022.

(91) Hamm, P.; Woutersen, S. Coupling of the Amide I Modes of the Glycine Dipeptide. *Bull. Chem. Soc. Jpn.* **2002**, 75, 985–988.

(92) Roberts, S. T.; Loparo, J. J.; Tokmakoff, A. Characterization of Spectral Diffusion from Two-Dimensional Line Shapes. *J. Chem. Phys.* **2006**, 125, 084502.

(93) Finkelstein, I. J.; Ishikawa, H.; Kim, S.; Massari, A. M.; Fayer, M. D. Substrate Binding and Protein Conformational Dynamics Measured by 2D-IR Vibrational Echo Spectroscopy. *Proc. Natl. Acad. Sci. U.S.A.* **2007**, 104, 2637–2642.

(94) Fang, C.; Bauman, J. D.; Das, K.; Remorino, A.; Arnold, E.; Hochstrasser, R. M. Two-Dimensional Infrared Spectra Reveal Relaxation of the Nonnucleoside Inhibitor TMC278 Complexed with HIV-1 Reverse Transcriptase. *Proc. Natl. Acad. Sci. U.S.A.* **2008**, 105, 1472–1477.

(95) Osborne, D. G.; Kubarych, K. J. Rapid and Accurate Measurement of the Frequency–Frequency Correlation Function. *J. Phys. Chem. A* **2013**, 117, 5891–5898.

(96) Bakulin, A. A.; Liang, C.; Jansen, T. L. A. C.; Wiersma, D. A.; Bakker, H. J.; Pshenichnikov, M. S.; Shenichnikov, M. S. P. Hydrophobic Solvation: A 2D IR Spectroscopic Inquest. *Acc. Chem. Res.* **2009**, 42, 1229–1238.

(97) Guo, Q.; Pagano, P.; Li, Y.-L.; Kohen, A.; Cheatum, C. M. Line Shape Analysis of Two-Dimensional Infrared Spectra. *J. Chem. Phys.* **2015**, 142, 212427.

(98) Roy, S.; Pshenichnikov, M. S.; Jansen, T. L. C. Analysis of 2D CS Spectra for Systems with Non-Gaussian Dynamics. *J. Phys. Chem. B* **2011**, 115, 5434–5440.

(99) Lanzani, G. Photophysics Tool Box. In *The Photophysics behind Photovoltaics and Photonics*; Wiley-Blackwell, 2012; pp 89–123.

(100) Lakowicz, J. R. *Principles of Fluorescence Spectroscopy*, Third edit.; Springer Science+Business Media, LLC, 2006.

Chapter 2

Interplay Between Hydrogen Bonding and Vibrational Coupling in Liquid N-methylacetamide

Intrinsically disordered proteins play an important role in biology, and unraveling their labile structure presents a vital challenge. However, the dynamical structure of such proteins thwarts their study by standard techniques such as x-ray diffraction and NMR spectroscopy. Here, we use a neat liquid composed of N-methylacetamide molecules as a model system to elucidate dynamical and structural properties similar to those one can expect to see in intrinsically disordered peptide systems. To examine the structural dynamics in the neat liquid, we combine molecular dynamics, response-function based spectral simulations, and two-dimensional polarization-resolved infrared spectroscopy in the amide I (CO stretch) region. The two-dimensional spectra reveal delicate interplay between hydrogen-bonding and intermolecular vibrational coupling effects, observed through fast anisotropy decay. The present study constitutes a general platform for understanding the structure and dynamics of highly disordered systems.

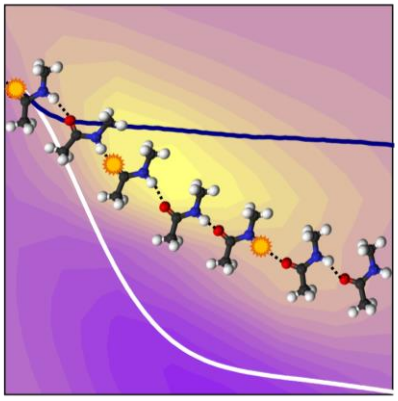

The current chapter is based on the following publication:

Ana V. Cunha, Evgeniia Salamatova, Robbert Bloem, Steven J. Roeters, Sander Woutersen, Maxim S. Pshenichnikov and Thomas L. C. Jansen, *J. Phys. Chem.Lett*. **2017**, 8, 2438-2444.

https://pubs.acs.org/doi/abs/10.1021%2Facs.jpclett.7b00731

2.1 Introduction

Proteins, the engines of living systems, control essentially all the processes that occur in cells. Well-defined structural parts of proteins are responsible for their biological activity. These systems have been extensively studied with molecular dynamics and spectroscopic modeling. However, more recently it has been discovered that intrinsically disordered proteins (IDPs) can also have important biological functions, such as signaling and DNA translation/transcription[1-4].IDPs are characterized by weaker interactions, low quantities of bulky side chains, and sequence simplicity. The intrinsic disorder results in lower structural stability and in an absence of well-defined secondary structure domains. This provides new challenges to molecular dynamics and spectroscopic modeling as the low structural stability allows rapid fluctuations between different conformations, which is crucial for their function. To benchmark the modeling of such systems we utilize a small molecule mimic, N-methylacetamide (NMA)[5-8], as it is composed of a single peptide bond. In the dynamically disordered hydrogen-bonded bulk liquid the NMA molecules interact with each other in a way similar to intrinsically disordered proteins. The molecules have one hydrogen bond accepting oxygen atom and one donating hydrogen atom, as each peptide unit in the protein backbone, which allows fast forming and breaking of hydrogen bonds.

Nuclear magnetic resonance and X-ray crystallography methods are powerful tools to determine structure and dynamics of most biological systems. Nonetheless, the main limitation of these techniques is rooted in the fact that they are not well suited to probe sub-nanosecond dynamics. Two-dimensional infrared spectroscopy (2D-IR) has been used as a novel method to probe transient structure of biological systems[8-13], thus providing dynamical and structural information on femto- to the pico- and nanosecond timescales. The amide I mode, dominated by the CO stretch and NH bending, is the most probed mode in 2D-IR spectroscopy of proteins due to its strong absorbance and high sensitivity to hydrogen bonding and secondary structure[3,14]. Nevertheless, the distribution of different hydrogen bonding environments and vibrational delocalization phenomena arising from intermolecular vibrational coupling result in strongly congested spectra, which are challenging to interpret. Theoretical methods developed recently are of great support to overcome this limitation[15-27]. The combination of classical Molecular Dynamics with response function methods, due to their low computational cost and high accuracy, has become a powerful tool to model 2D-IR spectra[4,16,20,28-30]. Conceptually, a time-dependent Hamiltonian containing the site frequencies and the couplings between the molecular sites derived from MD simulations is generated using electrostatic maps[7,18,21,22,29,31]. This

information is converted to 2D spectra using response-function based calculations[32,33], which in combination with experimental results are used to disentangle different contributions to spectral shapes and dynamics.

In the current Chapter, unlike in many other previous studies[7,8,24,29,34-38], we use bulk NMA as opposed to NMA molecules diluted in different solvents, which provides direct insight into the interactions and dynamics in this liquid. Previously, neat liquids of molecules each containing a peptide unit were also studied with 2D-IR[10,39]. The first molecule, N,N-dimethylformamide[39], has one hydrogen bond accepting oxygen atom but no donating hydrogen atom, and thus does not form hydrogen bonds as a the NMA liquid studied herein. The second molecule, formamide[10], has one hydrogen bond accepting oxygen atom and two donating hydrogen atoms, which results in more branched structures than in peptides.

The goal of this Chapter is to investigate the structure and dynamics of liquid NMA as a first step towards using 2D-IR to study intrinsically disordered proteins/peptides. We use 2D-IR spectroscopy on the NMA amide I mode combining theoretical predictions with experimental data. We unravel the contributions of hydrogen bonding and vibrational delocalization over multiple peptide units to the amide I vibration spectrum. Our findings reveal that even in highly disordered systems one can expect to find highly delocalized amide I vibrations while the hydrogen bond exchange is still relatively slow.

2.2 Results and Discussion

The experimental and theoretical FTIR spectra of neat liquid NMA (Figure 2.1) are quite similar. They both exhibit the main band at 1655 cm^{-1} and sub-bands at ~1695 cm^{-1} or ~1685 cm^{-1}, for theory and experiment, respectively. In the experiment, a low-frequency shoulder is also observed at ~1635 cm^{-1}. This is attributed to the H-O-H bend absorption of residual water (<5% molar) in the sample (see SI for details). This mode was not included in the spectral modeling nor will be considered in the rest of the Chapter.

To disentangle the origin of the two NMA bands, we first performed spectral calculations omitting the intermolecular vibrational couplings given by the electrostatic coupling between the amide I units (details given in the Theoretical Methods section), thus obtaining an FTIR spectrum of uncoupled NMAs (Figure 2.1). By comparison of the coupled and uncoupled theoretical spectra, it is clear that the intermolecular vibrational coupling lead to a ~17 cm^{-1} redshift of the main band which consistent with a similar effect in β-sheets[16,40], and an overall broadening of the spectrum. Both spectra clearly have at least two components contributing.

To unravel the different NMA substructures underlying the spectral features, we characterized the NMA molecules according to their hydrogen bond configuration (Figure 2.2). We employed a criterion similar in spirit to that of the most commonly used hydrogen bonding criteria, which is defined in terms of the distance between atoms in the accepting and donating groups as well as an angle involving two atoms of the hydrogen donor[41]. Namely, the distance between the oxygen atom of the accepting group and the nitrogen of the donating group is used, along with the angle between the carbon (accepting), oxygen (accepting), and nitrogen (donating) atoms (Figure 2.2a). This criterion allows for a better structure-frequency relationship than the more traditional donor-centered hydrogen-bonding criterion[41]. This is because the frequency shift of the amide I depends largely on the electric field exerted by the surrounding molecules on the NMA molecules along the CO bond, for which the oxygen acts as a hydrogen-bond acceptor.

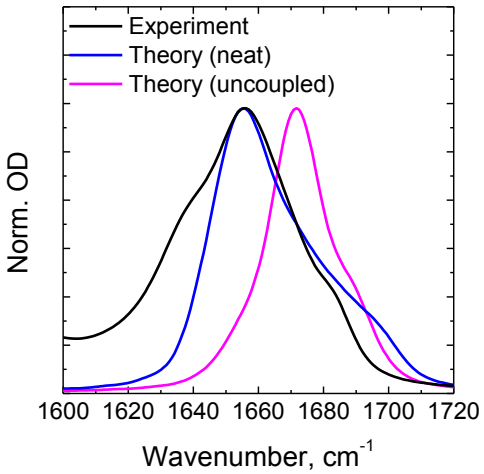

Figure 2.1 Experimental (black line) and theoretical (blue line) FTIR spectra of liquid NMA at 300 K. The magenta line shows the theoretical FTIR spectrum with couplings between amide I units set to zero. The additional shoulder around ~1635 cm^{-1} in the experiment

Four main NMA species have been distinguished. The most abundant species (42%) is a hydrogen-bonded chain (c-NMA) (Figure 2.2d) resembling the cross-strand configurations found in intrinsically disordered peptides[4]. This structure is followed in abundance by the substructures in which NMA is interacting with one other NMA either by the accepting (a-NMA, 20%) or the donating (d-NMA, 20%) group, and a free NMA configuration (f-NMA, 10%) that does not directly hydrogen bond with other molecules (Figure 2.2). The remaining 8% of the configurations involve different types of bifurcated states, where the NMA molecule either accepts or donates two hydrogen bonds; these states do not play any substantial role due to their scarcity.

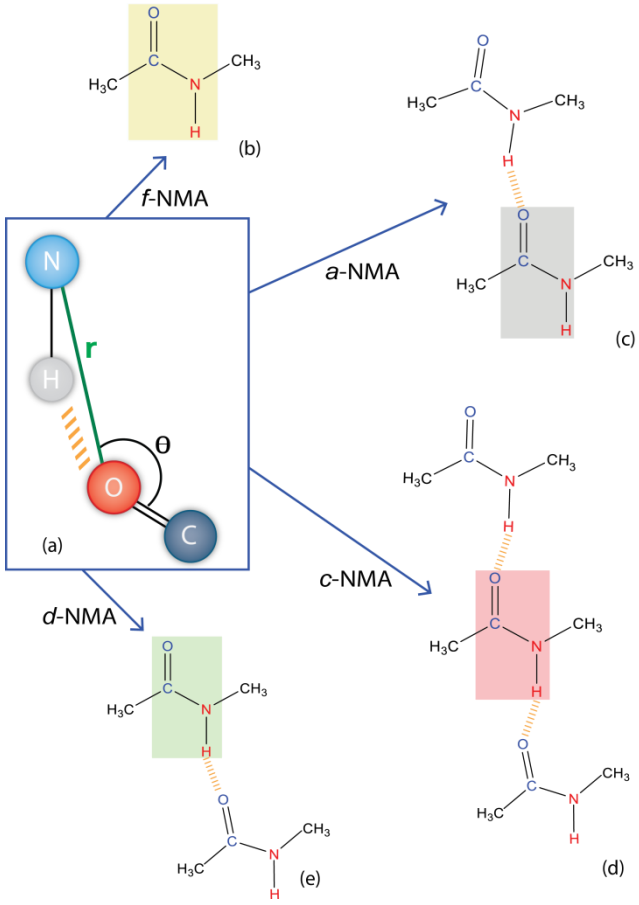

Figure 2.2: Schematic drawings of the different NMA species categorized with a hydrogen bonding configuration criterion (a), where an r_{NO} distance smaller than 3.5 Å and an angle θ larger than 120° are used to ascribe a hydrogen bond. The colored rectangles highlight the categorized NMA molecules, while the other molecules are the hydrogen bond partners. The four main species identified: (b) f-NMA: NMA with no hydrogen bonds, (c) a-NMA: accepting NMA, (d) c-NMA: chain of hydrogen-bonded NMA molecules, (e) d-NMA: donating NMA.

To understand in which species the intermolecular vibrational couplings are most pronounced, we calculated the linear spectra in the static approximation for each of the four species independently for both the uncoupled (Figure 2.3a) and coupled (Figure 2.3b) cases.

For the spectra, where the vibrational couplings are neglected (Figure 2.3a), the c-NMA and the a-NMA species, which both accept a hydrogen bond, absorb in the red flank of the spectrum, while the d-NMA and the f-NMA, which do not accept a hydrogen-bond, absorb in the blue region of the spectrum. For the coupled-case spectra (Figure 2.3b), the peaks of the species accepting hydrogen bonds are

redshifted due to the vibrational coupling for c-NMA and to a lesser extend a-NMA. Noteworthy, there is a shoulder in the c-NMA spectrum at ~1695 cm^{-1} in the coupled case which is not present in the uncoupled case (red dashed line in Figure 2.3). This suggests that this shoulder originates from vibrational couplings among different c-NMA molecules and from f-NMA and a-NMA absorption.

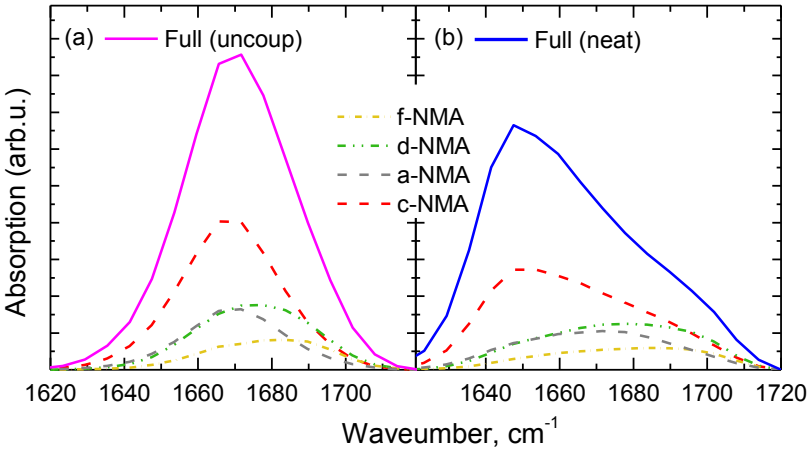

Figure 2.3: Linear spectra calculated in the static approximation for the different hydrogen-bonded species of NMA. In (a), the vibrational couplings are set to zero , in (b) the full vibrational Hamiltonian for the given subset of molecules is included.

2D-IR experimental and theoretical spectra shown in Figure 2.4 are in good agreement, apart from the shoulder on the red side of the experimental spectra arising from the water bend (see also Figure S2.1). In both cases, the diagonally elongated spectra are composed of two peaks with central frequencies of ~1655 cm^{-1}, and ~1685 cm^{-1} or ~1695 cm^{-1}, experiment and theory respectively. Note that the sub-peak at 1695 cm^{-1} identified previously in the linear absorption spectra (Figure 2.1), is much clearer resolved in the 2D-IR spectra because of diagonal elongation.

The anisotropy decay of neat NMA (Figure 2.5a) was extracted from the parallel and perpendicular polarized 2D-IR spectra (Figures S2.7 and S2.8 in SI) at the position of the main peak. Both theoretical and experimental anisotropy transients are considerably faster than the anisotropy of the uncoupled case. The latter matches very well with the rotational correlation function (Figure 2.5b, red symbols) thereby demonstrating the purely orientational origin of the decay on a 20 ps time scale (see Table S2.1 in SI for the fitting parameters). This immediately suggests that the anisotropy is affected by vibrational coupling that results in population migration from one oscillator to another thereby accelerating the anisotropy

decay[27,42-43]. The experimental value starts below 0.4, which is most likely related to the finite pulse duration, which was not included in the theory.

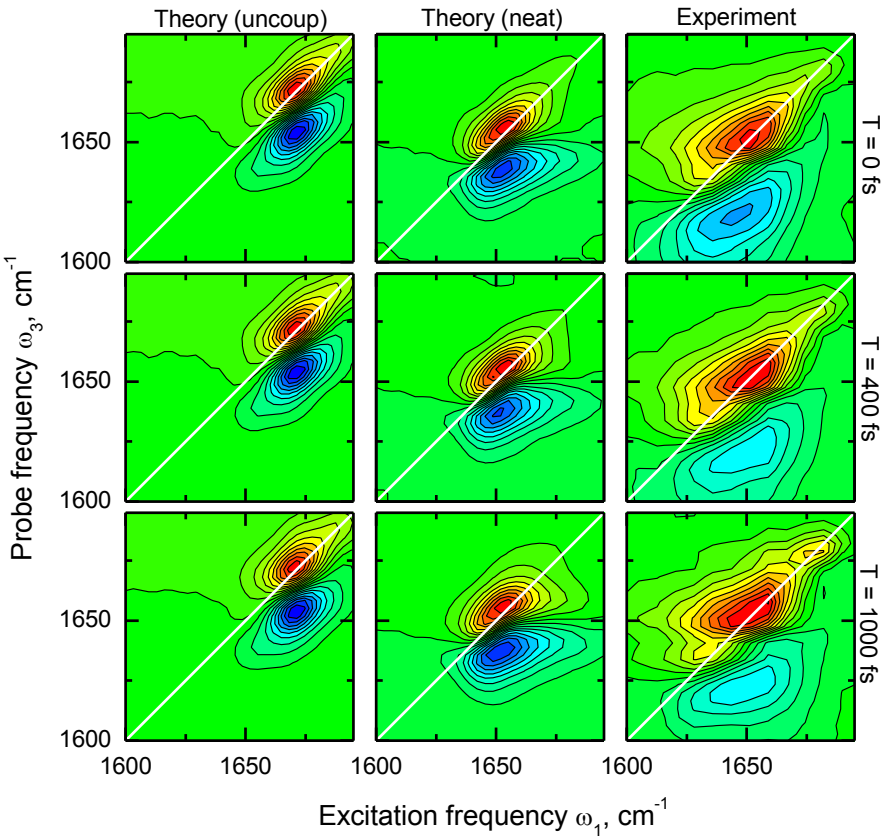

Figure 2.4: 2D-IR parallel polarization spectra of bulk NMA for different waiting times: uncoupled NMA (left panels), theoretical NMA (middle panels), experimental (right panels) spectra at different waiting times t_2. Equidistant contour lines are drawn with 10% steps from the maximum; red colors indicate bleach, while blue colors indicate absorption.

Next, we calculated the population transfer defined as the probability that a molecule excited at time zero will still be excited at time *t* (see Figure 2.5b). The population dynamics consists of a fast part resulting in the Gaussian decay with a timescale of 400 fs, and a slower part resulting in an exponential decay of 1.3 ps. This suggests that the population transfer between hydrogen-bonded molecules is dominated by the fast Gaussian decay, while transfer involving the non-hydrogen bonded species is exponential and occurs on the slower time scale. This demonstrates that the vibrational excitation moves along the hydrogen bonded chains (see Figure 2.2d), which largely preserve the orientation of the transition dipole despite the movement of the vibrational excitation. This alignment was

quantified by calculating the joint angular-radial distribution function for the CO bonds (see SI Figure S2.9). We further found that typical couplings along the chains amount to -7.5 cm^{-1}, while couplings between NMA molecules in different chains in close proximity to each other are typically around -2.5 cm^{-1}. This means that even the coupling is a through space electrostatic effect the coupling along the hydrogen bonds is 3 times larger than between chains, which leads to more efficient delocalization of the vibrational modes along the hydrogen bond chains than between chains. Note that a similar effect was previously discussed for the amide-A vibration of neat NMA[44]; however the population transfer in that case was much slower.

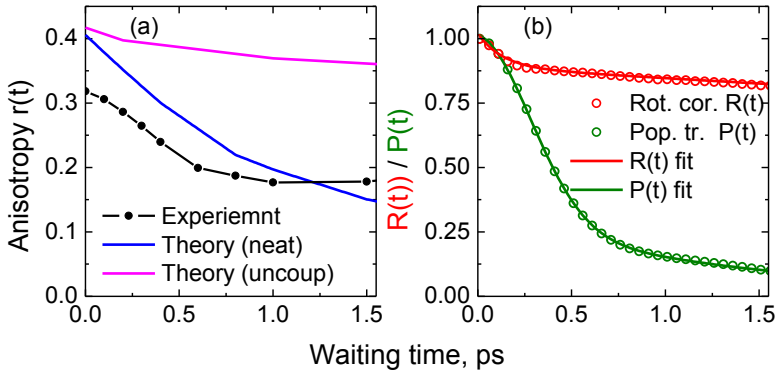

Figure 2.5: (a) Anisotropy decay for the main absorption peak integrated over the frequency ranges (1651 cm^{-1}<ω_1<1661 cm^{-1},1647 cm^{-1}<ω_3<1662 cm^{-1}) for both theory and experimental spectra. For the uncoupled spectra the anisotropy decay was integrated over the main peak frequency range (1668 cm^{-1}<ω_1<1674 cm^{-1}, 1668 cm^{-1}<ω_3<1674 cm^{-1}). (b) The orientational correlation function (red symbols) and population transfer dynamics (olive symbols. The data of panel (b) were fitted to a biexponential function for the orientational correlation function, and to a sum of a Gaussian and an exponential decay for the population transfer. The fits are shown in dashed lines and the parameters are provided in Table S2.1 of the SI.

Our conclusion on the extent of the vibrational delocalization is further corroborated by the inverse participation ratio[45], in the static limit, which is a measure of the delocalization of the vibrational mode in the system. We find that on average the vibration is delocalized over 42 molecules despite the orientational disorder in the liquid. This is larger than values previously reported value for normal proteins, ranging from 4 to 23[8,46], which can be understood by the finite size of the proteins and the fact that these proteins also contain bulky side chains diluting the density of amide I modes. In a previous study on N,N-dimethylacetamide[39] the inverse participation ratio was determined for simulation boxes with different size demonstrating that this quantity depends strongly on the size of the system and that one needs to be cautious with the interpretation of this number for three-

dimensional systems. The fact that the effects of vibrational coupling are stronger in the c-NMA and a-NMA configurations as seen in Figure 2.3 further demonstrates that the hydrogen bonding facilitate the strong vibrational delocalization.

Finally, we comment on discrepancies between experimental and theoretical data. While the qualitative agreement between theory and experiment is reasonable, the calculated anisotropy decay is slightly different from the experimental one, and the high-frequency peak positions are different, too. This indicates that the couplings predicted in our model are somewhat too large. This agrees well with previous findings using the same coupling model[47]. The presence of the water bend in the experiment does not affect the pain amide I peak significantly (see SI for details), however, the overtone peak region below the main peak in the 2D-IR spectra might be contaminated with the water bend response.

2.3 Conclusions

In this Chapter, we have investigated both experimentally and theoretically, the structure and dynamics of bulk NMA using linear and 2D-IR spectroscopy. The main spectroscopic features from both approaches agree very well enabling the interpretation in terms of hydrogen bonding and population transfer from the simulations. We find that NMA aggregation involves four main hydrogen-bonding structures, of which the chain structure is most abundant. The main absorption band is red-shifted due to intermolecular vibrational coupling. The high-frequency shoulder contains both a contribution from a coupling induced sub-band of the c-NMA hydrogen bond species and the main absorption of the d-NMA and f-NMA species. The anisotropy decay of the main band is much faster than the orientational relaxation due to population transfer but is still considerably slower than the population transfer. This demonstrates delicate interplay between coupling effects and angular correlations of the hydrogen-bonded amide I oscillators even in disordered liquid NMA.

2D-IR anisotropic spectroscopy has proven as powerful tools to unravel the interplay between hydrogen bonding vibrational delocalization in liquid NMA. The present study serves as an important benchmark for the models for the structure and dynamics used to unravel spectral signatures of highly disordered systems.

2.4 Materials and Methods

2.4.1 Theoretical methods

Molecular dynamics simulations were performed with the GROMACS suite version 4.6.1 [48] using the OPLS-AA[49] force field to describe 343 N-methylacetamide

molecules. After an initial energy minimization, a constant pressure equilibration of 1 ns at 300 K using Berendsen barostat[50], with an inverse time constant of 0.2 ps^{-1}, was done. This was followed by a constant volume equilibration of 1 ns at 300 K at the equilibrium density. A constant volume production run of 1 ns at 300 K was performed and the coordinates were stored at each 10 fs for analysis and spectral modeling. For all simulations a 1 fs time step was used, and the temperature was kept constant using the Berendsen thermostat[50]. Here a 1.1 nm cutoff was used for both Lennard-Jones and Coulomb interactions. The latter were treated using Particle Mesh Ewald method, with a grid step of 0.16 nm and a convergence of 10^{-5} [51]. The truncation of the Lennard-Jones interactions was compensated by introducing analytical corrections to pressure and potential energy[52]. All bonds were constrained using the LINCS algorithm[53]. The radial distribution functions of the liquid were calculated for all simulations, and are in agreement with those previously obtained[49]. Furthermore, the joint angular-radial distribution function for the CO bonds was calculated to quantify the angular ordering (see SI, Figure S2.9).

The time-dependent vibrational Hamiltonian for the amide I modes was constructed from the snapshots stored from the MD production run. This Hamiltonian has the form[8, 15, 54]

$$H(t) = \sum_{i}^{N} \omega_i(t) B_i^{\dagger} B_i \; + \frac{\Delta}{2} \sum_{i}^{N} B_i^{\dagger} B_i^{\dagger} B_i \; B_i \; + \sum_{i \neq j}^{N} J_{ij}(t) B_i^{\dagger} B_j \; - \sum_{i}^{N} \vec{\mu}_i(t) \vec{E}(t) \left(B_i^{\dagger} + B_i \right)$$

(Eq. 2.1)

Here $B_i^{\dagger}$ and B_i are the bosonic creation and annihilation operators, $\omega_i(t)$ is the time dependent fundamental amide I frequency for the *i*'th molecule, and $\vec{\mu}_i(t)$ is the corresponding transition dipole. The anharmonicity, Δ_i, was kept constant at 16 cm^{-1} [8]. The site frequencies of the amide I, $\omega_i(t)$, were calculated using the Jansen electrostatic map[29], which relates the electrostatic field and gradient generated by the point charges of the MD force field with the frequency, and the transition dipoles. The long range intermolecular couplings between the different amide I units were calculated using the transition charge coupling (TCC) model[28], where a charge, q_n, and a transition charge, dq_n, and a normal mode coordinate, $\vec{v}_{n_i}$, are assigned to each atom of the amide one I unit. The TCC model has the form:

$$J_{ij} = \frac{1}{4\pi\varepsilon_0}\sum_{n,m}\left(\frac{dq_n dq_m}{\left|\vec{r}_{n_i m_j}\right|} - \frac{3q_n q_m\left(\vec{v}_{n_i}\cdot\vec{r}_{n_i m_j}\right)\left(\vec{v}_{m_j}\cdot\vec{r}_{n_i m_j}\right)}{\left|\vec{r}_{n_i m_j}\right|^5} - \frac{dq_n q_m \vec{v}_{m_j}\cdot\vec{r}_{n_i m_j} + q_n dq_m \vec{v}_{n_i}\cdot\vec{r}_{n_i m_j} - q_n q_m \vec{v}_{n_i}\cdot\vec{v}_{m_j}}{\left|\vec{r}_{n_i m_j}\right|^3}\right)$$

(Eq. 2.2)

Here, the subscripts n, and m, number the atoms, which belong to different amide I modes at molecules i, and j, respectively. The distance vector between two atoms in the involved molecules is given by $\vec{r}_{n_i m_j}$. This vibrational Hamiltonian mapping was demonstrated to work well in combination with the OPLS-AA force field in a recent benchmark study for proteins[26].

The spectra were calculated using the Numerical Integration of Schrödinger Equation (NISE) method[20,55]. Here, the time dependent Schrödinger equation is solved numerically for the time-dependent amide I Hamiltonian. The first- and third-order response functions were calculated and the linear absorption and 2D-IR spectra were obtained from Fourier transforms of these response functions. We used coherence times from 0 to 1.25 ps, and a lifetime of 1.8 ps for apodization. The response functions were calculated from starting configurations spaced by 2 ps along the trajectory, giving an ensemble average over 500 realizations. For analysis purposes linear spectra were also calculated in the static approximation, where the effect of motional narrowing is neglected.

2.4.2 Experimental

N-methylacetamide (NMA) with purity of ≥99% was obtained from Sigma-Aldrich and used without any further purification. NMA is a solid under the room temperature of ~22°C (the melting point is 28°C[56]), so it was placed on a heat plate at temperature of 40°C until it was melted completely. After that, an NMA droplet of ~1.4 µl was squeezed between two 1 mm thick CaF_2 windows which were preheated to T=40°C. The NMA sample thickness was ~2.5 µm assuming that the NMA droplet was spread uniformly between the 1" diameter CaF_2 windows. The sample preparation was performed under nitrogen atmosphere to avoid any contact with air moisture; after the preparation the sample was placed in a nitrogen-filled sample holder. During the experiments, the temperature of the sample was controlled by a thermocouple and maintained at 30.5±1°C by a

thermostat. The water content in the experimental samples does not exceed 5% molar (see SI).

The IR absorption spectra were recorded at an FTIR-spectrometer *Vertex-70* purged with dry nitrogen, with 4 cm^{-1} spectral resolution. The maximal optical density of the sample was measured as OD~0.6 at the central frequency of the amide I mode (1656cm^{-1}).

A collinear 2D-IR setup, based on the interferometer platform described in Ref.57, was used. In short, a 25 μJ, 135 fs IR pulses (140 cm^{-1} FWHM spectral width), centered at 1640 cm^{-1} were split into pump (90% of the total intensity), probe and reference beams. The reference pulse was advanced in respect to the pump beam by 40 ps. A wobbler in the pump beam path generated a *-π, 0, +π, 0* phase sequence[58] for each subsequent pulse at 1 kHz repetition rate to remove sample scattering. Before the sample cell, the polarization of the pump beam was rotated by 45° by a halfwave plate. After the sample cell, a movable polarizer selected either the parallel or perpendicular polarization of the probe/reference beams. The probe light was dispersed by a polychromator (Newport Oriel MS 260i) onto one array of 2x32 pixel MCT array (Infrared Associates) to create the ω_3 dimension. The second array was used for detection of the reference spectrum over which the probe spectrum was normalized at each laser shot. With two polychromator settings, a combined spectral window of 150 cm^{-1} was achieved. The delay between the two pump pulses, t_1, was scanned up to 2 ps using fast scanning approach[57]. The waiting time between the later pump pulse and the probe, *T*, was set at different values to study the system dynamics. The 2D signal was averaged over the wobbler-generated phase sequence to extract the nonlinear response related to all three pulses (two pumps and the probe), zero-padded to 4 ps, and Fourier-transformed to obtain the ω_1 dimension with the phase correction applied[59].

For the pump-probe measurements, one of the pump pulses was blocked and a chopper was installed in the other pump beam. The amide-I mode lifetime was obtained as 450±100 fs while the thermalization time of the hot ground state was measured as 5±1 ps (see SI for details). These two values provide experimental window of ~2 ps for 2D-IR spectroscopy.

The whole interferometer was constantly purged with dry air. The whole measuring cycle lasted for ~16 hours.

2.5 Supporting Information

2.5.1 Water content in the NMA sample

NMA is strongly hygroscopic and easily contaminated with water. The water bending mode frequency (~1635 cm^{-1}) lies in the spectral region of interest (1600-1700 cm^{-1}). To determine the actual water content in the sample, the OH-stretching mode of diluted water molecules at 3500 cm^{-1} was used. FTIR spectra of two NMA samples with well-controlled water content (5 and 10% molar added) were measured and normalized to the OD of the NH-stretching mode of NMA at 3300 cm^{-1} (Figure S2.1). The linear fit to the data points constitutes the calibration curve from which we determined the water content in the experimental samples as 2.5 and 5% molar before and after the experimental session.

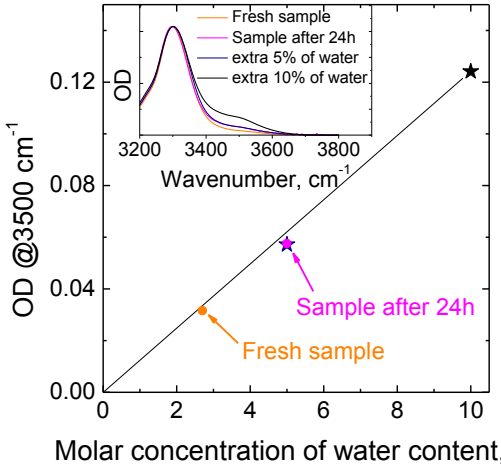

Figure S2.1 Calibration curve: dependence of OD of the OH-stretching mode on water content. The stars show the data points for the molar water content of 5% and 10% added while the dots depict OD of the sample before and after the experimental session. The inset shows the NH/OH stretching region of the sample; all spectra are normalized to OD of NMA NH-stretching mode at 3300 cm^{-1}.

2.5.2 Linear FTIR spectra at different water concentrations

The FTIR spectra of NMA in the amide I region with different water content are shown in Figure S2.2. The amplitude of the peak at ~1635 cm^{-1} increases with increased water content so that it was identified as the bending mode[55-56] of residual water in the NMA sample (blue line in Figure S2.1). In this Chapter, we do not elaborate further on the water bending peak but remark that water presence might lead to slight broadening of the main amide I peak (Figure 2.1). Also note that the increased water content decreases the peak at ~1685 cm^{-1} that is assigned to a combined action of hydrogen-bonding and vibrational coupling. This suggests

that the water molecules mediate NMA hydrogen bonding, in particular, in the chain structures (Figure 2.2d).

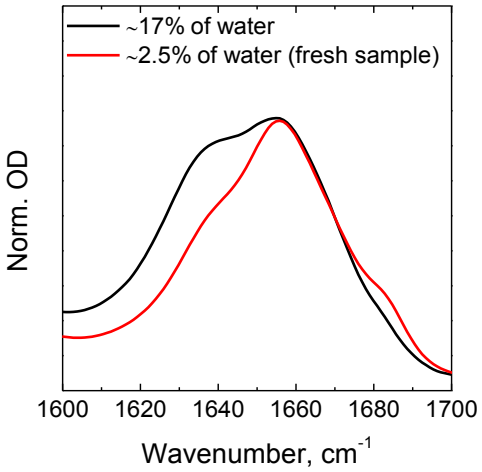

Figure S2.2: FTIR spectra of NMA samples with different water contents.

2.5.3 Temperature jump

Isotropic transient pump-probe spectra calculated as $I(\omega) = I_{\parallel}(\omega) + 2 \cdot I_{\perp}(\omega)$ (with $I_{\parallel}(\omega)$ and $I_{\perp}(\omega)$ being the parallel and orthogonally polarized spectra, respectively) are shown in Figure S2.3. At the early times, the spectrum is dominated by the bleaching and stimulated emission at the frequency of the |0>-|1> transition (at ~1655 cm^{-1}), and induced absorption at the frequency of |1>-|2> transition (at ~1625 cm^{-1}). At later times (>1 ps), the spectral shape begins to deviate from that at the early times. We assign this effect to thermalization of the ground state, i.e. to the local temperature jump due to excited state relaxation .To prove this point, we calculated the difference absorption spectrum at two temperatures (Figure. S2.4a). As is evident from Figure S2.4b, the pump-probe transient spectrum at a delay of 10 ps possesses a reasonable match with the difference between two absorption spectra of the sample measured with a temperature difference of ~3°C. Calculations based on direct conversion of the pump energy absorbed (~2.5 μJ) into heat in the focal volume of ~10^{-7} cm^3, resulted in a temperature raise of ~5°C which reasonably matches the pump-probe based value.

2.5.4 Excited state lifetime

To calculate the build-up time of the thermalization process, we analyzed the transient near the compensation point at 1644 cm^{-1} (Figure S2.5, blue triangles). Fitting the transient with an exponential function yielded the rise time of 5±1 ps. Clearly, this time is very different from a much faster decay of the excited state

(black and red curves). This makes us conclude that the excited state depopulation proceeds via an intermediate state, identified earlier as the NMA amide II mode[41]. Therefore, we fit the transients at 1655 cm^{-1} (maximal bleach) and 1624 cm^{-1} (maximal induced absorption) with a three-level relaxation model[41] (Figure S4.7) where the intermediate state lifetime was fixed at 5 ps. From this fitting, the excited state lifetime was inferred as 450±100 fs. This, together with the thermalization time of 5±1 ps[29] provides an experimental window for 2D IR spectroscopy as of ~2 ps. After this time, the 2D spectra will acquire a non-negligible contribution from the thermalization effects, which are not included in the theoretical model.

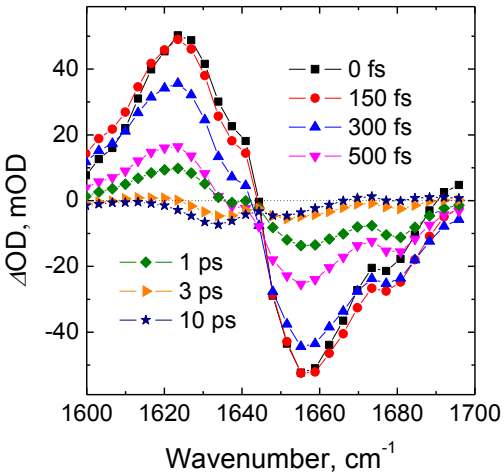

Figure S2.3 Isotropic pump-probe transient spectra at different delay times (shown in legend).

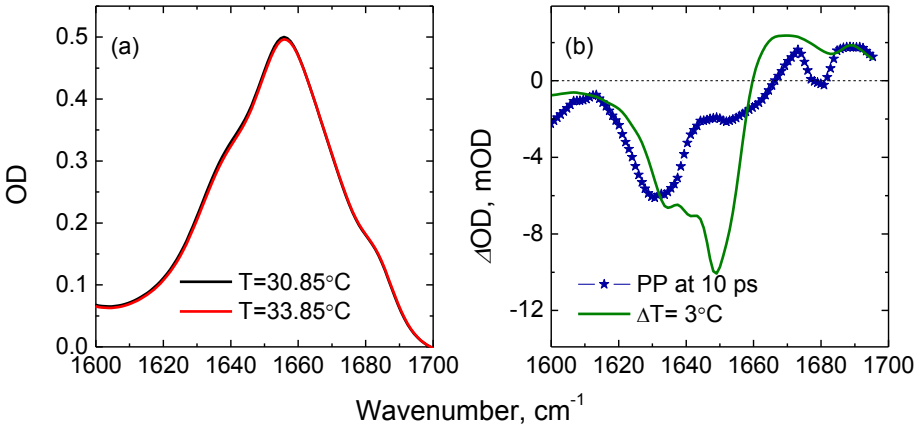

Figure S2.4 (a) FTIR absorption spectra of NMA at two representative temperatures. (b) Comparison of the isotropic transient absorption spectrum at 10 ps delay with the difference absorption spectrum.

2.5.5 Two-dimensional infrared spectra

Figures S2.6 and S2.7 show the comparison of the theoretical and experimental 2D-IR spectra in the amide I region of bulk NMA at different waiting times for parallel and perpendicular polarization, respectively. The spectra were obtained as described in the section 2.4.2. A subtle presence of a ridge, due to the couplings, is identified in the theoretical 2D-IR, at a pump/probe frequency of (ω_1=1655 cm^{-1}, ω_3=1695 cm^{-1}) already at T=0 fs. These are not visible in the experimental 2D-IR at T=0 fs, but as the waiting time is increased the 2D-IR spectra acquires a more square shape, due to the growth of intensity at these off-diagonal positions.

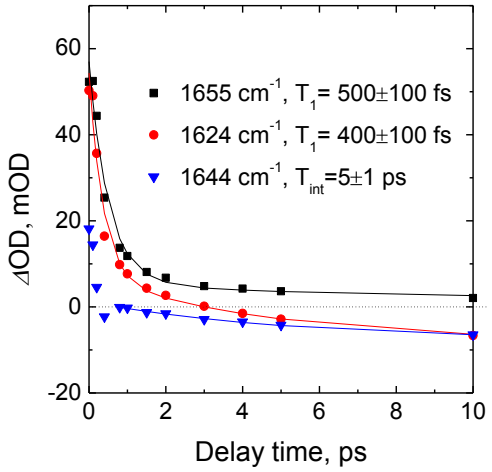

Figure S2.5 Experimental transients (symbols) at a few representative wavelengths (shown in the legend), and the fits according to a three-level relaxation model (solid lines).

2.5.6 Anisotropy decay

To evaluate a possible influence of water to the amide I anisotropy, the anisotropy decay was calculated at the three following frequencies: at the amide I peak, at red and blue flanks of the amide I peak (Figure S2.8). The anisotropy at the red flank (i.e. closer to the water bend mode frequency) decays slower in comparison to the anisotropy at the blue flank; a similar trend is supported by the theoretical data. Therefore, the water bend does not contribute substantially into anisotropy decay. The faster dynamics at the blue side, which is also evident in the theory, can be understood as follows. The anti-symmetric nature of the vibrational states at the high-energy peak (around 1680 cm^{-1} in theory and 1690 cm^{-1} in experiment; see Figure 2.2) results in transition dipoles not aligned with the hydrogen bond chain direction, which leads to a reduced suppression of the anisotropy decay due to diffusion of vibrational excitation. Furthermore, the non-hydrogen-bonded f-NMA and d-NMA species may be rotating slightly faster than the other configurations.

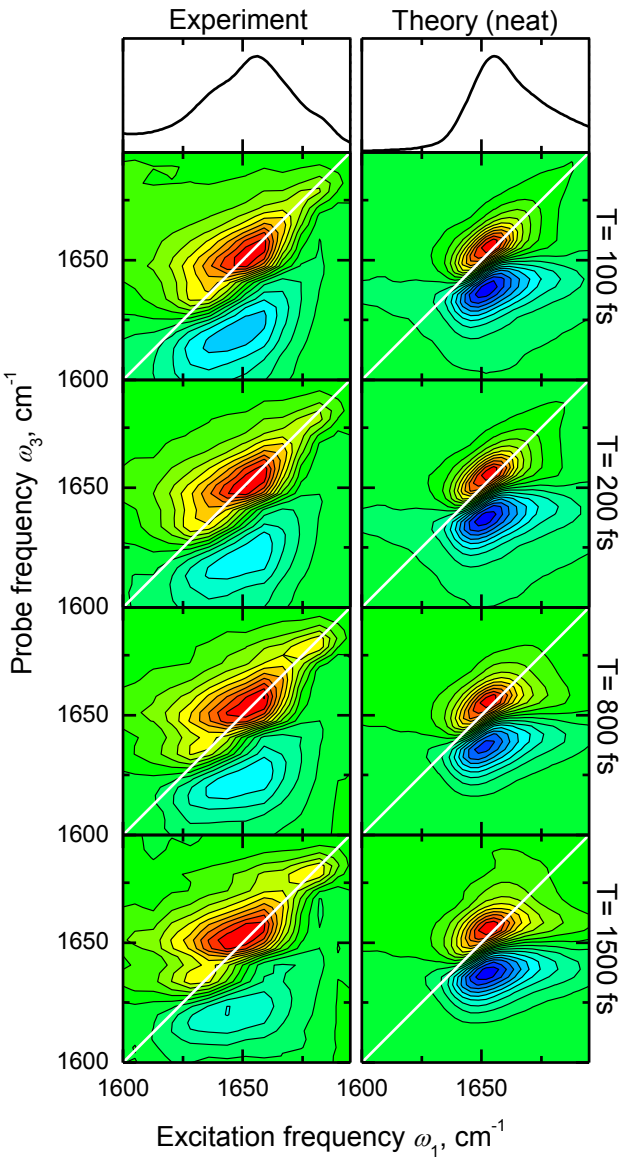

Figure S2.6 Two-dimensional infrared spectra of bulk N-methylacetamide at 300 K for parallel polarization. Equidistant contour lines are drawn with 10% steps from the maximum; red colors indicate bleach, while blue colors indicate absorption.

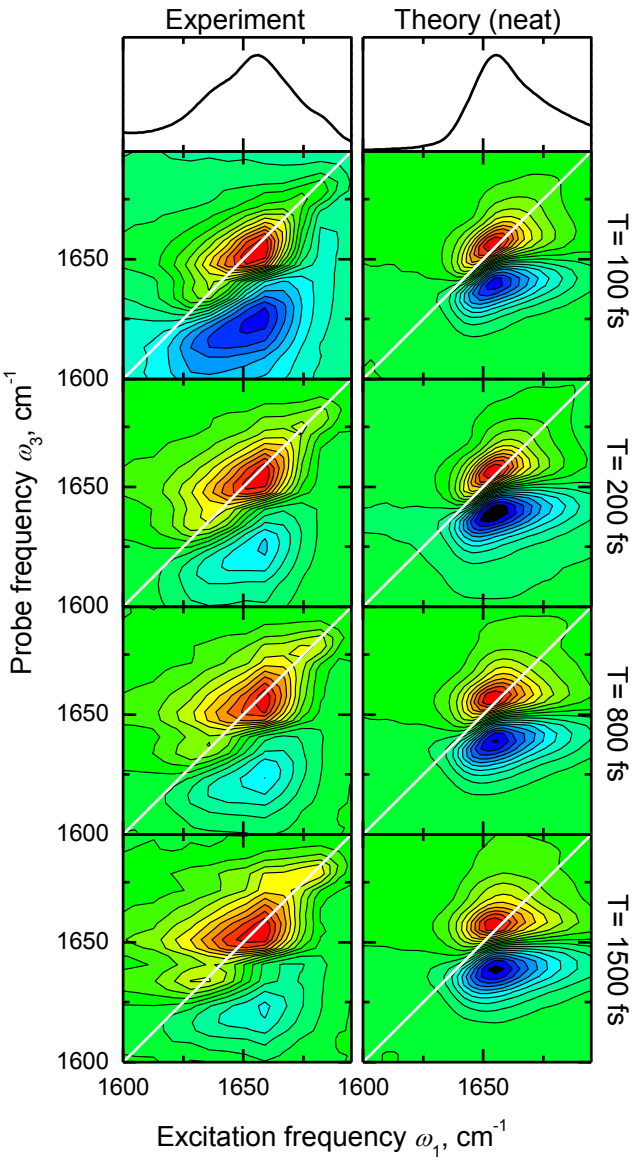

Figure S2.7 Two-dimensional infrared spectra of bulk N-methylacetamide at 300 K for orthogonal polarization. Equidistant contour lines are drawn with 10% steps from the maximum; red colors indicate bleach, while blue colors indicate absorption.

2.5.7 Analysis of the dynamics

Table S2.1 contains the fit parameters of the fits (Eqs. S2.1 and S2.2) of the orientational correlation function, *R(t)*, and the population transfer, *P(t)*. The biexponential, and the gaussian plus exponential fit parameters are defined as:

$$R(t) = A_1 e^{-t/T_1} + A_2 e^{-t/T_2} \qquad \text{(Eq. S2.1)}$$

$$P(t) = A_1 e^{-t/T_1} + A_2 e^{-t^2/T_2^2} \qquad \text{(Eq. S2.2)}$$

Fitting Coefficients	A_1	T_1 (ps)	A_2	T_2 (ps)
Orientational Correlation function *R(t)*	0.89	20	0.13	0.13
Population transfer *P(t)*	0.32	1.30	0.68	0.41

Table S2.1: Fitting parameters for the orientational correlation function, and scaled population transfer.

The Figure S2.9 presents the joint angular-radial distribution function between the CO bonds on the NMA molecules. The peak centered at *cos(Θ)*=1, *r*=0.5 nm represent the aligned NMA molecules in the hydrogen bonded chains. The largest deviations in the angle from the straight chain (0°) are about 60°. An isotropic distribution in the given representation would be a *sin(Θ)* function giving no probability for *cos(Θ)*=1 and *cos(Θ)*=-1 and largest probability at *cos(Θ)*=0.

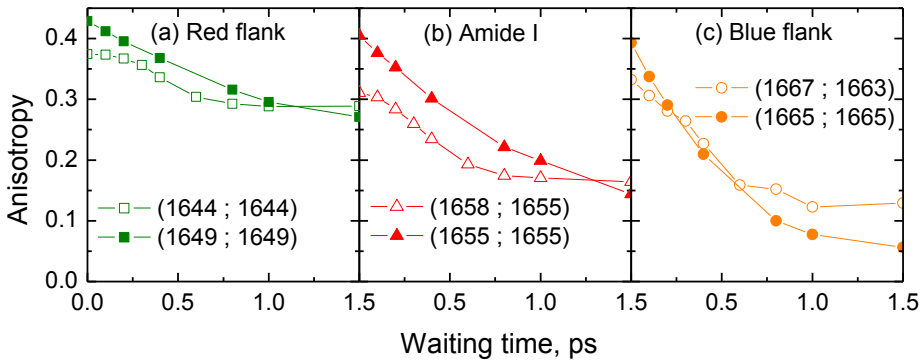

Figure S2.8 Anisotropy decays of the (a) red flank (b) center and (c) blue flank of the amide I mode, calculated from the experimental (open symbols) and theoretical coupled (filled symbols) 2D-IR spectra. The (ω_1,ω_3) frequencies at which the anisotropy was calculated, are shown in the legends.

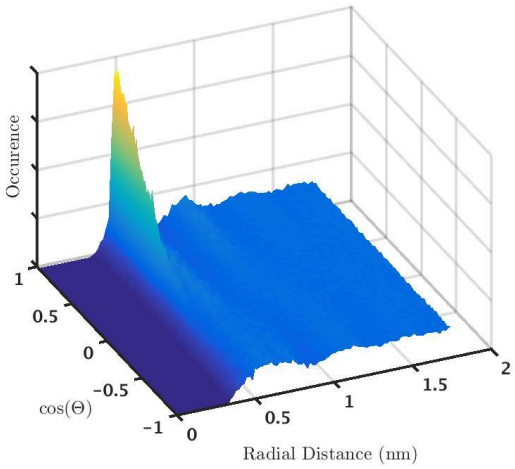

Figure S2.9: The joint angular-radial distribution function for the CO configurations. *Θ* stands for the angle between pairs of CO bonds, with *cos(Θ)*=1 and *cos(Θ)*=-1 representing parallel and anti-parallel bonds, respectively. The distance between the middle of the CO bond pairs, *r*, has a value of 0.5 nm for hydrogen bonded pairs.

Author Contributions

ES, RB, SJR performed 2D-IR experiments under the supervision of SW. AC and TLCJ performed all theoretical calculations; TLCJ and MSP supervised the research. The manuscript was written by AC and ES under the supervision of MSP and TLCJ.

2.6 References

(1) Drescher, M.; Huber, M.; Subramaniam, V., Hunting the Chameleon: Structural Conformations of the Intrinsically Disordered Protein α-Synuclein. *ChemBioChem* **2012**, 13, 761-768.

(2) Uversky, V. N., A Protein-Chameleon: Conformational Plasticity of A-Synuclein, a Disordered Protein Involved in Neurodegenerative Disorders. *J. Biomol. Struct. Dyn*. **2003**, 21, 211-234.

(3) Wells, M.; Tidow, H.; Rutherford, T. J.; Markwick, P.; Ringkjobing Jensen, M.; Mylonas, E.; Svergun, D. I.; Blackledge, M.; Fersht, A. R., Structure of Tumor Suppressor P53 and Its Intrinsically Disordered N-Terminal Transactivation Domain. *Proc. Nat. Acad. Sci.* U.S.A **2008**, 105, 5762-5767.

(4) Lessing, J.; Roy, S.; Reppert, M.; Baer, M.; Marx, D.; Jansen, T. L. C.; Knoester, J.; Tokmakoff, A., Identifying Residual Structure in Intrinsically Disordered Systems: A 2D IR Spectroscopic Study of the Gvgxpgvg Peptide. *J. Am. Chem. Soc.* **2012**, 134, 5032-5035.

(5) Ham, S.; Cho, M., Amide I Modes in the N-Methylacetamide Dimer and Glycine Dipeptide Analog: Diagonal Force Constants. *J. Chem. Phys.* **2003**, 118, 6915-6922.

(6) Kwac, K.; Cho, M., Molecular Dynamics Simulation Study of N-Methylacetamide in Water. I. Amide I Mode Frequency Fluctuation. *J. Chem. Phys.* **2003**, 119, 2247-2255.

(7) DeCamp, M. F.; DeFlores, L.; McCracken, J. M.; Tokmakoff, A.; Kwac, K.; Cho, M., Amide I Vibrational Dynamics of N-Methylacetamide in Polar Solvents: The Role of Electrostatic Interactions. *J. Phys. Chem. B* **2005**, 109, 11016-11026.

(8) Hamm, P.; Lim, M.; Hochstrasser, R. M., Structure of the Amide I Band of Peptides Measured by Femtosecond Nonlinear-Infrared Spectroscopy. *J. Phys. Chem. B* **1998**, 102, 6123-6138.

(9) Buchanan, E. G.; James, W. H.; Choi, S. H.; Guo, L.; Gellman, S. H.; Müller, C. W.; Zwier, T. S., Single-Conformation Infrared Spectra of Model Peptides in the Amide I and Amide II Regions: Experiment-Based Determination of Local Mode Frequencies and Inter-Mode Coupling. *J. Chem. Phys.* **2012**, 137, 094301.

(10) Lima, M.; Chelli, R.; Volkov, V. V.; Righini, R., Two-Dimensional Infrared Spectroscopy of a Structured Liquid: Neat Formamide. *J. Chem. Phys.* **2009**, 130, 204518.

(11) Krimm, S.; Abe, Y., Intermolecular Interaction Effects in the Amide I Vibrations of β-Polypeptides. *Proc. Nat. Acad. Sci. U.S.A* **1972**, 69, 2788-2792.

(12) Roy, S.; Jansen, T. L. C.; Knoester, J., Structural Classification of the Amide I Sites of a β-Hairpin with Isotope Label 2D IR Spectroscopy. *Phys. Chem. Chem. Phys.* **2010**, 12, 9347-9357.

(13) Liang, C.; Louhivuori, M.; Marrink, S. J.; Jansen, T. L. C.; Knoester, J., Vibrational Spectra of a Mechanosensitive Channel. *J. Phys. Chem. Lett.* **2013**, 4, 448-452.

(14) Woutersen, S.; Hamm, P., Time-Resolved Two-Dimensional Vibrational Spectroscopy of a Short α-Helix in Water. *J. Chem. Phys.* **2001**, 115, 7737-7743.

(15) Jansen, T. L. C.; Knoester, J., Waiting Time Dynamics in Two-Dimensional Infrared Spectroscopy. *Acc. Chem. Res.* **2009**, 42, 1405-1411.

(16) Jansen, T. L. C.; Knoester, J., Two-Dimensional Infrared Population Transfer Spectroscopy for Enhancing Structural Markers of Proteins. *Biophys. J.* **2008**, 94, 1818-1825.

(17) Jeon, J.; Cho, M., Direct Quantum Mechanical/Molecular Mechanical Simulations of Two-Dimensional Vibrational Responses: N-Methylacetamide in Water. *New. J. Phys.* **2010**, 12, 065001.

(18) Małolepsza, E.; Straub, J. E., Empirical Maps for the Calculation of Amide I Vibrational Spectra of Proteins from Classical Molecular Dynamics Simulations. *J. Phys. Chem. B.* **2014**, 118, 7848-7855.

(19) Lin, Y. S.; Shorb, J. M.; Mukherjee, P.; Zanni, M. T.; Skinner, J. L., Empirical Amide I Vibrational Frequency Map: Application to 2D IR Line Shapes for Isotope-Edited Membrane Peptide Bundles. *J. Phys. Chem. B* **2009**, 113, 592-602.

(20) Liang, C.; Jansen, T. L. C., An Efficient N3-Scaling Propagation Scheme for Simulating Two-Dimensional Infrared and Visible Spectra. *J. Chem. Theory Comput.* **2012**, 8, 1706-1713.

(21) Bouř, P.; Keiderling, T. A., Empirical Modeling of the Peptide Amide I Band IR Intensity in Water Solution. *J. Chem. Phys.* **2003**, 119, 11253-11262.

(22) Reppert, M.; Tokmakoff, A., Electrostatic Frequency Shifts in Amide I Vibrational Spectra: Direct Parameterization against Experiment. *J. Chem. Phys.* **2013**, 138, 134116.

(23) Reppert, M.; Roy, A. R.; Tokmakoff, A., Isotope-Enriched Protein Standards for Computational Amide I Spectroscopy. *J. Chem. Phys.* **2015**, 142, 125104.

(24) Hayashi, T.; Zhuang, W.; Mukamel, S., Electrostatic DFT Map for the Complete Vibrational Amide Band of NMA. *J. Phys. Chem. A* **2005**, 109, 9747-9759.

(25) Maekawa, H.; Toniolo, C.; Moretto, A.; Broxterman, Q. B.; Ge, N.-H., Different Spectral Signatures of Octapeptide 3_{10}- and α-Helices Revealed by Two-Dimensional Infrared Spectroscopy. *J. Phys. Chem. B* **2006**, 110, 5834-5837.

(26) Cunha, A. V.; Bondarenko, A. S.; Jansen, T. L. C., Assessing Spectral Simulation Protocols for the Amide I Band of Proteins. *J. Chem. Theory Comput.* **2016**, 12, 3982-3992.

(27) Cowan, M. L.; Bruner, B. D.; Huse, N.; Dwyer, J. R.; Chugh, B.; Nibbering, E. T. J.; Elsaesser, T.; Miller, R. J. D., Ultrafast Memory Loss and Energy Redistribution in the Hydrogen Bond Network of Liquid H2O. *Nature* **2005**, 434, 199-202.

(28) Jansen, T. L. C.; Dijkstra, A. G.; Watson, T. M.; Hirst, J. D.; Knoester, J., Modeling the Amide I Bands of Small Peptides. *J. Chem. Phys.* **2006**, 125, 044312.

(29) Jansen, T. L. C.; Knoester, J., A Transferable Electrostatic Map for Solvation Effects on Amide I Vibrations and Its Application to Linear and Two-Dimensional Spectroscopy. *J. Chem. Phys.* **2006**, 124, 044502.

(30) Shinokita, K.; Cunha, A. V.; Jansen, T. L. C.; Pshenichnikov, M. S., Hydrogen Bond Dynamics in Bulk Alcohols. *J. Chem. Phys.* **2015**, 142, 212450.

(31) Reppert, M.; Tokmakoff, A., Communication: Quantitative Multi-Site Frequency Maps for Amide I Vibrational Spectroscopy. *J. Chem. Phys.* **2015**, 143, 061102.

(32) Mukamel, S., *Principles of Nonlinear Optical Spectroscopy;* Oxford University Press: Oxford, 1995.

(33) Hamm, P.; Zanni, M. T. *Concepts and Methods of 2D Infrared Spectroscopy*; Cambridge University Press: Cambridge, U.K., 2011.

(34) Woutersen, S.; Mu, Y.; Stock, G.; Hamm, P., Hydrogen-Bond Lifetime Measured by Time-Resolved 2D IR Spectroscopy: N-Methylacetamide in Methanol. *Chem. Phys.* **2001**, 266, 137-147.

(35) Jansen, T. L. C., Linear Absorption and Two-Dimensional Infrared Spectra of N-Methylacetamide in Chloroform Revisited: Polarizability and Multipole Effects. *J. Phys. Chem. B.* **2014**, 118, 8162-8169.

(36) Wang, L.; Middleton, C. T.; Zanni, M. T.; Skinner, J. L., Development and Validation of Transferable Amide I Vibrational Frequency Maps for Peptides. *J. Phys. Chem. B* **2011**, 115, 3713-3724.

(37) Torii, H., Amide I Vibrational Properties Affected by Hydrogen Bonding out-of-Plane of the Peptide Group. *J. Phys. Chem. Lett.* **2015**, 6, 727-733.

(38) Torri, H., Vibrational Interactions in the Amide I Subspace of the Oligomers and Hydration Clusters of N-Methylacetamide. *J. Phys. Chem. A* **2004**, 108, 7272-7280.

(39) Torri, H., Effects of Intermolecular Vibrational Coupling and Liquid Dynamics on the Polarized Raman and Two-Dimensional Infrared Spectral Profiles of Liquid N,N-

Dimethylformamide Analyzed with a Time-Domain Computational Method. *J. Phys. Chem. A* **2006**, 110, 4822-4832.

(40) Dijkstra, A. G.; Knoester, J., Collective Oscillations and the Linear and Two-Dimensional Infrared Spectra of Inhomogeneous β-Sheets. *J. Phys. Chem. B* **2005**, 109, 9787-9798.

(41) Luzar, A.; Chandler, D., Hydrogen-Bond Kinetics in Liquid Water. *Nature* **1996**, 379, 55-57.

(42) Woutersen, S.; Bakker, H. J., Resonant Intermolecular Transfer of Vibrational Energy in Liquid Water. *Nature* **1999**, 402, 507-509.

(43) Jansen, T. L. C.; Auer, B. M.; Yang, M.; Skinner, J. L., Two-Dimensional Infrared Spectroscopy and Ultrafast Anisotropy Decay of Water. *J. Chem. Phys.* **2010**, 132, 224503.

(44) Panman, M. R.; Shaw, D. J.; Ensing, B.; Woutersen, S., Local Orientational Order in Liquids Revealed by Resonant Vibrational Energy Transfer. *Phys. Rev. Lett.* **2014**, 113, 207801.

(45) Thouless, D. J., Electrons in Disordered Systems and the Theory of Localization. *Phys. Rep.* **1974**, 13, 93-142.

(46) Choi, J.-H.; Ham, S.; Cho, M., Inter-Peptide Interaction and Delocalization of Amide I Vibrational Excitons in Myoglobin and Flavodoxin. *J. Chem. Phys.* **2002**, 117, 6821–6832.

(47) Woys, A. M.; Almeida, A. M.; Wang, L.; Chiu, C.-C.; McGovern, M.; de Pablo, J. J.; Skinner, J. L.; Gellman, S. H.; Zanni, M. T., Parallel β-Sheet Vibrational Couplings Revealed by 2D IR Spectroscopy of an Isotopically Labeled Macrocycle: Quantitative Benchmark for the Interpretation of Amyloid and Protein Infrared Spectra. *J. Am. Chem. Soc.* **2012**, 134, 19118-19128.

(48) Van Der Spoel, D.; Lindahl, E.; Hess, B.; Groenhof, G.; Mark, A. E.; Berendsen, H. J., Gromacs: Fast, Flexible, and Free. *J. Comput. Chem.* **2005**, 26, 1701-1718.

(49) Jorgensen, W. L.; Maxwell, D. S.; Tirado-Rives, J., Development and Testing of the OPLS All-Atom Force Field on Conformational Energetics and Properties of Organic Liquids. *J. Am. Chem. Soc.* **1996**, 118, 11225-11236.

(50) Berendsen, H. J. C.; Postma, J. P. M.; van Gunsteren, W. F.; DiNola, A.; Haak, J. R., Molecular Dynamics with Coupling to an External Bath. *J. Chem. Phys.* **1984**, 81, 3684-3690.

(51) Caleman, C.; van Maaren, P. J.; Hong, M.; Hub, J. S.; Costa, L. T.; van der Spoel, D., Force Field Benchmark of Organic Liquids: Density, Enthalpy of Vaporization, Heat Capacities, Surface Tension, Isothermal Compressibility, Volumetric Expansion Coefficient, and Dielectric Constant. *J. Chem. Theory Comput.* **2012**, 8, 61-74.

(52) Tobias, D. J.; Brooks, C. L.; Fleischman, S. H., Conformational Flexibility in Free Energy Simulations. *Chem. Phys. Lett.* **1989**, 156, 256-260.

(53) Hess, B.; Bekker, H.; Berendsen, H. J. C.; Fraaije, J. G. E. M., Lincs: A Linear Constraint Solver for Molecular Simulations. *J. Comput. Chem.* **1997**, 18, 1463-1472.

(54) Torii, H.; Tasumi, M., Model Calculations on the Amide-I Infrared Bands of Globular Proteins. *J. Chem. Phys.* **1992**, 96, 3379-3387.

(55) Jansen, T. L. C.; Knoester, J., Nonadiabatic Effects in the Two-Dimensional Infrared Spectra of Peptides: Application to Alanine Dipeptide. *J. Phys. Chem. B.* **2006**, 110, 22910-22916.

(56) Haynes, W. M., *Handbook of Chemistry and Physics: A Ready-Reference Book of Chemical and Physical Data*; CRC Press: Boca Raton, FL, 2016.

(57) Helbing, J.; Hamm, P., Compact Implementation of Fourier Transform Two-Dimensional IR Spectroscopy without Phase Ambiguity *J. Opt. Soc. Am. B* **2011**, 28, 171-178.

(58) Bloem, R.; Garrett-Roe, S.; Strzalka, H.; Hamm, P.; Donaldson, P., Enhancing Signal Detection and Completely Eliminating Scattering Using Quasi-Phase-Cycling in 2D IR Experiments. *Opt. Express* **2010**, 18, 27067-27078.

(59) Backus, E. H. G.; Garret-Roe, S.; Hamm, P., Phasing Problem of Heterodyne-Detected Two-Dimensional Infrared Spectroscopy. *Opt. Lett.* **2008**, 33, 2665-2667.

Chapter 3

Hydrophobic Collapse in N-methylacetamide-Water Mixtures

Aqueous N-methylacetamide solutions were investigated by polarization-resolved pump-probe and 2D infrared spectroscopy (2D-IR), using amide I mode as a reporter. The 2D-IR results are compared with molecular dynamics simulations and spectral calculations to gain insight into the molecular structures in the mixture. N-methylacetamide molecules and the water molecules tend to form clusters with “frozen” amide I dynamics. This is driven by a hydrophobic collapse as the methyl groups of the N-methylacetamide molecules cluster in the presence of water. Since the studied system can be considered as a simplified model of the backbone of proteins, the present study forms a convenient basis for understanding the structural and vibrational dynamics in proteins. It is particularly interesting to find out that a hydrophobic collapse, as the one driving protein folding, is observed in such a simple system.

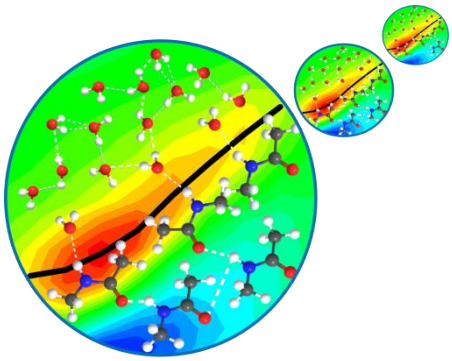

The current chapter is based on the following publication:

Evgeniia Salamatova, Ana V. Cunha, Robbert Bloem, Steven J. Roeters, Sander Woutersen, Thomas L. C. Jansen, and Maxim S.Pshenichnikov, *J. Phys. Chem. A* **2018**, 122, 2468-2478.

https://pubs.acs.org/doi/abs/10.1021%2Facs.jpca.8b00276

3.1 Introduction

The development of two-dimensional infrared (2D-IR) spectroscopy[1–3] led to extensive studies of biological and biochemical systems, with structural and dynamical properties of peptides and proteins[3,4] being in the focus. Amide I (CO stretch) vibrations were of particular interest due to their abundance in proteins and the resulting potential to access the information on structure and dynamics through their strong mutual coupling[5–12].

The mechanism of protein folding[13] is an important subject as misfolding of proteins leads to diseases like Altzheimer's and Parkinson's disease, type II diabetes, and cancer[14,15]. Great progress in the understanding of this complex process has been made in recent years[11,12,16–37]. The folding process can be steered by proteins called chaperones[38,39], influenced by salt bridge formation[40], and affected by pH and ionic strength. However, overall the hydrophobic collapse[27,41] and the framework model[16] have been proposed as the most common driving forces for protein folding. Understanding these mechanisms on a fundamental level for proteins is, however, challenging as sequence-specific effects inevitably play a role as well. The idea of this Chapter is to study the behavior of the amide groups forming the backbone of protein chains, when mixed with water. We want to eliminate the effect of sidechains to address the question to what extent the interactions between water and amide groups drive structural formation.

N-methylacetamide (NMA) is a convenient model molecule for studying such interactions. NMA is composed of a single peptide bond[42–48] (-CONH-), which contains a single amide I mode. Due to this structure, NMA is used as a model compound for the linkage between peptide units[44,49]. NMA can both donate and accept hydrogen bonds (HBs)[50] which makes it miscible with a wide range of solvents[42–44,48,51,52]. This has led to extensive experimental[42–45,48,52] and theoretical[47,48,53–55] studies of vibrational dynamics of the amide I mode of NMA[56] in different solvents.

The studies of NMA diluted in polar and non-polar solvents[42–45,48,51,52,54,56–65] provided important information on the relaxation pathways of the amide I mode and its spectral dynamics. An extensive study of the influence of the solvent on the amide I mode vibrational dynamics was performed by DeCamp *et al*.[48]. The amide I lifetime appeared to be weakly dependent on the particular solvent and amounted to 450 fs in heavy water[44], 380 fs and 430 fs in heavy water and DMSO, respectively[52] (with an ~2 ps tail reported in the latter study). In contrast, solvents

that form weak HBs lead to slower HB and reorientational dynamics[48,52]. Spectral dynamics of NMA molecules, diluted in water exhibit bimodal dynamics: a timescale of 50 fs was assigned to water librations while HB vibration dephasing occurred on a 180 fs timescale[48]. Recently, NMA bulk dynamics were studied by optical Kerr effect spectroscopy[66] and theoretically and experimentally by 2D IR spectroscopy[67]. In the former study, structural relaxation was observed to occur at the time scales of 30 ps and 180 ps at 300 K; both times accelerated by a factor of ~30 at 470 K. In the latter Chapter, an interesting interplay between HB and vibrational coupling was reported and interpreted from the viewpoint of the existence of highly-ordered HB chains where the transition dipoles are largely oriented parallel to each other along the chain of NMA molecules.

So far, the NMA dynamics have been studied for both diluted [48,52] and bulk[66,67] environments. However, in biological systems neither situation is relevant, as proteins and peptides form HBs with the aqueous surroundings. This situation can be only be mimicked by concentrated NMA-water mixtures. We will study such solutions to understand how the interactions between water and amide groups affect the HB structure and dynamics of the amide groups.

In this Chapter, we examine dynamics of mixtures of NMA molecules and water with 2D-IR spectroscopy and molecular dynamic simulations combined with spectral simulations. In the 50/50 molar % mixture the amide I lifetime is 450±100 fs which is in line with previous studies[43,44,67]. We show that such a mixture leads to clustering of NMA and water molecules, which leads to “frozen” dynamics at the ps time scale. The methyl groups in the NMA clusters tend to stick together suggesting a hydrophobic collapse. However, as evident from the anisotropy measurements, this does not fully prevent the movement of the vibrational excitations between amide I modes typical for bulk NMA, but its extent is limited to the NMA cluster size.

3.2 Results and Discussion

3.2.1 Linear absorption

The experimental and theoretical linear absorption spectra of the NMA-d_1/D_2O mixtures studied are shown in Figure 3.1. The experimental and theoretical spectra demonstrate similar trends: with increasing NMA-d_1 concentration, the spectra are blue shifted, become broader at intermediate concentrations, and narrow down in diluted NMA solutions. Both pure NMA spectra exhibit a high-frequency shoulder, which was earlier shown to have mixed HB – vibrational coupling origin.

The experimental spectra at X = 0.5-0.7 also show a noticeable high-frequency sub-band, while its appearance in the theoretical spectra is not as noticeable, except for the X = 0.3 case. The discrepancy most probably originates from the fact that the applied force fields overestimate the NMA clustering, which leads to more heterogeneity of the solution. Therefore, in what follows we have chosen to compare the experimental spectra of the X = 0.5 mixture with X = 0.3 of the simulated mixture (Figure 3.2) as representing the most similar heterogeneous case.

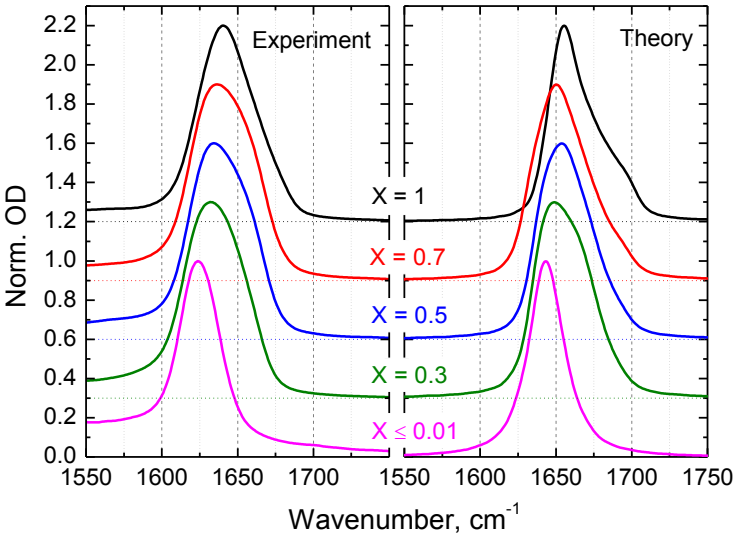

Figure 3.1 Comparison of linear experimental (left panel) NMA-d_1/D_2O mixtures and simulated (right panel) NMA/water absorption spectra at different molar fractions. The mole fraction X of NMA-d_1 is shown next to the corresponding spectrum.

To disentangle the origin of the main NMA band and the high-frequency sub-band, the linear spectrum of the very same system was calculated with the vibrational coupling between amide I modes set to zero (Figure 3.2). The spectra with zero coupling (hereafter denoted as uncoupled) are narrower and blue-shifted by ~13 cm^{-1} in comparison with the coupled spectra. This indicates a strong effect of vibrational coupling on the spectral lineshape as was previously reported for bulk NMA[67]. The high-frequency sub-band vanishes, which suggests that the sub-band originates from the vibrational coupling.

To verify this conclusion, all possible types of HB between NMA and water were extracted from the MD simulations. Geometric criteria[68] were used to determine if HBs were present between the molecules. For water-water and water-NMA HBs a common criterion defined for water[69] was used, while the criterion described in Ref.67 was used for NMA-NMA HBs. In total, there are 21 types of HB species

(see SI, section 3.4.1), which can be further categorized in three main groups according to the number of accepted HBs. Group I includes the free NMA (f-NMA) and NMA donating one HB (1d-NMA). The species in group II either accept one HB (1a-NMA) or donate one and accept one HB (1a-1d-NMA). Group III is characterized by two accepted HBs (2a-NMA) or two accepted and one donated HBs (2a-1d-NMA). No difference with respect to the origin of the HB donor (water or NMA) is made in this group categorization. The fraction of each group is depicted in Figure 3.3; group II is by far the most populated one.

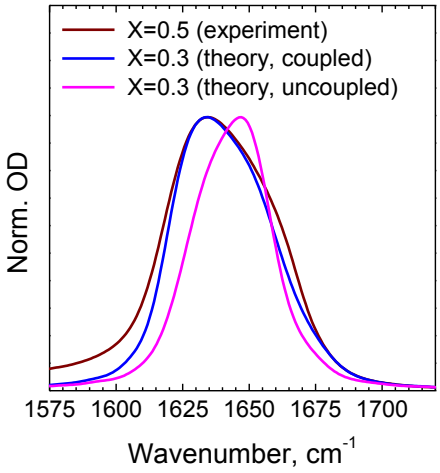

Figure 3.2 Linear FTIR spectrum of the NMA-d_1/D_2O solution (wine, X = 0.5) in comparison with the simulated coupled (blue) and uncoupled (magenta) spectra at X = 0.3.

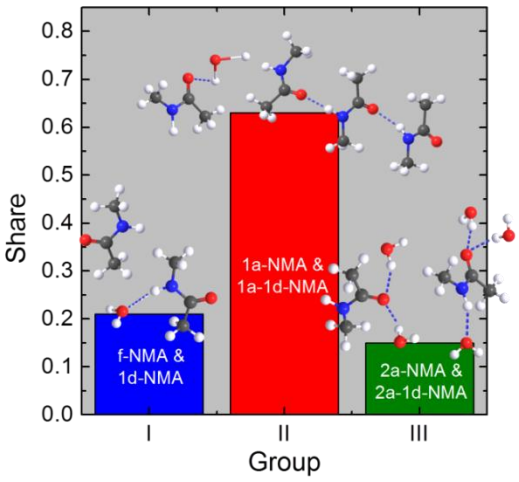

Figure 3.3 The fraction of each NMA-d_1/D_2O group. The number of accepted-donated HBs in the group is shown in the bar. Above the bar, representative corresponding structures are depicted.

To estimate the effect of the intermolecular coupling to the spectral features, the linear absorption spectra for each group were calculated in the static approximation for both coupled and uncoupled cases (Figure 3.4). The central frequency of group I is the most blue-shifted because of similarity of the effect of HB donation and no HB on the frequency of the C=O oscillator. In contrast, for group III the central frequency is the most red-shifted due to two accepted HBs. The dominant single HB accepting species (group II) absorbs at a frequency in the middle of the band. Of course, this is true only for the central frequencies: due to the broadness of the spectral distributions, there are double HB accepting complexes (group III) of which the frequency is blue-shifted as compared to free NMAs in group I, and vice versa.

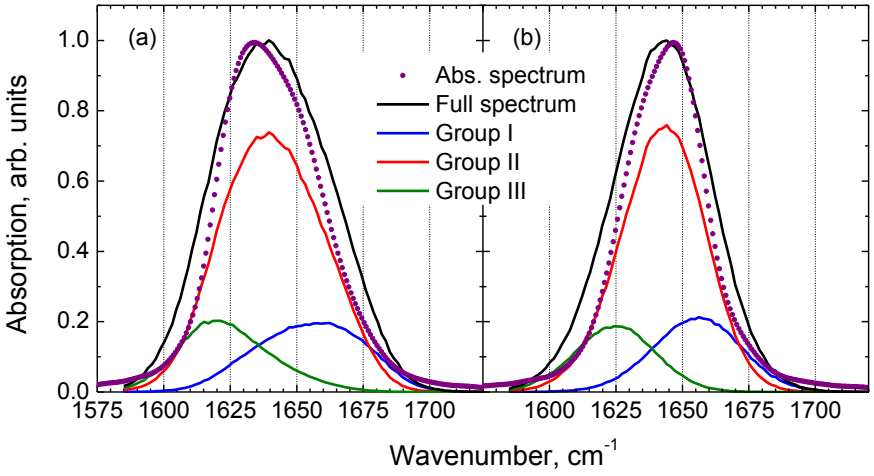

Figure 3.4 Linear absorption spectra in a static approximation of each group for coupled (a) and uncoupled (b) cases. For comparison, the full dynamic spectra from Figure 3.2 are also shown by the circles.

For each group the vibrational coupling leads to broadening of the spectra due to additional inhomogeneity in the coupling strengths (compare Figures 3.4a and 3.4b), similar to the observation in bulk NMA[67]. However, the red shift of the coupled spectra does not exceed 4-5 cm^{-1}, which is substantially lower than the 13 cm^{-1} red shift seen in the full dynamical calculations (Figure 3.2). This is because when calculating the static spectra for the different groups, the coupling between species belonging to different groups is neglected. Therefore, the similarity of the static structures tells us that the coupling between molecules belonging to different groups determines the shift in the dynamics spectra, and therefore the molecules belonging to the same group are dispersed throughout the liquid. A comparison between full static spectra and linear absorption spectra

simulated with the NISE approach (i.e. accounting for motional narrowing effects) shows that the HB dynamics lead to narrowing of both the coupled and uncoupled spectra hereby proving the importance of the motional narrowing effects.

In principle, the uncoupled spectra in Figure 3.2 could be obtained experimentally by using isotopically diluted NMA where the carbonyl carbon or oxygen is replaced by ^{13}C and/or ^{18}O which leads to red-shifting of the amide I absorption by 20-60cm^{-1} [70]. This is comparable to typical values of vibrational couplings of <20 cm^{-1} [71] so the intermolecular coupling is not fully suppressed.

3.2.2 Pump-probe

To extract the amide I mode lifetime, the frequency- dependent isotropic component of the pump-probe signal was extracted from the experimental spectra as:

$$I_{iso}(t) = \frac{I_{\parallel}(t) + 2 \cdot I_{\perp}(t)}{3} \qquad \text{(Eq. 3.1)}$$

where $I_{\parallel}(t)$ and $I_{\perp}(t)$ are the parallel and perpendicularly polarized components, respectively, of pump-probe signal with respect to the pump. The isotropic transient spectra for an NMA-d_1/D_2O with X = 0.5 recorded at several pump-probe delays are shown in Figure 3.5. The transient spectra consist of a positive bleaching component (at ~1650 cm^{-1}) and a negative induced absorption component (at ~1615 cm^{-1}). The transient spectrum at 5 ps is drastically different from those at shorter times. This is ascribed to thermal effects[72] that begin to dominate the pump-probe signal at longer times.

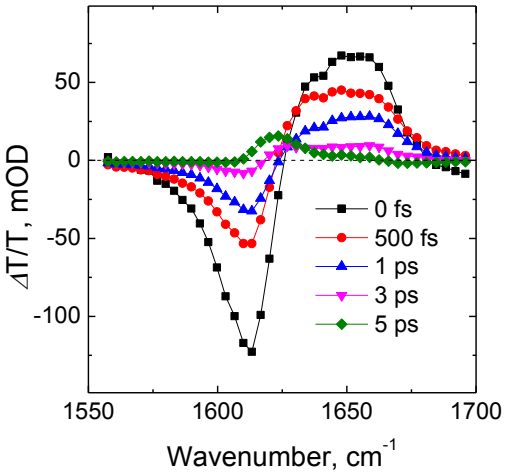

Figure 3.5 Isotropic transient spectra of X = 0.5 NMA-d_1/D_2O mixture at different delay times (as shown in the legend).

To determine the time scales of the population relaxation and thermalization, we used the isotropic pump-probe transients at the extreme points of bleaching/stimulated emission (~1650 cm^{-1}) and induced absorption (~1615 cm^{-1}) frequencies, along with the transient near the compensation point at ~1625 cm^{-1} (Figure 3.6). The latter represents the thermalization signal that is the least affected by the population dynamics. Its set-up time of 4.2±0.3 ps is apparently much longer than the population relaxation time, which hints that a four-level model[73] (with the ground, excited, intermediate and hot-ground states) should be used to describe the transients. The lifetime of amide I mode calculated from such a model amounted to ~450±100 fs. While the obtained lifetime of the amide I mode corroborates the previous results, it might be affected by the presence of HB configurations with different lifetimes, and mixing up frequencies of excited-state absorption and bleaching/stimulated emission of these species. Nonetheless, the value of 450 fs is sufficiently reliable for estimating the time window provided for 2D-IR experiments (~1.5 ps).

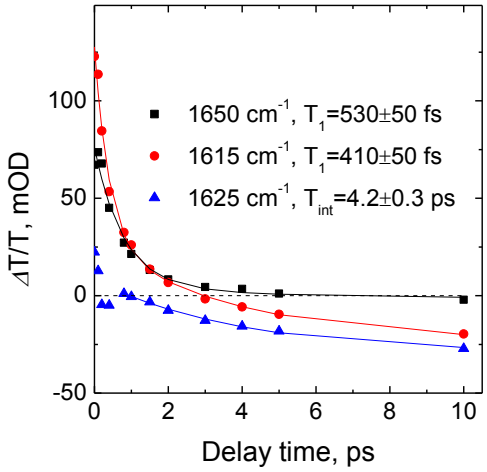

Figure 3.6 Representative pump-probe transients of X = 0.5 NMA-d_1/D_2O mixture at the maximum of bleaching/stimulated emission (black symbols), induced absorption (red symbols), and the compensation point (blue symbols). The fits obtained from the four-level thermalization model, are shown by the solid lines; the respective relaxation times (the excited state lifetime T_1 and the thermalization time T_{int}) are given in the legend. The sign of the 1615 cm^{-1} transient was inverted to allow easy comparison with the other transients.

3.2.3 2D-IR spectroscopy

The linear spectrum does not contain any information about the NMA-d_1/D_2O dynamics. Such information can be extracted from non-linear 2D spectra (Figure 3.7). All spectra are strongly elongated along the diagonal, which suggests “frozen” dynamics. However, more careful inspection reveals the presence of two

peaks with central frequencies at ~1635 cm^{-1} and ~1660 cm^{-1} (see the linear spectra in Figure 3.2 for comparison). Therefore, the diagonal elongation might result from a simple combination of the two peaks each of which is not necessarily elongated diagonally (providing there is no chemical exchange between the peaks, see SI, section 3.4.2). Hence, we decided to perform the center line slope (CLS)[74,75] analysis in two separate regions which correspond to the two peaks in Figure 3.2.

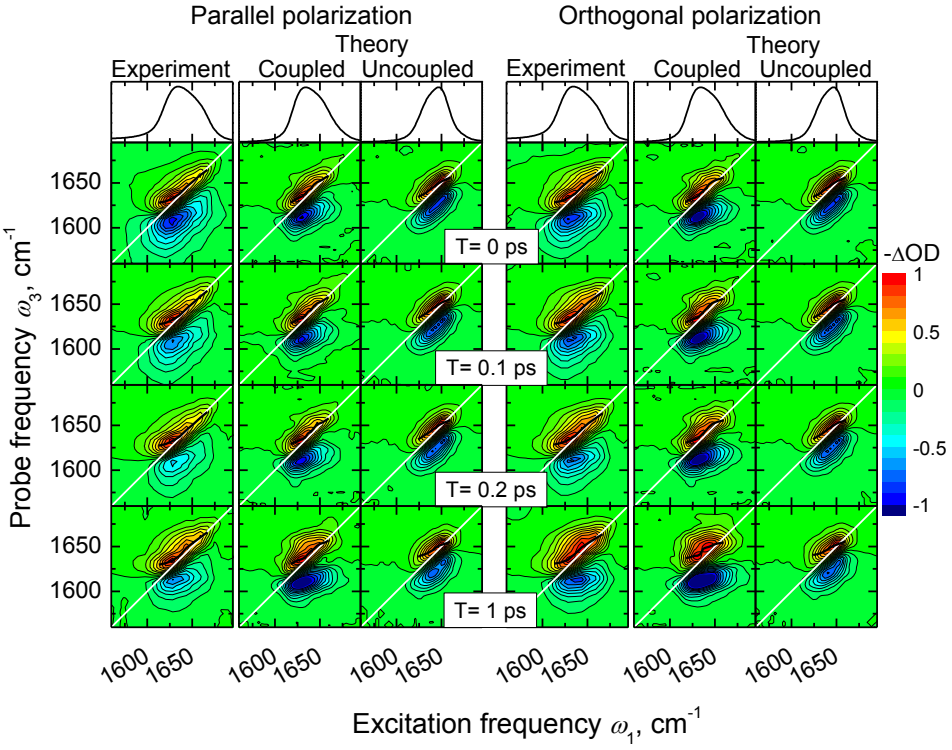

Figure 3.7 Normalized 2D-IR spectra of X = 0.5 NMA-d_1/D_2O mixture at several representative waiting times T. The experimental (the left hand columns) and the simulated coupled and uncoupled (the middle and right-hand columns, respectively) spectra are shown for parallel and orthogonal polarization arrangement. Red and blue colors represent the bleaching/stimulated emission and induced absorption, respectively. The equidistant contours are drawn with 10% steps from the maximal amplitude. The thick black lines show the results of the CLS analysis in the following frequency regions: experiment $1613<\omega_1<1667$ cm^{-1}, theory (coupled) $1617<\omega_1<1660$ cm^{-1} and theory (uncoupled) $1624<\omega_1<1660$ cm^{-1}.

In the low-frequency region (Figure 3.8a), the experimental CLS values at short times are about 0.55, which indicates a substantial contribution of the homogeneous broadening, in accordance with the theoretical calculations. Most probably, this broadening originates from fast bath modes, such as the water librations. In contrast, the CLS values at short times in the high-frequency region

(Figure 3.8b) are close to unity, indicating that this region of the spectrum is primarily inhomogeneously broadened (see Figure 3.4 and the discussion around it). The small rise at short waiting times most probably originates from the pulse overlap region and/or nonresonant (instantaneous) background response.

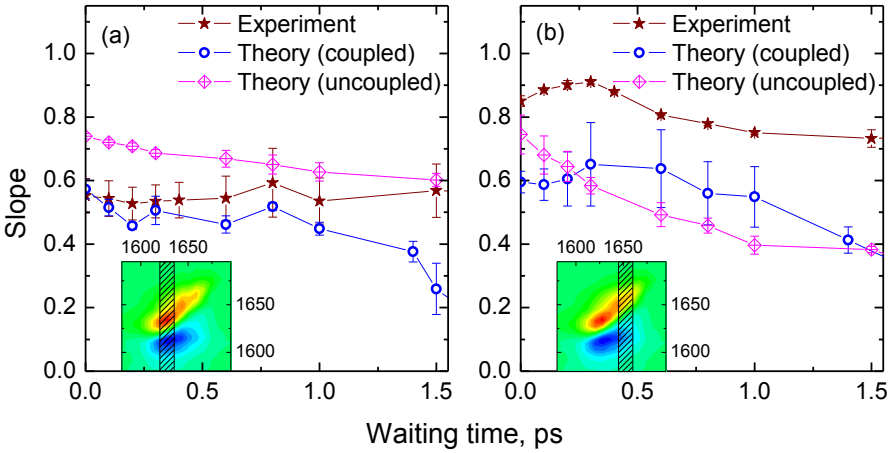

Figure 3.8 CLS analysis of the 2D spectra (parallel polarization) in the amide I mode region performed at the low (experiment, coupled: $1620<\omega_1<1636$ cm^{-1} and uncoupled: $1633<\omega_1<1648$ cm^{-1}) and high (experiment, coupled: $1644<\omega_1<1659$ cm^{-1} and uncoupled: $1656<\omega_1<1670$ cm^{-1}) frequencies. The region of the CLS analysis is shown in the inset as a shaded area. Theoretical values are computed for the coupled case (blue circles) and uncoupled (magenta diamonds).

The theoretical CLS values in the low-frequency region capture the experimental ones rather well (Figure 3.8a). However, the theory predicts more homogeneity in the high-frequency region (Figure 3.8b); this may in part be due to the overestimation of vibrational couplings[76-77] (which is supported by the fact that the CLS values are higher when the coupling is set to zero; see Figure 3.8), and overestimation of frequency fluctuations of the free species. The latter likely arise as the molecular polarizability in the point charge based force fields used here are accounted for by scaled point charges to match the average dipole moment in the liquid and configurations far from this average are described less accurate[54,78]. We also note that the coexistence of free and clustered NMA molecules might lead to a vibrational lifetime in the low-frequency region that differs from the lifetime in the high-frequency region (see discussion in Section 3.2.2).

At the main peak position the CLS values for the uncoupled simulations are generally higher than for the simulations accounting for the coupling (Figure 3.8a). In the high-frequency region the CLS values are much more similar (Figure 3.8b). This suggests that the couplings are more important for the NMA molecules

involved in HB. One must of course keep in mind that when the coupling is included, the excitations are no longer localized on a specific HB type.

For all waiting times, the experimental and theoretical CLS values do not change substantially in both frequency regions which suggests “frozen” dynamics of the amide I mode at the ps time scale. Such “frozen” dynamics have been reported earlier for water in reversed micelles[79] and around hydrophobic groups[80]. This effect was explained as breakage of the 3D HB network amongst the water molecules. As we concluded from the analysis of the static spectra (Figure 3.4), different types of HB species are dispersed in the mixture. From 2D spectroscopy, we inferred that the dispersed structures are static at least at the time scale of a few ps. This situation is visualized in Figure 3.9 where a snapshot from MD simulations clearly shows the phase separation of the mixture onto NMA clusters (in the center) surrounded by the water molecules (at the periphery).

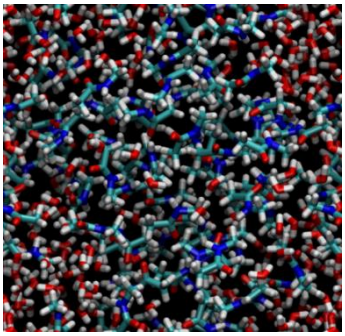

Figure 3.9 A snapshot from the MD simulation of the NMA-water mixture. Oxygen atoms are shown in red, hydrogen in white, carbon in cyan, and nitrogen in blue.

To quantify the clustering effect, we calculated the joint angular-radial distribution functions (JARDFs) of the NMA/water mixture and compared them with JARDFs of bulk NMA (Figure 3.10). The initial peak at ~0.48 nm corresponds to HBs between amide units in the first solvation shell. After this, the JARDF for NMA contains apparent recurrences, both in the radial and angular dependences, which are also presented in less pronounced form in JARDF of the mixture.

The features of the JARDF revealing the liquid structure are highlighted in Figure 3.11 where two particular cuts of the JARDFs are depicted, one in the radial direction at a fixed angle, and another one at an angle direction at a fixed distance. The main peak of the bulk NMA JARDF has a higher amplitude than its mixture counterpart, which reflects more ordering amongst HBs between amide units already in the first solvation shell. Furthermore, several recurrences follow which correspond to HBs between amide units in the second and third solvation shells.

This is not surprising given the previous findings that NMA in bulk forms chain-like structures with well-defined orientation of the HBs between amide units [67]. These features are less pronounced in the NMA-water mixture, lending additional support for the system heterogeneity. The radial cut shows a similar trend: a relatively narrow (~50°) distribution of C=O angles for bulk NMA, and a much broader (~65°) distribution for the NMA-water mixture. These observations lead to the conclusion that the NMA-water mixture is not as well-organized as bulk NMA, and that the formation of the HB chains of NMA molecules is largely destroyed by water molecules.

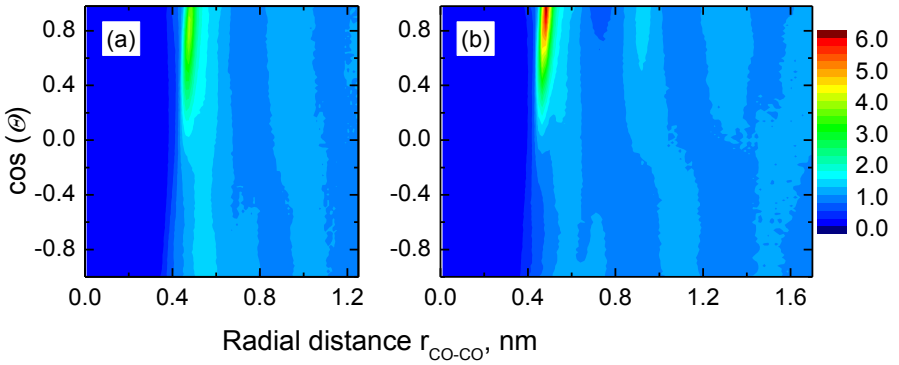

Figure 3.10 The joint angular-radial distribution functions of (a) NMA-water mixture and (b) bulk NMA. Θ is the angle between the pairs of C=O bond vectors ($cos(\Theta)$ = 1 and $cos(\Theta)$ = -1 for the parallel and antiparallel bond vectors, respectively), and $r=r_{CO\text{-}CO}$ is the distance between the centers of pairs of C=O bonds. The color map corresponds to the occurrence of formation the pair of C=O bonds: the red color shows the high occurrence, while the blue is used for low occurrence. Both distributions are normalized to unity at large r.

The nanoscopic phase separation in the mixture can also be interpreted from the perspective of water molecules (Figure 3.12). The radial distribution function (RDF) for O…O distances of the NMA-water mixture has a higher amplitude initial peak and stronger recurrences than the RDF of bulk water[81]. This indicates that, the water molecules in the mixture form extended clusters, with a better defined water structure than in the bulk. This is well in line with many reported studies of water at molecular interfaces[82–86]

To further quantify the clustering of NMA molecules, the RDF between methyl groups (C…C distance) of the NMA molecules were calculated (Figure 3.13) and compared with that of bulk NMA. The probability to find two NMA methyl groups at a distance of 0.38 nm distance is higher in the mixture compared to bulk NMA. This makes us conclude that in the mixture, the NMA molecules tend to form clusters in which the hydrophobic methyl groups stick together. This, thus, resembles the hydrophobic collapse observed in the protein folding process[27], but in this case it is

solely driven by the presence of the small methyl groups in the NMA molecule, instead of the large hydrophobic sidechains present in real proteins.

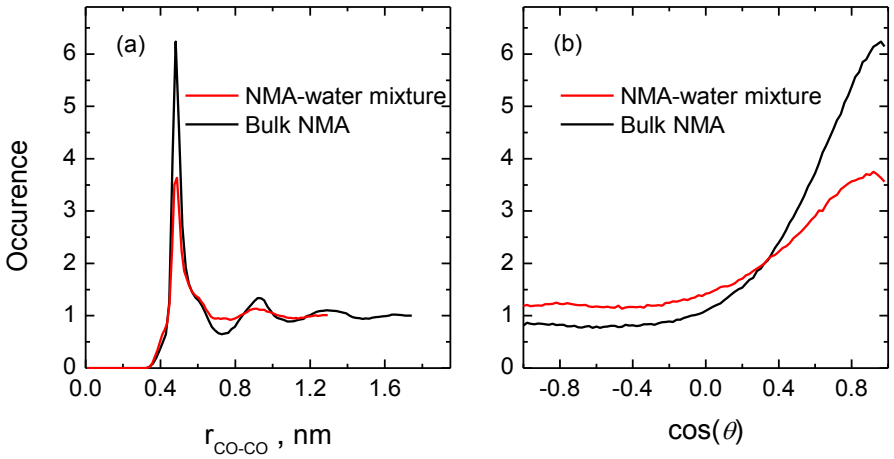

Figure 3.11 (a) The radial distribution function of NMA mixture and bulk NMA at *cos(Θ)* =1 and (b) the angular distribution function of dissolved and bulk NMA at *r*=0.48nm

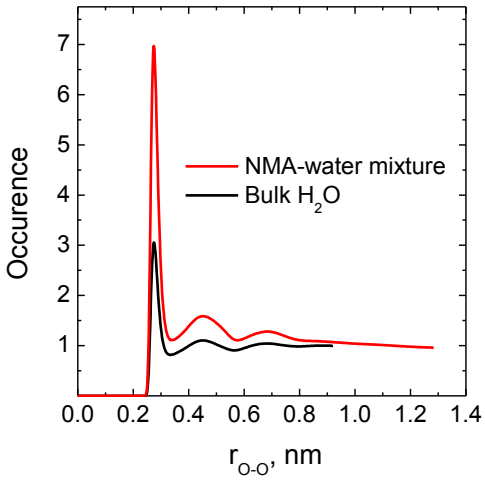

Figure 3.12 Radial distribution functions of water oxygen for NMA-water mixture (red) and bulk water (black). Both distributions are normalized to unity at large *r*.

To verify the destabilizing effect of water on the structural order of NMA, we measured and calculated the anisotropy decay (Figure 3.14). Both the experimental and calculated coupled anisotropies decay much faster than the rotational correlation function (RCF) but with the same rate as the population transfer regardless the spectral region. This is in a sharp contrast with bulk NMA where the anisotropy decays faster than RCF but slower than the population transfer. The latter was interpreted as vibrational excitation moving through the transition dipole network ordered by HBs. Apparently, the current situation is very different: the vibrational excitation is still mobile (the anisotropy decays faster than RCF) but the orientations of the transient dipole moments are not mutually aligned so that the anisotropy is quickly scrambled. The vibrational excitation in the mixture is delocalized over 8.6 NMA molecules on average as compared to 42 in the bulk[67] (as determined using the inverse participation ratio[87]). In the mixture, the delocalization is thus strongly reduced as it has to be localized inside the NMA cluster. All these observation confirm our conclusion that water induces a hydrophopic collapse in NMA destabilizing the intermolecular HBs and lowering the structural order.

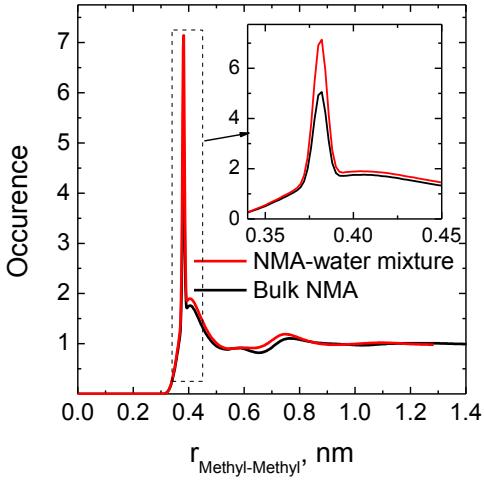

Figure 3.13 Methyl-methyl RDF of NMA-water mixture (red) in comparison with bulk NMA (black). Both distributions are normalized to unity at long distances *r*.

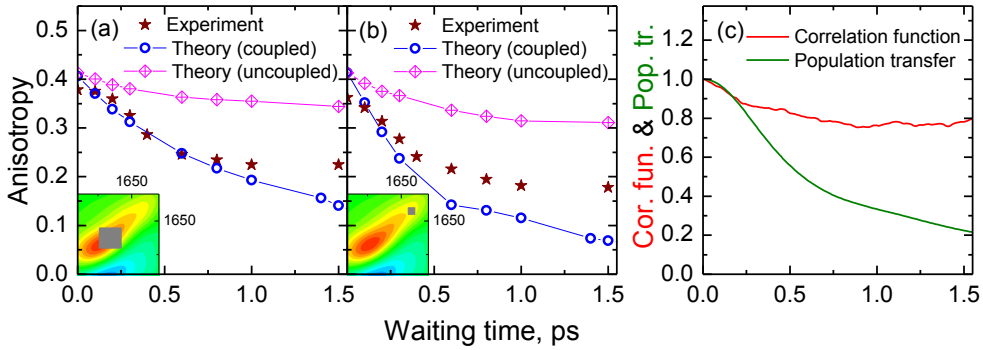

Figure 3.14 The anisotropy decay of the main (a) and high-frequency (b) absorption peaks for experimental and theoretical spectra. The anisotropy values were calculated from the integration of the 2D spectra over the region shown in the corresponding inset; for the uncoupled case, the spectral area around the main peak at ~1650 cm^{-1} (Figure 3.2) was taken. (c) rotational correlation function (RCF) and population transfer function obtained from MD simulations. Note that the uncoupled case produces the anisotropy decay similar to the RCF as expected from the localized (immobile) vibrational excitation.

3.3 Conclusions

In this Chapter, we have studied the NMA-water mixtures with linear and non-linear IR spectroscopy. The lifetime of the amide I mode has been found to be similar the previous reports of diluted and the bulk NMA solutions. We revealed that adding water to NMA leads to disruption of the HB chains of NMA molecules, which were described in Chapter 2. Instead, solvation results in the formation of water and NMA clusters where the amide I dynamics are "frozen", at least at the ps timescale. Curiously, only the frequency and rotational dynamics are frozen while the anisotropy is not and does decay at the ~1 ps time scale. This is because the excitation is mobile and therefore samples a few amide I modes with similar frequencies but different orientations. The former leads to constant CLS values (after the initial drop), as the excitations tend to be shared between vibrations with similar frequency, while the latter results in the anisotropy decay. It would be interesting to investigate if the water dynamics are frozen, too (similarly to the recently-reported "mayonnaise effect" [88]); these experiments are underway.

In our opinion, the results obtained herein could form a basis for understanding the hydration structure and (vibrational) dynamics of more complex biological systems than the NMA-water system studied in the current work. Real proteins may, for example, have charged groups at the surface – a complication that could be avoided using simpler systems such as NMA as a testing ground. We clearly find that even without an actual backbone or side chains the amide unit is experiencing a kind of hydrophobic collapse when exposed to water. This leads to disruption of the long-range ordered HB network between NMA molecules

observed in bulk NMA[67], and to clustering of both NMA and water molecules. The resulting spectral dynamics reflecting the HB dynamics, at least in the NMA phase, are “frozen” as compared to the dynamics in the bulk. This suggests that the hydrophobic collapse is an intrinsic property of the amino acid backbone units, which may of course be enhanced by hydrophobic side chains or suppressed by hydrophilic ones.

3.4 Materials and Methods

3.4.1 Sample preparation

We used NMA with deuterated peptide bond and deuterated water (D_2O) to avoid unwanted overlap of the C=O stretching mode at ~1650 cm^{-1} with the HOH bending mode[89] (~1645 cm^{-1}). N-methylacetamide-d_1 (NMA-d_1) with isotopic enrichment >99% was obtained from CDN isotopes; deuterium oxide (D_2O) with isotropic purity >99.9% of the D atom was purchased from Sigma-Aldrich. Both chemicals were used without any further purification.

NMA-d_1 is a solid at the room temperature (~22°C) so it was placed on a heating plate of 40°C until it was completely melted. After that, liquid NMA-d_1 was mixed with D_2O in precalculated volumes in order to obtain mixtures with variable mole fractions of NMA-d_1 (hereinafter the mole fraction of NMA in solution is denoted as X[90], i.e. X = 1 and X = 0 correspond to pure NMA-d_1 and heavy water, respectively) . Approximately 1.5 µl of the NMA-d_1/D_2O solution was squeezed between two 1 mm thick CaF_2 windows, which were preheated up to T=40°C to ensure the homogeneous distribution of the sample all over the area. In order to minimize the contact of the samples with air, the assembly was placed in a sealed cylindrical sample holder. The sample thickness (estimated from the absorbance) was ~3 µm assuming that the solution was spread uniformly between the 1inch diameter CaF_2 windows.

To avoid any contact with air moisture, sample preparation was performed under nitrogen atmosphere. During the experiments, to avoid potential crystallization of NMA-d_1 at high concentration, the temperature of samples were uniformly maintained at temperature of 30.5±1°C by a thermostat controlled by a thermocouple.

3.4.2 IR Spectroscopy

An FTIR-spectrometer *Vertex-70* purged with dry nitrogen was used for recording the FTIR absorption spectra in the spectral range of 1550-1750 cm^{-1}. The spectral

resolution was ~2 cm^{-1}; 32 scans were averaged for every absorption spectrum. The maximal OD in the region of interest was ~0.6.

An interferometer platform used as a base for the collinear 2D IR setup is described elsewhere[91]. In short, an IR pulse (~25 μJ of energy, 135 fs in duration, 140 cm^{-1} FWHM spectral width), centered at 1640 cm^{-1} was split into two pumps (90% of the total intensity) of equal intensity, probe and reference. The time difference between probe and reference pulses was set at 40 ps to avoid any interference. A wobbler in the probe beam path generated a -π, 0, +π, 0 phase sequence[92] for subsequents pulse (1 kHz repetition rate) to remove sample scattering. Before the sample the polarization of the pump was rotated by a λ/2 waveplate by 45° with respect to the pump polarization. After the sample, either the parallel or the perpendicular polarization of the probe beam was selected by a polarizer. The probe spectrum was detected by one of the 2x32 pixel MCT array rows (Infrared Associates) to provide the ω_3 dimension of the 2D spectra. Detection of the reference beam spectrum was carried out by the second array row of the MCT spectrometer. To increase the signal-to-noise ratio, the probe spectrum was normalized by the reference spectrum for each laser shot. At fixed waiting times *T* between the probe and the latest pump pulse the delay between two pump pulses, t_1, was scanned up to 2 ps with fast scanning approach[91]. The normalized probe spectrum was averaged over the wobbler-generated phase sequence to extract the nonlinear response related to all three pulses (two pumps and the probe), zeropadded to 4 ps, and Fourier-transformed to obtain the ω_1 dimension with the phase correction applied [93]. For the pump-probe measurements, one of the pump beams was used.

The interferometer together with the sample and detection sections were purged with dry air to prevent water peaks in the IR spectrum and to minimize the sample adsorption of the water vapor.

3.4.3 Theory

The molecular modelling simulations were performed with the GROMACS suite 4.6.1 [94] using a combination of the OPLS-AA[95] force field and the SPC/E water model [78] to describe the NMA/water mixture, with variable NMA/water content. The production run of 1 ns at 27°C was performed at constant volume and the coordinates of all atoms using 1 fs time steps. Snapshots were stored at each 10 fs for analysis and spectral modeling. The temperature was kept constant using the Berendsen thermostat[96], and a 1.1 nm cutoff was used for both Lennard-Jones and Coulomb interactions. The truncation of the Lennard Jones potential was compensated by introducing analytical corrections to pressure and potential energy[97]. The long range Coulomb interactions were treated using Particle Mesh

Ewald method, with a grid step of 0.16 nm, and a convergence of 10^{-5} [98]. All bonds were constrained using the LINCS algorithm[99].

The spectral modelling was performed using the Numerical Integration of Schrödinger Equation (NISE) method[49,100]. The time dependent Schrödinger equation was solved numerically for the time-dependent amide I Hamiltonian:

$$H(t) = \sum_{i}^{N} \omega_i(t) B_i^{\dagger} B_i \; - \frac{\Delta}{2} \sum_{i}^{N} B_i^{\dagger} B_i^{\dagger} B_i \; B_i \; + \sum_{i \neq j}^{N} J_{ij}(t) B_i^{\dagger} B_j \; - \sum_{i}^{N} \vec{\mu}_i(t) \vec{E}(t) \left(B_i^{\dagger} + B_i \; \right)$$

(Eq. 3.2)

where $B_i^{\dagger}$ and B_i are the bosonic creation and annihilation operators, $\omega_i(t)$ is the time dependent fundamental amide I frequency for the i'th molecule, and $\vec{\mu}_i(t)$ is the corresponding transition dipole. The anharmonicity, Δ_i, was kept constant at 16 cm-1 44. The amide I site frequencies, $\omega_i(t)$, were calculated using the Jansen electrostatic map 53, which was reported to work well with the OPLS-AA force field 77. The long range couplings between the different amide I units were calculated using the transition charge coupling (TCC) model 8,55, where a charge, q_n, and a transition charge, dq_n, and a normal mode coordinate, $\vec{v}_{n_i}$, are assigned to each atom of the amide I unit. The TCC model has the form:

$$J_{ij} \; = \; \frac{1}{4\pi\varepsilon_0} \sum_{n,m} \left(\frac{dq_n dq_m}{\left| \vec{r}_{n_i m_j} \right|} - \frac{3 q_n q_m \left(\vec{v}_{n_i} \cdot \vec{r}_{n_i m_j} \right) \left(\vec{v}_{m_j} \cdot \vec{r}_{n_i m_j} \right)}{\left| \vec{r}_{n_i m_j} \right|^5} \right.$$
$$\left. - \frac{dq_n q_m \vec{v}_{m_j} \cdot \vec{r}_{n_i m_j} + q_n dq_m \vec{v}_{n_i} \cdot \vec{r}_{n_i m_j} - q_n q_m \vec{v}_{n_i} \cdot \overrightarrow{v}_{m_j}}{\left| \vec{r}_{n_i m_j} \right|^3} \right)$$

(Eq. 3.3)

Here, the subscripts n, and m, number the atoms, which belong to different amide I local modes at molecules i, and j, respectively. The distance vector between two atoms in the involved molecules is given by $\vec{r}_{n_i m_j}$. The values of the used parameters are given in Ref.18.

3.5 Supporting Information

3.5.1 Types of the HB spices

a) **Group I** includes the free NMA (f-NMA) and NMA donating one HB (1d-NMA) and consists of three different types.

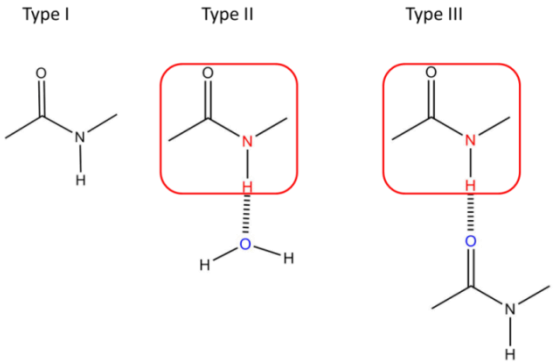

Figure S3.1 The schematic representations of NMA-water species, which were bundled in group I.

b) **Group II** includes the NMA-water species, which either accept one HB (1a-NMA) or donate one and accept one HB (1a-1d-NMA) and consists of six types.

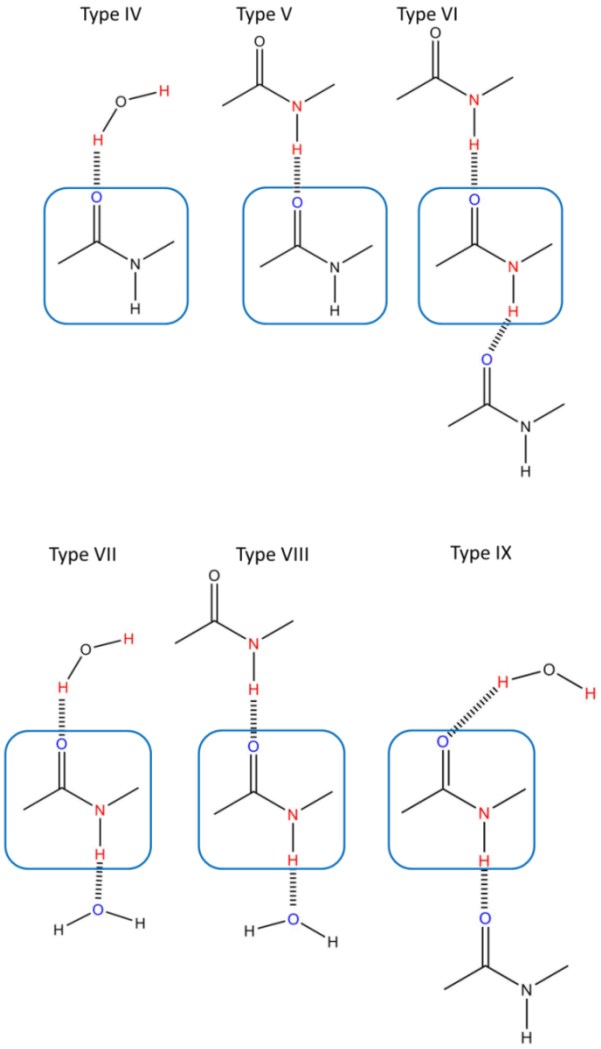

Figure S3.2 The schematic representations of NMA-water species, which were bundled in group II

c) **Group III** consists of the NMA-water species, which either accept two HBs (2a-NMA) or accept two and donate one HB (2a-1d-NMA). This group consists of nine types.

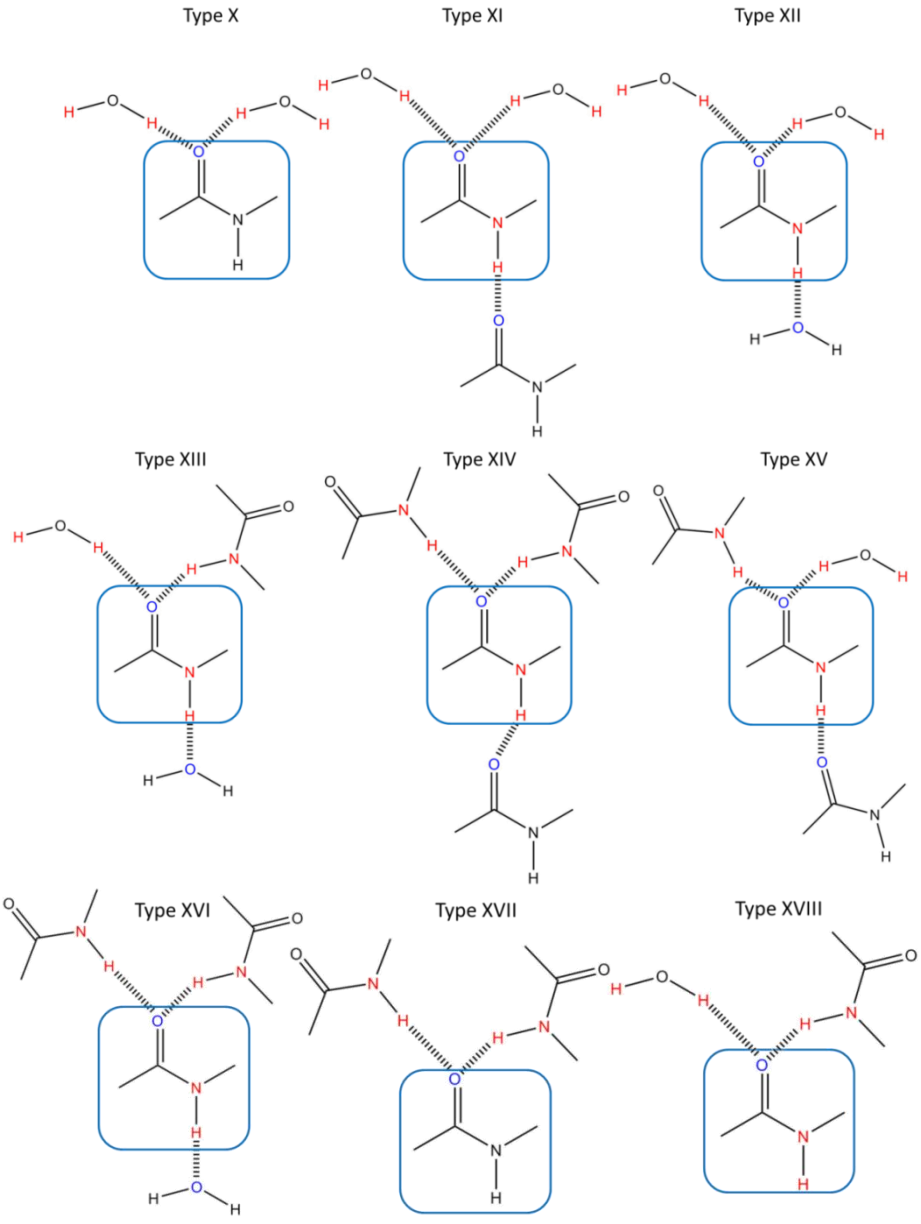

Figure S3.3 The schematic representations of NMA-water species, which were bundled in group III

d) **Other NMA species.** These NMA-water species are transient species found to either donate two HBs, or accept three HBs according to the used hydrogen bond criteria. These are not assigned to any of the groups I-III.

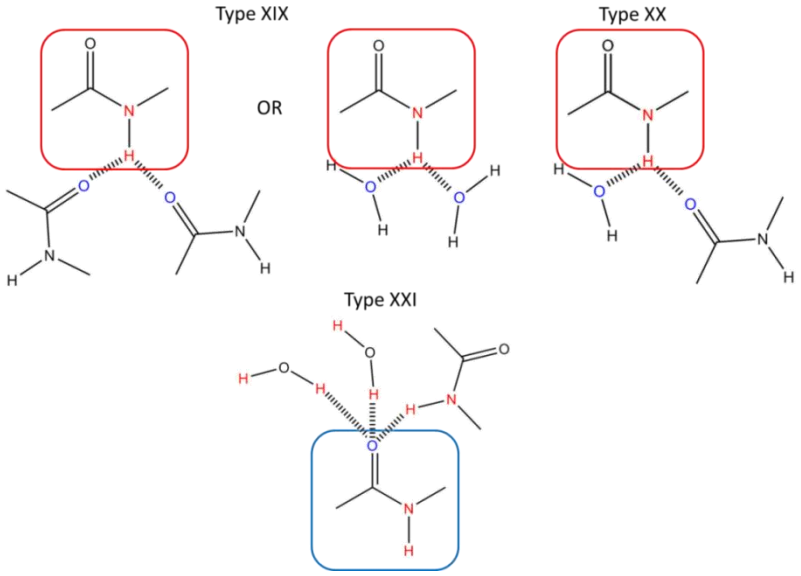

Figure S3.4 The schematic representations of transient NMA-water species, which were not assigned to any of the three groups.

3.5.2 2D-IR spectra of NMA-water mixture at different waiting times

a) Experimental spectra of NMA-d_1/D_2O mixture at X = 0.5

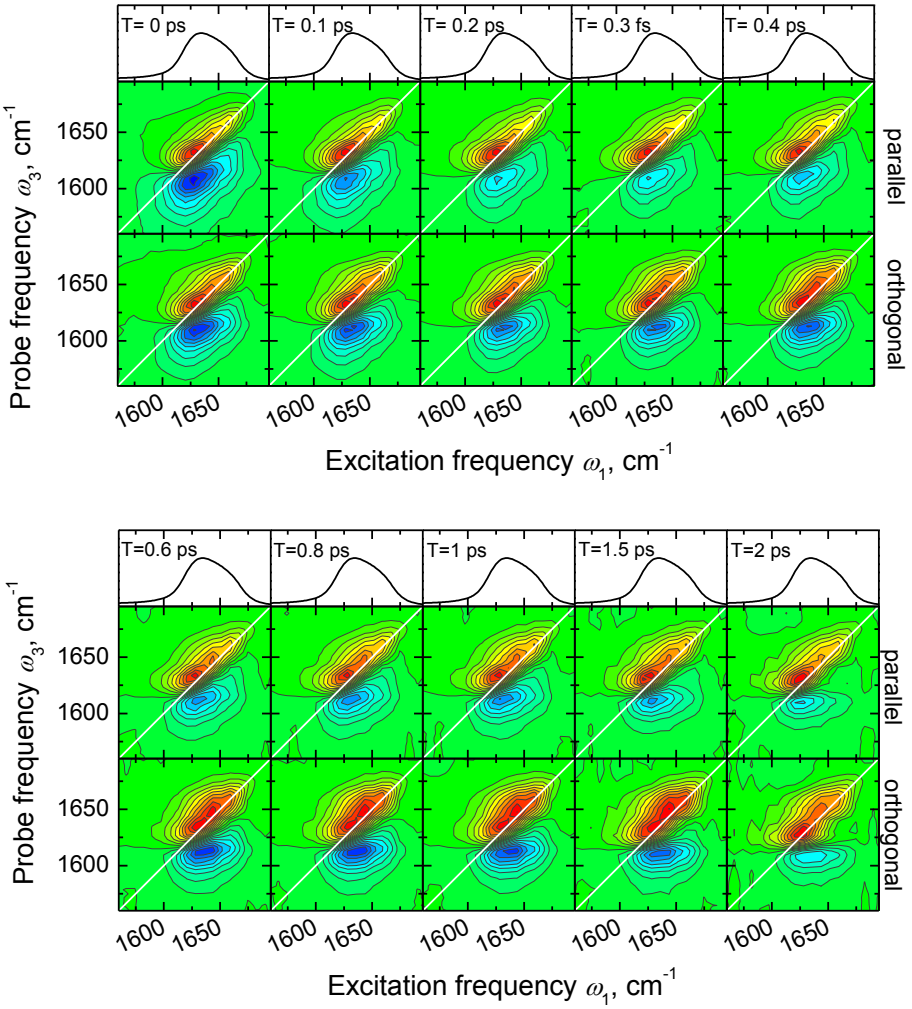

Figure S3.5 2D-IR experimental spectra of NMA-d_1/D_2O solution at different waiting times and two different polarizations.

b) Theoretical coupled spectra of NMA/water mixture at X = 0.3

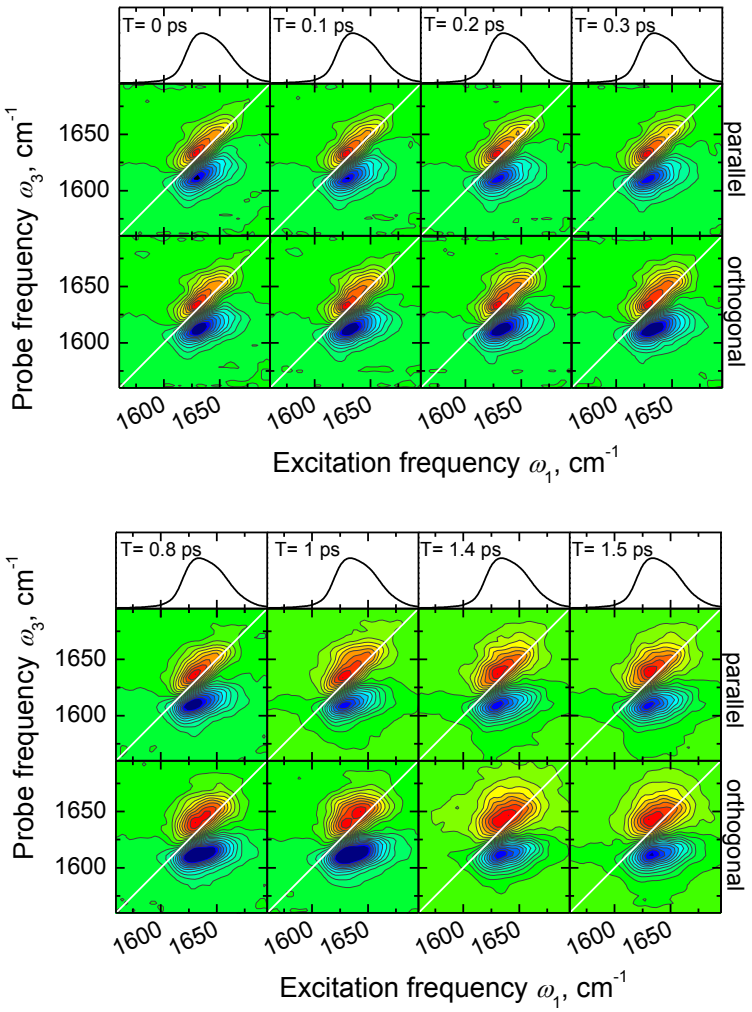

Figure S3.6 2D-IR theoretical coupled spectra of NMA/water solution at different waiting times and two different polarizations.

c) Theoretical uncoupled spectra of NMA/water mixture at X = 0.3

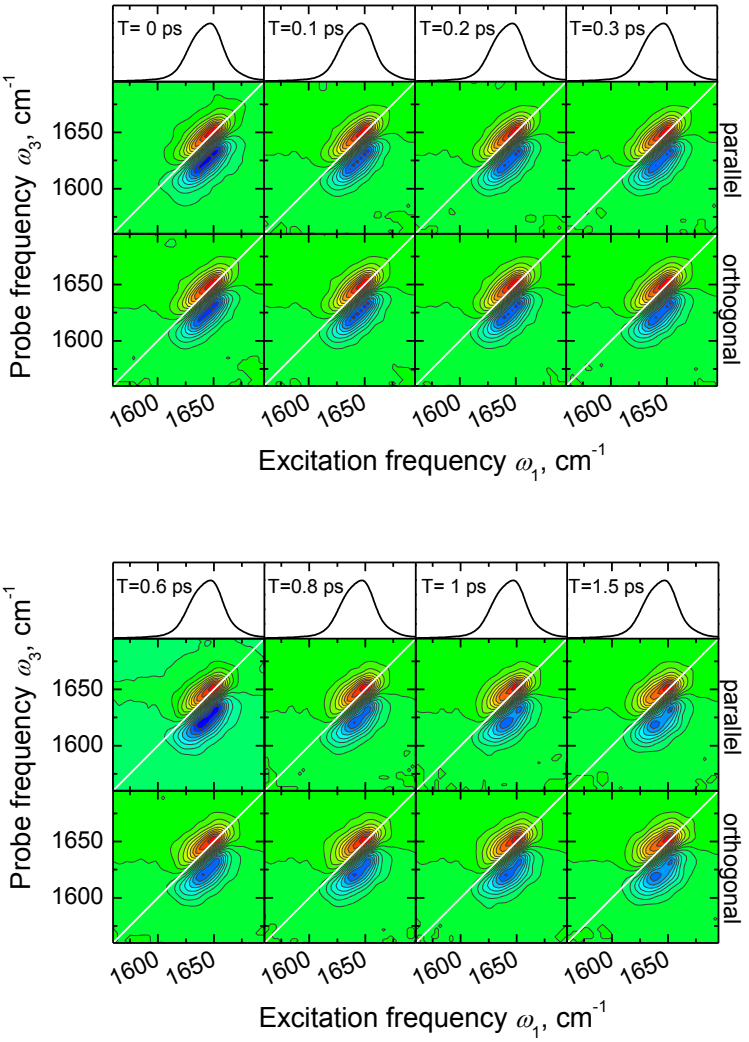

Figure S3.7 2D IR theoretical uncoupled spectra of NMA/water solution at different waiting times and two different polarizations.

Author Contributions

ES, RB, SJR performed the 2D-IR experiments under the supervision of SW. AC and TLCJ performed all theoretical calculations; TLCJ and MSP supervised the research. The manuscript was written by ES under the supervision of TLCJ and MSP.

3.6 References

(1) Hamm, P.; Zanni, M. T. *Concepts and Methods of 2D Infrared Spectroscopy*; Cambridge University Press: Cambridge, U.K., 2011.

(2) Cho, M. *Two-Dimensional Optical Spectroscopy*; CRC Press: Boca Raton, FL, 2009.

(3) Cho, M. Coherent Two-Dimensional Optical Spectroscopy. *Chem. Rev*. **2008**, 108, 1331–1418.

(4) Baiz, C. R.; Reppert, M.; Tokmakoff, A. Introduction to Protein 2D IR Spectroscopy. *In Ultrafast Infrared Vibrational Spectroscopy*; Fayer, M. D., Ed.; Taylor & Francis: New York, 2013; pp 361–404.

(5) Jansen, T. L. C.; Knoester, J. Two-Dimensional Infrared Population Transfer Spectroscopy for Enhancing Structural Markers of Proteins. *Biophys. J.* **2008**, 94, 1818–1825.

(6) Demirdöven, N.; Khalil, M.; Golonzka, O.; Tokmakoff, A. Correlation Effects in the Two-Dimensional Vibrational Spectroscopy of Coupled Vibrations. *J. Phys. Chem. A* **2001**, 105, 8025–8030.

(7) Krimm, S.; Bandekar, J. Vibrational Spectroscopy and Conformation of Peptides, Polypeptides, and Proteins. *Adv. Protein Chem*. **1986**, 38, 181–364.

(8) Hamm, P.; Woutersen, S. Coupling of the Amide I Modes of the Glycine Dipeptide. *Bull. Chem. Soc. Jpn.* **2002**, 75, 985–988.

(9) Torii, H.; Tasumi, M. Modeling the Amide I Bands of Small Peptides. *J. Chem. Phys.* **1992**, 96, 3379–3386.

(10) Lessing, J.; Roy, S.; Reppert, M.; Baer, M.; Marx, D.; Jansen, T. L. C.; Knoester, J.; Tokmakoff, A. Identifying Residual Structure in Intrinsically Disordered Systems: A 2D IR Spectroscopic Study of the GVGXPGVG Peptide. *J. Am. Chem. Soc*. **2012**, 134, 5032–5035.

(11) Smith, A. W.; Lessing, J.; Ganim, Z.; Peng, C. S.; Tokmakoff, A.; Roy, S.; Jansen, T. L. C.; Knoester, J. Melting of β-Hairpin Peptide Using Isotope-Edited 2D IR Spectroscopy and Simulations. *J. Phys. Chem. B* **2010**, 114, 10913–10924.

(12) Chung, H. S.; Khalil, M.; Smith, A. W.; Ganim, Z.; Tokmakoff, A. Conformational Changes during the Nanosecond-to-Millisecond Unfolding of Ubiquitin. *Proc. Natl. Acad. Sci. U.S.A.* **2005**, 102, 612–617.

(13) Anfinsen, C. B. Principles That Govern the Folding of Protein Chains. *Science* **1973**, 181, 223–230.

(14) Selkoe, D. J. Cell Biology of Protein Misfolding: The Examples of Alzheimer's and Parkinson's Diseases. *Nat. Cell Biol.* **2004**, 6, 1054–1061.

(15) Jaikaran, E. T. A. S.; Clark, A. Islet Amyloid and Type 2 Diabetes: From Molecular Misfolding to Islet Pathophysiology. *Biochim. Biophys. Acta* **2001**, 1537, 179–203.

(16) Kim, P. S.; Baldwin, R. L. Specific Intermediates in the Folding Reactions of Small Proteins and the Mechanism of Protein Folding. *Ann. Rev. Biochem.* **1982**, 51, 459–489.

(17) Roder, H.; Elöve, G. A.; Englander, S. W. Structural Characterization of Folding Intermediates in Cytochrome c by H-Exchange Labelling and Proton NMR. *Nature* **1988**, 335, 700–704.

(18) Tirado-Rives, J.; Jorgensen, W. L. Molecular Dynamics Simulations of the Unfolding of an a-Helical Analogue of Ribonuclease A S-Peptide in Water. *Biochemistry* **1991**, 30, 3864–3871.

(19) Baiz, C. R.; Lin, Y. S.; Peng, C. S.; Beauchamp, K. A.; Voelz, V. A.; Pande, V. S.; Tokmakoff, A. A Molecular Interpretation of 2D IR Protein Folding Experiments with Markov State Models. *Biophys. J.* **2014**, 106, 1359–1370.

(20) Bycroft, M.; Matouschek, A.; Kellis Jr, J. T.; Serrano, L.; Fersht, A. R. Detection and Characterization of a Folding Intermediate in Barnase by NMR. *Nature* **1990**, 346, 488–490.

(21) Yang, W. Y.; Pitera, J. W.; Swope, W. C.; Gruebele, M. Heterogeneous Folding of the Trpzip Hairpin: Full Atom Simulation and Experiment. *J. Mol. Biol.* **2004**, 336, 241–251.

(22) Zhuang, W.; Cui, R. Z.; Silva, D. A.; Huang, X. Simulating the T-Jump-Triggered Unfolding Dynamics of trpzip2 Peptide and Its Time-Resolved IR and Two-Dimensional IR Signals Using the Markov State Model Approach. *J. Phys. Chem. B* **2011**, 115, 5415–5424.

(23) Hauser, K.; Krejtschi, C.; Huang, R.; Wu, L.; Keiderling, T. A. Site-Specific Relaxation Kinetics of a Tryptophan Zipper Hairpin Peptide Using Temperature-Jump IR Spectroscopy and Isotopic Labeling. J. *Am. Chem. Soc.* **2008**, 130, 2984–2992.

(24) Balbach, J. Compaction during Protein Folding Studied by Real-Time NMR Diffusion Experiments. *J. Am. Chem. Soc.* **2000**, 122, 5887–5888.

(25) Muñoz, V.; Thompson, P. A.; Hofrichter, J.; Eaton, W. A. Folding Dynamics and Mechanism of Beta-Hairpin Formation. *Nature* **1997**, 390, 196–199.

(26) Segel, D. J.; Bachmann, A.; Hofrichter, J.; Hodgson, K. O.; Doniach, S.; Kiefhaber, T. Characterization of Transient Intermediates in Lysozyme Folding with Time-Resolved Small-Angle X-Ray Scattering. *J. Mol. Biol.* **1999**, 288, 489–499.

(27) Agashe, V. R.; Shastry, M. C. R.; Udgaonkar, J. B. Initial Hydrophobic Collapse in the Folding of Barstar. *Nature* **1995**, 377, 754–757.

(28) Kühn, T.; Schwalbe, H. Monitoring the Kinetics of Ion-Dependent Protein Folding by Time-Resolved NMR Spectroscopy at Atomic Resolution. *J. Am. Chem. Soc.* **2000**, 122, 6169–6174.

(29) Ianoul, A.; Mikhonin, A.; Lednev, I. K.; Asher, S. A. UV Resonance Raman Study of the Spatial Dependence of α-Helix Unfolding. *J. Phys. Chem. A* **2002**, 106, 3621–3624.

(30) Bredenbeck, J.; Helbing, J.; Sieg, A.; Schrader, T.; Zinth, W.; Renner, C.; Behrendt, R.; Moroder, L.; Wachtveitl, J.; Hamm, P. Picosecond Conformational Transition and Equilibration of a Cyclic Peptide. *Proc. Natl. Acad. Sci. U.S.A* **2003**, 100, 6452–6457.

(31) Kubelka, J.; Hofrichter, J.; Eaton, W. A. The Protein Folding “Speed Limit.” *Curr. Opin. Struct. Biol.* **2004**, 14, 76–88.

(32) Yang, W. Y.; Gruebele, M. Detection-Dependent Kinetics as a Probe of Folding Landscape Microstructure. *J. Am. Chem. Soc.* **2004**, 126, 7758–7759.

(33) Finke, J. M.; Jennings, P. A.; Lee, J. C.; Onuchic, J. N.; Winkler, J. R. Equilibrium Unfolding of the Poly(glutamic acid)$_{20}$ Helix. *Biopolymers* **2007**, 86, 193–211.

(34) Wei, G.; Mousseau, N.; Derreumaux, P. Complex Folding Pathways in a Simple β-Hairpin. *Proteins Struct. Funct. Genet.* **2004**, 56, 464–474.

(35) Wang, L.; Skinner, J. L. Thermally Induced Protein Unfolding Probed by Isotope-Edited IR Spectroscopy. *J. Phys. Chem. B* **2012**, 116, 9627–9634.

(36) Meuzelaar, H.; Marino, K. A.; Huerta-Viga, A.; Panman, M. R.; Smeenk, L. E. J.; Kettelarij, A. J.; Van Maarseveen, J. H.; Timmerman, P.; Bolhuis, P. G.; Woutersen, S. Folding Dynamics of the Trp-Cage Miniprotein: Evidence for a Native-like Intermediate from Combined Time-Resolved Vibrational Spectroscopy and Molecular Dynamics Simulations. *J. Phys. Chem. B* **2013**, 117, 11490–11501.

(37) Beauchamp, K. A.; McGibbon, R.; Lin, Y.-S.; Pande, V. S. Simple Few-State Models Reveal Hidden Complexity in Protein Folding. *Proc. Natl. Acad. Sci. U.S.A* **2012**, 109, 17807–17813.

(38) Hartl, F. U. Molecular Chaperones in Cellular Protein Folding. *Nature* **1996**, 381, 571–580.

(39) Dobson, C. M. Protein Folding and Misfolding. *Nature* **2003**, 426, 884–890.

(40) Meuzelaar, H.; Tros, M.; Huerta-Viga, A.; Van Dijk, C. N.; Vreede, J.; Woutersen, S. Solvent-Exposed Salt Bridges Influence the Kinetics of α-Helix Folding and Unfolding. *J. Phys. Chem. Lett.* **2014**, 5, 900–904.

(41) Robson, B.; Pain, R. H. Analysis of the Code Relating Sequence to Conformation in Proteins: Possible Implications for the Mechanism of Formation of Helical Regions. *J. Mol. Biol.* **1971**, 58, 237–257.

(42) Woutersen, S.; Pfister, R.; Hamm, P.; Mu, Y.; Kosov, D. S.; Stock, G. Peptide Conformational Heterogeneity Revealed from Nonlinear Vibrational Spectroscopy and Molecular-Dynamics Simulations. *J. Chem. Phys.* **2002**, 117, 6833–6840.

(43) Zanni, M. T.; Asplund, M. C.; Hochstrasser, R. M. Two-Dimensional Heterodyned and Stimulated Infrared Photon Echoes of N-Methylacetamide-D. *J. Chem. Phys.* **2001**, 114, 4579–4590.

(44) Hamm, P.; Lim, M.; Hochstrasser, R. M. Structure of the Amide I Band of Peptides Measured by Femtosecond Nonlinear-Infrared Spectroscopy. *J. Phys. Chem. B* **1998**, 102, 6123–6138.

(45) Woutersen, S.; Mu, Y.; Stock, G.; Hamm, P. Hydrogen-Bond Lifetime Measured by Time-Resolved 2D-IR Spectroscopy: N-Methylacetamide in Methanol. *Chem. Phys.* **2001**, 266, 137–147.

(46) Noda, I.; Liu, Y.; Ozaki, Y. Two-Dimensional Correlation Spectroscopy Study of Temperature-Dependent Spectral Variations of N-Methylacetamide in the Pure Liquid State. 2. Two-Dimensional Infrared Analysis. *J. Phys. Chem.* **1996**, 100, 8674–8680.

(47) Kwac, K.; Cho, M. Molecular Dynamics Simulation Study of N-Methylacetamide in Water. II. Two-Dimensional Infrared Pump-Probe Spectra. *J. Chem. Phys*. **2003**, 119, 2256–2263.

(48) DeCamp, M. F.; DeFlores, L.; McCracken, J. M.; Tokmakoff, A.; Kwac, K.; Cho, M. Amide I Vibrational Dynamics of N-Methylacetamide in Polar Solvents: The Role of Electrostatic Interactions. *J. Phys. Chem. B* **2005**, 109, 11016–11026.

(49) Jansen, T. L. C.; Knoester, J. Nonadiabatic Effects in the Two-Dimensional Infrared Spectra of Peptides: Application to Alanine Dipeptide. *J. Phys. Chem. B* **2006**, 110, 22910–22916.

(50) Arunan, E.; Desiraju, G. R.; Klein, R. A.; Sadlej, J.; Scheiner, S.; Alkorta, I.; Clary, D. C.; Crabtree, R. H.; Dannenberg, J. J.; Hobza, P.; et al. Definition of the Hydrogen Bond. *Pure Appl. Chem.* **2011**, 83, 1637–1641.

(51) Chen, X. G.; Schweitzer-Stenner, R.; Krimm, S.; Mirkin, N. G.; Asher, S. A. N-Methylacetamide and Its Hydrogen-Bonded Water Molecules Are Vibrationally Coupled. *J. Am. Chem. Soc.* **1994**, 116, 11141–11142.

(52) DeFlores, L. P.; Ganim, Z.; Ackley, S. F.; Chung, H. S.; Tokmakoff, A. The Anharmonic Vibrational Potential and Relaxation Pathways of the Amide I and II Modes of N-Methylacetamide. *J. Phys. Chem. B* **2006**, 110, 18973–18980.

(53) Jansen, T. L. C.; Knoester, J. A Transferable Electrostatic Map for Solvation Effects on Amide I Vibrations and Its Application to Linear and Two-Dimensional Spectroscopy. *J. Chem. Phys.* **2006**, 124, 044502.

(54) Jansen, T. L. C. Linear Absorption and Two-Dimensional Infrared Spectra of N-Methylacetamide in Chloroform Revisited: Polarizability and Multipole Effect. *J. Phys. Chem. B* **2014**, 118, 8162–8169.

(55) Jansen, T. L. C.; Dijkstra, A. G.; Watson, T. M.; Hirst, J. D.; Knoester, J. Modeling the Amide I Bands of Small Peptides. *J. Chem. Phys.* **2006**, 125, 044312.

(56) Bandekar, J. Amide Modes and Protein Conformation. *Biochim. Biophys. Acta.* **1992**, 1120, 123–143.

(57) Schmidt, J. R.; Corcelli, S. A.; Skinner, J. L. Ultrafast Vibrational Spectroscopy of Water and Aqueous N-Methylacetamide: Comparison of Different Electronic Structure/molecular Dynamics Approaches. *J. Chem. Phys.* **2004**, 121, 8887–8896.

(58) Roseman, M. A. Hydrophobicity of the Peptide C=O...H-N Hydrogen-Bonded Group. *J. Mol. Biol.* **1988**, 201, 621–623.

(59) Fujisaki, H.; Yagi, K.; Straub, J. E.; Stock, G. Quantum and Classical Vibrational Relaxation Dynamics of N-Methylacetamide on Ab Initio Potential Energy Surfaces. *Int. J. Quantum Chem.* **2009**, 109, 2047–2057.

(60) Kwac, K.; Cho, M. Molecular Dynamics Simulation Study of N-Methylacetamide in Water. I. Amide I Mode Frequency Fluctuation. *J. Chem. Phys.* **2003**, 119, 2247–2255.

(61) Fujisaki, H.; Yagi, K.; Hirao, K.; Straub, J. E. Quantum Dynamics of a Peptide-like Molecule Studied by Vibrational Configuration Interaction Method. *Chem. Phys. Lett.* **2007**, 443, 6–11.

(62) Bastida, A.; Soler, M. A.; Zúñiga, J.; Requena, A.; Kalstein, A.; Fernández-Alberti, S. Hybrid Quantum/Classical Simulations of the Vibrational Relaxation of the Amide I Mode of N-Methylacetamide in D2O Solution. *J. Phys. Chem. B* **2012**, 116, 2969–2980.

(63) Farag, M. H.; Bastida, A.; Ruiz-López, M. F.; Monard, G.; Ingrosso, F. Vibrational Energy Relaxation of the Amide I Mode of N-Methylacetamide in D2O Studied through Born-Oppenheimer Molecular Dynamics. *J. Phys. Chem. B* **2014**, 118, 6186–6197.

(64) Bloem, R.; Dijkstra, A. G.; Jansen, T. L. C.; Knoester, J. Simulation of Vibrational Energy Transfer in Two-Dimensional Infrared Spectroscopy of Amide I and Amide II Mode in Solution. *J. Chem. Phys.* **2008**, 129, 055101.

(65) Dijkstra, A. G.; Jansen, T. L. C.; Bloem, R.; Knoester, J. Simulation of Vibrational Energy Transfer in Two-Dimensional Infrared Spectroscopy of Amide I and Amide II Mode in Solution. *J. Chem. Phys.* **2007**, 127, 194505.

(66) Turton, D. A.; Wynne, K. Structural Relaxation in the Hydrogen-Bonding Liquids N-Methylacetamide and Water Studied by Optical Kerr Effect Spectroscopy. *J. Chem. Phys.* **2008**, 128, 154516.

(67) Cunha, A. V; Salamatova, E.; Bloem, R.; Roeters, S. J.; Woutersen, S.; Pshenichnikov, M. S.; Jansen, T. L. C. Interplay between Hydrogen Bonding and Vibrational Coupling in Liquid N-Methylacetamide. *J. Phys. Chem. Lett.* **2017**, 8, 2438–2444.

(68) Kumar, R.; Schmidt, J. R.; Skinner, J. L. Hydrogen Bonding Definitions and Dynamics in Liquid Water. *J. Chem. Phys.* **2007**, 126, 204107.

(69) Luzar, A.; Chandler, D. Hydrogen-Bond Kinetics in Liquid Water. Nature 1996, 379, 55–57.

(70) Torres, J.; Briggs, J. A. G.; Arkin, I. T. Multiple Site-Specific Infrared Dichroism of CD3-Z, a Transmembrane Helix Bundle. *J. Mol. Biol.* **2002**, 316, 365–374.

(71) Woutersen, S.; Mu, Y.; Stock, G.; Hamm, P. Subpicosecond Conformational Dynamics of Small Peptides Probed by Two-Dimensional Vibrational Spectroscopy. *Proc. Natl. Acad. Sci. U.S.A.* **2001**, 98, 11254–11258.

(72) Pshenichnikov, M. S.; Yeremenko, S.; Wiersma, D. A. IR Photon-Echo Spectroscopy of Water: The Thermalization Effects. *Ultrafast Phenom.* XIV 2005, 404–406.

(73) Cringus, D.; Bakulin, A.; Lindner, J.; Vöhringer, P.; Pshenichnikov, M. S.; Wiersma, D. A. Ultrafast Energy Transfer in Water - AOT Reverse Micelles. *J. Phys. Chem. B* **2007**, 111, 14193–14207.

(74) Kwak, K.; Park, S.; Finkelstein, I. J.; Fayer, M. D. Frequency-Frequency Correlation Functions and Apodization in Two-Dimensional Infrared Vibrational Echo Spectroscopy: A New Approach. *J. Chem. Phys.* **2007**, 127, 124503.

(75) Kwak, K.; Rosenfeld, D. E.; Fayer, M. D. Taking Apart the Two-Dimensional Infrared Vibrational Echo Spectra: More Information and Elimination of Distortions. *J. Chem. Phys.* **2008**, 128, 204505.

(76) Woys, A. M.; Almeida, A. M.; Wang, L.; Chiu, C. C.; McGovern, M.; De Pablo, J. J.; Skinner, J. L.; Gellman, S. H.; Zanni, M. T. Parallel β-Sheet Vibrational Couplings Revealed by 2D IR Spectroscopy of an Isotopically Labeled Macrocycle: Quantitative Benchmark for the Interpretation of Amyloid and Protein Infrared Spectra. *J. Am. Chem. Soc.* **2012**, 134, 19118–19128.

(77) Cunha, A. V.; Bondarenko, A. S.; Jansen, T. L. C. Assessing Spectral Simulation Protocols for the Amide I Band of Proteins. *J. Chem. Theory Comput.* **2016**, 12, 3982–3992.

(78) Berendsen, H. J. C.; Grigera, J. R.; Straatsma, T. P. The Missing Term in Effective Pair Potentials. *J.Phys. Chem.* **1987**, 91, 6269–6271.

(79) Bakulin, A. A.; Cringus, D.; Pieniazek, P. A.; Skinner, J. L.; Jansen, T. L. C.; Pshenichnikov, M. S. Dynamics of Water Confined in Reversed Micelles: Multidimensional Vibrational Spectroscopy Study. J. *Phys. Chem. B* **2013**, 117, 15545–15558.

(80) Bakulin, A. A.; Liang, C.; Jansen, T. L. C.; Wiersma, D. A.; Bakker, H. J.; Pshenichnikov, M. S. Hydrophobic Solvation: A 2D IR Spectroscopic *Inquest. Acc. Chem. Res.* **2009**, 42, 1229–1238.

(81) Jansen, T. L. C.; Auer, B. M.; Yang, M.; Skinner, J. L. Two-Dimensional Infrared Spectroscopy and Ultrafast Anisotropy Decay of Water. *J. Chem. Phys.* **2010**, 132, 224503.

(82) Groot, C. C. M.; Meister, K.; DeVries, A. L.; Bakker, H. J. Dynamics of the Hydration Water of Antifreeze Glycoproteins. *J. Phys. Chem. Lett.* **2016**, 7, 4836–4840.

(83) Fogarty, A. C.; Laage, D. Water Dynamics in Protein Hydration Shells: The Molecular Origins of the Dynamical Perturbation. *J. Phys. Chem. B* **2014**, 118, 7715–7729.

(84) Daley, K. R.; Kubarych, K. J. An “iceberg” Coating Preserves Bulk Hydration Dynamics in Aqueous PEG Solutions. *J. Phys. Chem. B* **2017**, 121, 10574–10582.

(85) Yang, J.; Wang, Y.; Wang, L.; Zhong, D. Mapping Hydration Dynamics around a β-Barrel Protein. *J. Am. Chem. Soc.* **2017**, 139, 4399–4408.

(86) Tros, M.; Zheng, L.; Hunger, J.; Bonn, M.; Bonn, D.; Smits, G. J.; Woutersen, S. Picosecond Orientational Dynamics of Water in Living Cells. *Nat. Commun.* **2017**, 8, 904.

(87) Thouless, D. J. Electrons in Disordered Systems and the Theory of Localization. *Phys. Rep.* **1974**, 13, 93–142.

(88) Wynne, K. The Mayonnaise Effect. *J. Phys. Chem. Lett.* **2017**, 8, 6189–6192.

(89) Chuntonov, L.; Kumar, R.; Kuroda, D. G. Non-Linear Infrared Spectroscopy of the Water Bending Mode: Direct Experimental Evidence of Hydration Shell Reorganization? *Phys. Chem. Chem. Phys.* **2014**, 16, 13172–13181.

(90) Chang, R. *Chemistry*; McGraw-Hill Companies: New York, 2009.

(91) Helbing, J.; Hamm, P. Compact Implementation of Fourier Transform Two-Dimensional IR Spectroscopy without Phase Ambiguity. *J. Opt. Soc. Am. B* **2011**, 28, 171–178.

(92) Bloem, R.; Garrett-Roe, S.; Strzalka, H.; Hamm, P.; Donaldson, P. Enhancing Signal Detection and Completely Eliminating Scattering Using Quasi-Phase-Cycling in 2D IR Experiments. *Opt. Express* **2010**, 18, 27067–27078.

(93) Backus, E. H. G.; Garrett-Roe, S.; Hamm, P. Phasing Problem of Heterodyne-Detected Two-Dimensional Infrared Spectroscopy. *Opt. Lett.* **2008**, 33, 2665–2667.

(94) Van Der Spoel, D.; Lindahl, E.; Hess, B.; Groenhof, G.; Mark, A. E.; Berendsen, H. J. C. GROMACS: Fast, Flexible, and Free. *J. Comput. Chem.* **2005**, 26, 1701–1718.

(95) Jorgensen, W. L.; Maxwell, D. S.; Tirado-Rives, J. Development and Testing of the OLPS All-Atom Force Field on Conformational Energetics and Properties of Organic Liquids. *J. Am. Chem. Soc.* 1996, **118**, 11225–11236.

(96) Swope, W. C.; Andersen, H. C.; Berens, P. H.; Wilson, K. R. A Computer Simulation Method for the Calculation of Equilibrium Constants for the Formation of Physical Clusters of Molecules: Application to Small Water Clusters. *J. Chem. Phys.* **1982**, 76, 637–649.

(97) Tobias, D. J.; Brooks III, C. L.; Fleischman, S. H. Conformational Flexibility in Free Energy Simulations. *Chem. Phys. Lett.* **1989**, 156, 256–260.

(98) Caleman, C.; Van Maaren, P. J.; Hong, M.; Hub, J. S.; Costa, L. T.; Van Der Spoel, D. Force Field Benchmark of Organic Liquids: Density, Enthalpy of Vaporization, Heat Capacities, Surface Tension, Isothermal Compressibility, Volumetric Expansion Coefficient, and Dielectric Constant. *J. Chem. Theory Comput.* **2012**, 8, 61–74.

(99) Hess, B.; Bekker, H.; Berendsen, H. J. C.; Fraaije, J. G. E. M. LINCS: A Linear Constraint Solver for Molecular Simulations. *J. Comput. Chem.* **1997**, 18, 1463–1472.

(100) Liang, C.; Jansen, T. L. C. An Efficient N 3-Scaling Propagation Scheme for Simulating Two-Dimensional Infrared and Visible Spectra. *J. Chem. Theory Comput.* **2012**, 8, 1706–1713.

Chapter 4

Hydrogen Bond and Lifetime Dynamics in Diluted Alcohols

Hydrogen-bonding plays a crucial role in many chemical and biochemical reactions. Alcohols, with their hydrophilic and hydrophobic groups, constitute an important class of hydrogen-bonding molecules with functional tuning possibilities through changes in the hydrophobic tails. Recent studies demonstrated that for solutions of alcohols changes in the hydrophobic tail significantly affect a broad range of dynamics properties of the liquid. Still, the understanding is lacking on the origin of such differences in terms of a solvent- versus a solute-dominated effect. Here we reveal this origin by studying hydrogen-bond dynamics in a number of alcohol molecules – from methanol to butanol – diluted in a hydrogen-bond accepting environment, acetonitrile. The dynamics were investigated by pump-probe and 2D infrared spectroscopy combined with molecular dynamics-spectral simulations, using the OH stretching mode as a reporter. For all considered alcohols, the vibrational lifetime of the OH stretching mode was found as ~3 ps. The hydrogen-bond dynamics exhibit similar behavior with a fast (~200 fs) initial relaxation dominated by librational motion and a slow (~4 ps) relaxation due to hydrogen-bond exchange dynamics. The similar dynamics over such a broad range of alcohols led us to conclude that the previously observed differences in dynamics in bulk alcohols originate from the dependence of the solvent properties on the hydrophobic tail, while the solute properties as found herein are essentially independent of the hydrophobic tail.

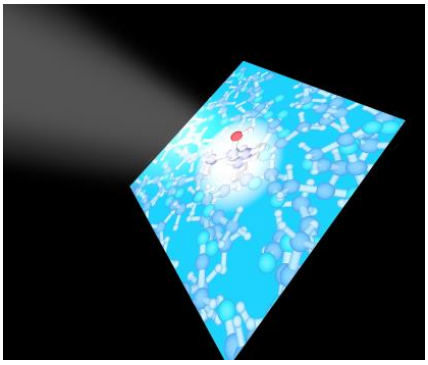

The current chapter is based on the following publication:

Evgeniia Salamatova, Ana V. Cunha, Keisuke Shinokita, Thomas L. C. Jansen, and Maxim S.Pshenichnikov, *Phys. Chem. Chem. Phys*.,2017, 19, 27960-27967.

4.1 Introduction

Hydrogen bonding[1] (HB) is one of the fundamental interactions in chemistry, biology and material sciences, and as such has been extensively studied.[2,3] Ultrafast two-dimensional (2D) IR spectroscopy[4,5] has been proven to be a powerful tool for revealing HB dynamics in water, liquid[6,7] and interfacial[8,9] alike. Alcohols present another example of a HB liquids, where the molecules form HBs via the hydroxyl group[10–11] that is attached to a hydrophobic alkyl tail.

So far, most of the studies on alcohols have been devoted to alcohol clusters in a non-polar solvent such as CCl_4[14–20]. The primary alcohols as methanol and ethanol were in a particular focus[12,15,16,18–28] due to their simple structure. Woutersen *et al.*[20] demonstrated dependence of OH-stretching mode lifetime on the excitation frequency in ethanol clusters in CCl_4 with the timescales ranging from 250 to 900 fs. The HB recombination time was found to vary with the size of alkyl chain group, from ~9 ps in methanol to ~15 ps in ethanol. Later, Laenen *et al.*[18] reported a similar trend for methanol clusters. Gaffney *et al.*[29] implemented another approach, where concentration of methanol-*d* diluted in CCl_4 was varied, and reported the relaxation dynamics of the methanol-*d* clusters as ~500 fs for all molar ratios with a conclusion that the HB dynamics hardly change with changing alcohol concentration.

Similarly to alcohol clusters, recent experimental and theoretical studies on bulk alcohols showed the effect of the size of alkyl-chain group on hydroxyl stretching dynamics[30–32]. Mazur *et al.*[31] explored such dynamics in bulk deuterated alcohols by monitoring vibrational and rotational dynamics of the OD stretching mode. The lifetime of the excited OD stretch was found in the sub-ps region and dependent on the alkyl chain size (0.75 ps for methanol and 0.9 ps for ethanol, 1-propanol and 1-butanol). In contrast to the lifetime, the structural relaxation time exhibited strong correlation with the size of alcohol molecule, i.e. larger alkyl chain group led to slower dynamics: ~5 ps for methanol, ~8 ps for ethanol, ~10.5 ps for 1-propanol, and ~11 ps for 1-butanol. Furthermore, the rotational dynamics possessed similar correlation with the size of alcohol molecule, i.e. the increase of alkyl chain led to slower dynamics.

Shinokita et al.[30] explored the OH stretch dynamics of methanol, ethanol and 2-propanol molecules diluted in respective deuterated solutions to avoid intermolecular vibrational couplings. It was found that the lifetime of the OH-stretching mode exhibits strong dependence on the size of alkyl chain (630 fs, 720 fs and 990 fs for methanol, ethanol and 2-propanol, respectively). OH-stretch dynamics occurred at two prime time scales: fast (~150 fs) and long (>4 ps), with

both components slowing down with the increase of the molecule size. The rotational dynamics of the OH group, obtained by Shinokita et al.[30] with ultrafast IR spectroscopy and Ludwig et al.[33] with NMR also possessed the dependence on the size: the larger the molecule, the slower the rotational dynamics. The timescales of the HB exchange dynamics, obtained experimentally, showed an increase from 5 ps for methanol[30,31,33] to ~90 ps in 1-hexanol[33].

All the aforementioned studies came to the unanimous conclusion: increasing the size of the alkyl chain leads to slowing the hydroxyl stretching mode as well as HB dynamics. The dynamics, however, depends on both inter- and intra- molecular interactions. This leaves the question open which one is dominant in the observed time scales.

Here we address this issue by eliminating differences in the interaction of the excited OH-stretch and the bulk solvent by studying alcohols diluted in acetonitrile, where intermolecular interactions between the alcohol molecules are negligibly weak. A series of primary alcohol molecules (methanol, ethanol, two isomers of propanol, and four isomers of butanol) were studied by linear, pump-probe and 2D IR spectroscopy, with the OH-stretching mode (~3535 cm^{-1}) acting as a reporter for HB dynamics. We show that the lifetime of the OH-stretching mode (~3 ps) and two timescales of HB dynamics (~200 fs and ~4 ps) are similar in all alcohols in sharp contrast to the observations in bulk alcohols. The latter finding is also confirmed by theoretical work, which uses response function based calculations to predict the linear and 2D IR spectra. The obtained results strongly suggest that in diluted alcohols the alkyl groups play a minor role in solvation and therefore the differences in the vibrational lifetimes and solvation dynamics in the bulk alcohols originates from the intermolecular interactions.

4.2 Results and Discussion

4.2.1 Linear absorption

Absorption spectra of methanol, 1-butanol and tert-butanol dissolved in MeCN in the region of the OH-stretching mode are shown in Figure 4.1, together with their simulated counterparts (for the spectra of other alcohols, see SI, Figure S4.3). The absorption peak of the OH stretch situated near ~3535 cm^{-1}, slightly red-shifts and becomes ~10% narrower as the alcohol size increases (see SI, Figure S4.4). The simulated spectra are wider than the experimental ones (especially for tert-butanol) and do not possess any size-dependence which is attributed to the fact that classical force fields are not fully optimized for this type of modelling.

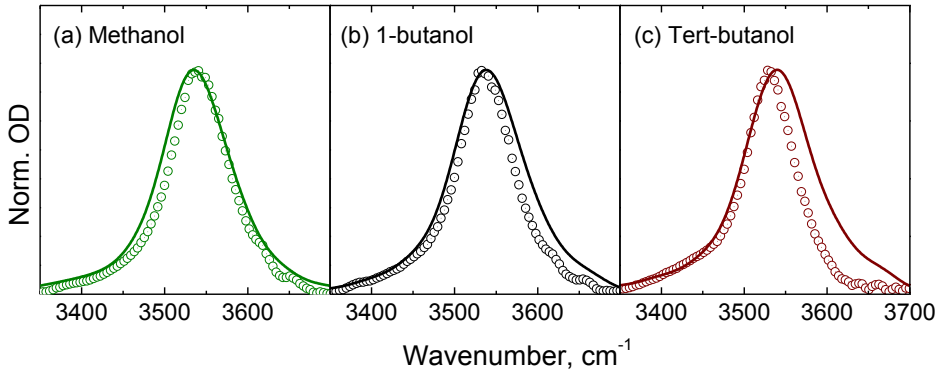

Figure 4.1 Experimental (dots) and simulated (solid lines) linear absorption spectra of (a) methanol, (b) 1-butanol and (c) tert-butanol dissolved in MeCN. The simulated spectra are blue-shifted by 50 cm-1 for ease of comparison.

4.2.2 Pump-probe

The pump-probe transients are shown in Figure 4.2 (for the pump-probe transients and the transient spectra of all alcohols, see SI, Figures S4.5 and S4.6, respectively) at the frequency of maximum bleaching (3535 cm^{-1}) and induced absorption (3370 cm^{-1}). After initial relaxation at the ps time scale, the transients level off which is attributed to population relaxation to the hot ground state[6]. To account for this effect, the transients were fit with the three-state kinetic model (see SI, Figure S4.7); the temperature jump was estimated as ~0.5 K (see SI, Figure S4.8).

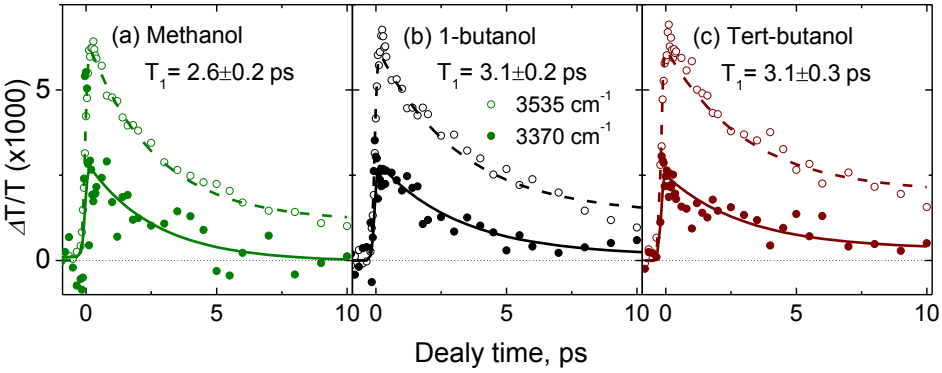

Figure 4.2 Experimental transients (symbols) at bleaching/stimulated emission (3535 cm^{-1}, open circles) and induced absorption (3370 cm^{-1}, filled circles, the sign is inverted) regions for (a) methanol, (b) 1-butanol, (c) tert-butanol, diluted in MeCN. The fits obtained from a kinetic model (SI,Figure S4.7) are shown by the lines with the corresponding lifetimes T_1 indicated.

Lifetimes T_1 of the OH stretch for all alcohols are about 3 ps (Figure 4.3) with a weak trend to increase with the increase of the molecule size. The obtained results

are in good agreement with the lifetime of the hydrogen bonded OH-stretching mode previously reported as 3.5±0.4 ps[34]. Nonetheless, the trend obtained also suggests partial energy relaxation via intramolecular channels, to be consistent with the finite lifetime of 7.5±0.5 ps of free OH-stretch vibrations[34].

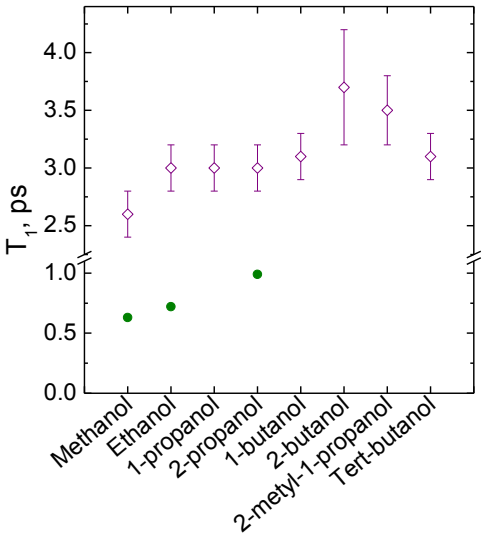

Figure 4.3 Lifetime of the OH-stretching mode T_1, calculated from the three-state kinetic model (SI Figure S4.7) for all studied alcohol/MeCN samples (open violet diamonds) in comparison to the bulk alcohol lifetimes (filled olive circles; the data are taken from Ref.[30]).

In contrast with diluted alcohol molecules, the lifetimes of hydroxyl stretching mode in bulk alcohols are shorter than 1 ps[30,31]. Furthermore, the lifetimes of bulk alcohols show a prominent increase (by a factor of ~2) from methanol to 2-propanol[30]. These are clear signatures of the fact that in bulk alcohols the OH stretch vibrational relaxation is mediated by collective intermolecular rather than intramolecular modes.

4.2.3 2D-IR spectra

Figure 4.4 shows 2D-IR spectra of methanol, 1-butanol and tert-butanol solutions at waiting times of T=0.1 ps and T=1 ps (see SI, Figure S4.9 for the complete set of 2D-IR spectra). At short waiting times, the 2D spectra are diagonally elongated which corresponds to high correlation between excitation and probe frequencies. By T=1 ps, the diagonal elongation decreases virtually to zero which signifies complete loss of the phase memory. Although the simulated 2D spectra (bottom panel) are slightly broader (see Figure 4.1 and discussion therein), they nonetheless show a reasonable agreement with the experimental ones.

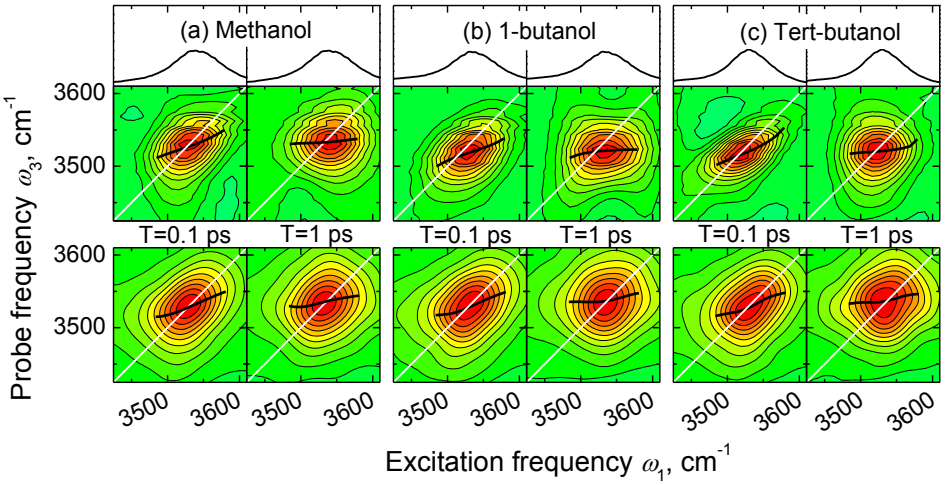

Figure 4.4 Experimental absorption spectra (top panels), experimental (middle panels) and simulated (bottom panels) 2D-IR spectra in the OH-stretching mode region for MeCN solution of (a) methanol, (b) 1-butanol and (c) tert-butanol at *T*=0.1 ps and *T*=1 ps. The 2D spectra are normalized to the maximal amplitude; only the bleaching region is shown. The equidistant contours are drawn with a 10% step of the maximal amplitude. The results of the CLS analysis are depicted by black lines. The simulated spectra are blue-shifted by 50 cm^{-1} along both axes for ease of comparison.

To extract quantitative information on the frequency-frequency correlation function[35] we applied the center line slope (CLS) analysis[36] in the frequency range of 3485-3580 cm^{-1} (Figure 4.4, black lines). The center lines are not perfectly straight as was also previously reported for other hydrogen bonding systems[37–40]. This is interpreted as a frequency-dependent correlation function, i.e., in other words, the dynamics are non-Gaussian.[39] Without performing any further analysis (which requires a low noise level) we note that the dynamics on the red side of the spectra are generally faster than that on the blue side in accordance with previous observations for the OH-stretch mode. The averaged slope values for the systems with non-Gaussian dynamics have larger error bars[39], which we accounted for in our analysis.

The dependences of CLS values on the waiting time *T* are summarized in Figure 4.5 (for all CLS data, see SI Figures S4.10 and S4.11). The dynamics are essentially identical for all alcohols: the fast (~200-300 fs, share of ~80%) decay in the beginning followed by an ~4 ps tail identical for all alcohols (within the error bars). The relatively large uncertainties in the slow dynamics originate from the following. First, their share in the correlation function is low (~20%); second, the lifetime of the OH stretch is shorter as compared to the timescale of slow dynamics (which provides a narrow observation window), and finally, the temperature response begins to rise at a similar timescale. The obtained dynamics have a

reasonable match with the previously reported values for MeCN bath, using a chromophore[41] (150 fs and ~3 ps, respectively), water[40] and HDO[42] (150-200 fs and 2 ps, respectively) as the solutes. The obtained results on CLS analysis are again in a sharp contrast with those for the bulk alcohols[30], where both fast and long components were slowing down with an increase in the size of the alcohol molecule. This provides another hint that the diluted alcohol dynamics are governed by the bath rather than by a particular alcohol molecule.

In the theoretical calculations, the fast component of the CLS functions is underrepresented (Figure 4.5, filled symbols), most probably because of underestimation of the time scale of the librational contribution to the frequency fluctuations. This originates either from inaccuracies in the interaction between the MeCN and the hydroxyl groups in the applied force field combination or from the fact that the water mapping was employed to model alcohols.

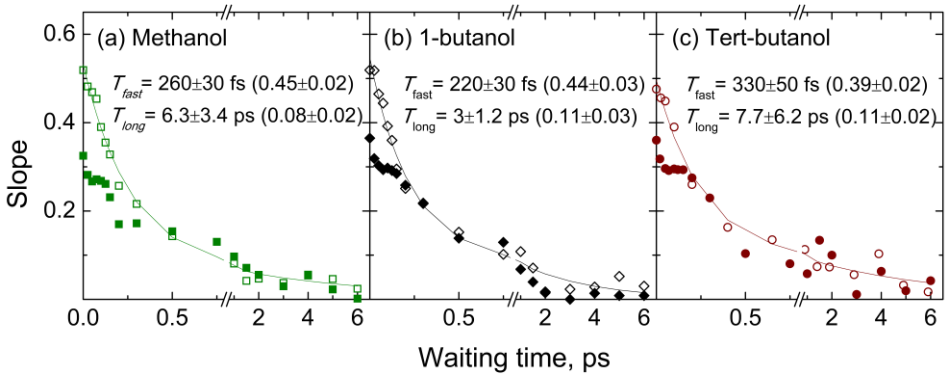

Figure 4.5 Comparison of CLS analysis, obtained from experimental (open symbols) and simulated (filled symbols) for (a) methanol, (b) 1-butanol and (c) tert-butanol. The results of biexponential fits to the experimental data are shown by the solid lines, with the parameters indicated in the legends.

4.2.4 Discussion

The frequency-frequency correlation functions derived from MD simulations are shown in Figure 4.6. They are similar for all alcohols (the strongly damped short-time oscillations notwithstanding): the fast component (~50 fs) originates from OH libations (Figure 4.7) while the slow component (~1 ps) is due to spectral diffusion as the result of rearrangement of HBs: breaking and forming new ones (Figure 4.7). The experimental CLS values are slower, most probably due to the fact that the MD simulations underestimate damping of the OH librations. The simulated frequency-frequency correlation functions are also very similar to those previously reported for water in MeCN[47]. The tail observed for water is slower, which may be caused by stronger HB and slower HB exchanges; however, this

conclusion should be taken with caution as the water simulations were performed with a different force field.

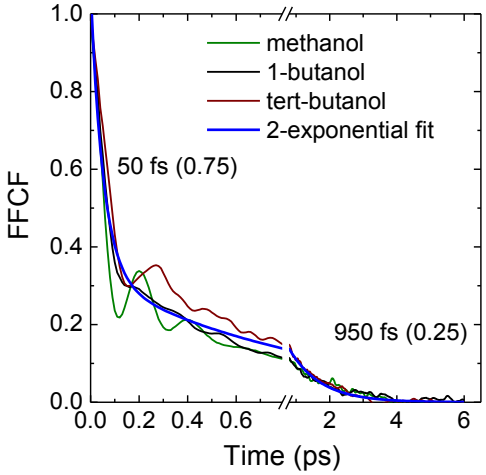

Figure 4.6 Normalized frequency-frequency correlation functions for the three simulated alcohols. The share of each exponent is indicated in the parentheses.

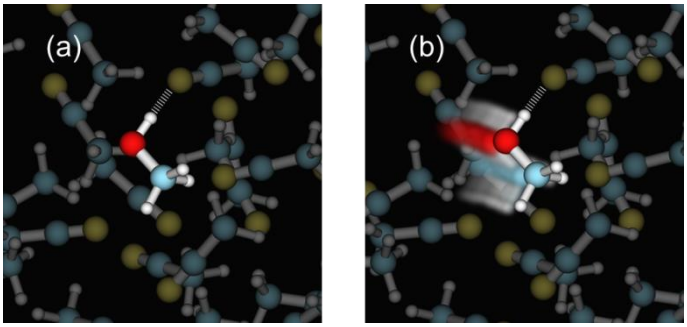

Figure 4.7 Illustration of (a) OH-librations and (b) spectral diffusion of a methanol molecule dissolved in MeCN adapted from MD simulations. A blur represents the previous positions of the OH- stretching mode (a) and the prior positions of the methanol atoms (b). The final HBs between alcohols and MeCN are depicted by dashed white line.

To understand the vanishing difference between the dynamics of the different alcohols dissolved in MeCN, we analyzed the HB between the alcohols and the nitrogen atoms of the MeCN molecules. Using a standard HB criterion[43], we found an average of 0.827, 0.802, and 0.806 of such HBs formed for methanol, 1-butanol, and tert-butanol, respectively, which already suggests very similar HB environments. In Figure 4.8, distributions of the HB distances are shown for solutions of the different alcohols; they again suggest analogous HB patterns. We further analyzed the HB lifetime dynamics as the duration between HB exchanges (Figure 4.9). Because the definition of HB is somewhat arbitrary, briefly broken

bonds may result in artificially short HB lifetimes; nevertheless, the HB dynamics are essentially identical.

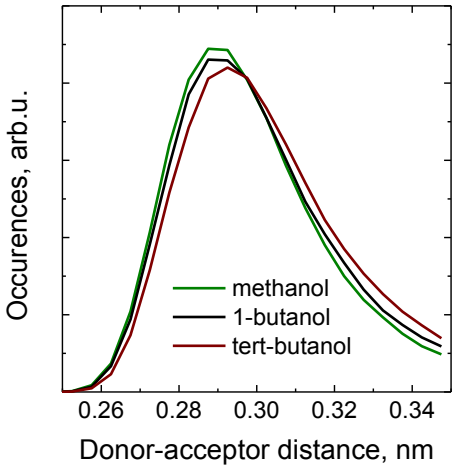

Figure 4.8 The HB (i.e. O-N) distance distribution obtained from MD simulations.

A unified picture emerges that the experimentally observed dynamics of the alcohols depend predominantly on HB dynamics of the OH group, and these HB dynamics are determined by the interaction of the OH group and the MeCN bath molecules. The hydrophobic tails affect the dynamics very little making the interaction of the OH group with the bath molecules and the nature of bath molecules the dominant factors. Despite the fact that the increase of the hydrophobic tail increases the moment of inertia and might therefore affect rotational relaxation, it appears to be a minor effect for the studied properties.

For bulk alcohols it was suggested[28] that different types of dynamics largely scale with the self-diffusion constant of the bath molecules. We found the diffusion constant of bulk MeCN to be $4.92 \cdot 10^{-5}$ cm^2/s, which is almost twice as fast as the $2.57 \cdot 10^{-5}$ cm^2/s reported for bulk methanol[30]. This suggests that the slow components of the observed dynamics of the alcohols in MeCN should be faster than for any bulk alcohol. For the CLSs, the predicted slowest timescale for a bath with diffusion constant $4.92 \cdot 10^{-5}$ cm^2/s (i.e. the MeCN bath) is about 2.3 ps, which in qualitative agreement with the slowest timescale observed herein for the CLSs, and the slowest timescale found from the frequency-frequency correlation function decay. The qualitative agreement is, thus, consistent with the conclusion that the slow dynamics are essentially driven by the solvent diffusion. However, caution must be taken as the diffusion constants and HB dynamics are quite sensitive to the particular force field choice and MeCN and alcohols are molecules with different functional groups (CN *vs*. OH).

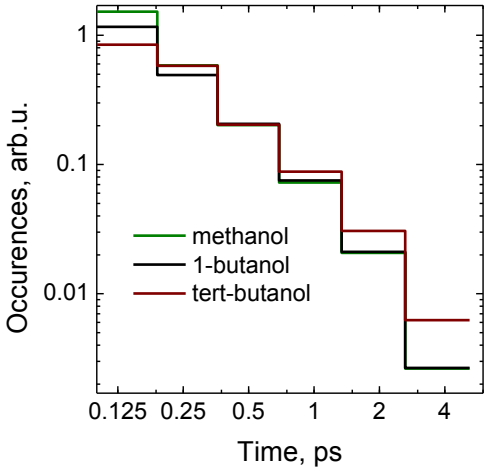

Figure 4.9 Histograms of the number of HB exchange events with a given time per alcohol molecule per picosecond for the three simulated alcohols according to the HB criterion of Ref.[43]

4.3 Conclusions

In this Chapter, we have studied dynamics and lifetimes of the OH-stretching mode of diluted alcohol molecules in the polar HB-accepting solvent, acetonitrile. Previous studies of bulk alcohols showed a large variation in the involved time scales depending on the size of the alkyl chain. This difference could originate from either inter- or intra-molecular interactions. In the present study, the intermolecular interactions between the alcohol molecules are eliminated by dilution; therefore, the obtained dynamics have solely *intra*molecular origin.

The lifetime of OH-stretching mode, used as a reporter for HB dynamics in our study, was found as ~3 ps for all eight studied alcohols. In a sharp contrast to bulk alcohols, there is no dependence on the size of alcohol molecules. From this we conclude that the intermolecular interactions must be the main reason for the observed differences in the bulk alcohols. The intramolecular vibrational relaxation must thus predominantly be directed to modes involving only the carbon and hydrogen atoms adjacent to the hydroxyl group under the test.

The OH stretch dynamics, deduced from the CLS analysis of the 2D IR spectra revealed the following two timescales: a fast librational one (~200-300 fs) and a slow one (~4 ps) related to the HB dynamics. The slow timescale was again essentially independent on the alkyl chain of the involved alcohol molecule in sharp contrast to the previous observations in bulk alcohol. This matches well with the supposition[30] that the HB exchange is correlated with the diffusion of the HB partners.

The present findings underline the importance of the solvent on the vibrational dynamics of HB groups such as the hydroxyl group of alcohols. It further demonstrates that using an alcohol with different alkyl chain as a probe of dynamics does not significantly change the outcome. This may prove true for other amphiphilic probes as well, thereby providing previously unforeseen flexibility for future studies of hydrophobic hydration.

4.4 Methods

4.4.1 Experimental

Eight alcohol molecules (methanol, ethanol, 1-propanol, 2-propanol, 1-butanol, 2-butanol, 2-methyl-1-propanol, and tert-butanol) and acetonitrile (MeCN) were obtained from Sigma-Aldrich and used without any further purification. Acetonitrile was used as a solvent due to its HB properties[44] and low absorption in the region of OH-stretch frequency. Alcohol molecules were dissolved in MeCN at pre-calculated molar ratios. The linear absorption spectra were recorded by an FTIR-spectrometer Brucker IFS 88 at room temperature (295±5 K), with 4 cm^{-1} spectral resolution in a 100 µm thickness CaF_2 cuvette. Due to hygroscopic properties of the chemicals used, all measurements were performed within one day of preparation.

The molar ratio between alcohol and MeCN was varied from 0.01 to 0.09 to determine the molar ratio where the alcohol molecules do not cluster (see SI, Figures S4.1 and S4.2). For further experiments, solutions with the molar ratio of 0.03 were used as a compromise between alcohol molecules clustering and the signal-to-noise ratio.

The IR pulses at the central wavelength of 3540 cm^{-1} and 75 fs in duration were generated by a home-built optical parametric amplification (OPA)[45]. For the 2D IR measurements, a pump-probe geometry was used[46] for which the OPA output was split into two collinear pump pulses (~3 µJ/pulse) and a probe pulse (~3 µJ/pulse). The polarization between the two pump pulses and the probe pulse was set at a magic angle of ~54.7°. The prepared solutions were pumped through a 50 µm thick sapphire nozzle to create a free-standing jet. To minimize water vapor adsorption from the air, the circulatory pump system and 2D-IR setup was constantly purged with dry nitrogen.

2D-IR spectra were obtained by the following algorithm: at a given waiting time between the pump and probe pulses, one of the pump pulses was scanned from -400 to 400 fs with respect to the second one to create the coherence time interval. The exact delay between the two pump pulses was calculated from the

interference pattern obtained from a backstage Michelson interferometer referenced to a 3.39 μm CW He-Ne laser. The zero delay between the pump pulses was determined by fitting their interference pattern by a cosine function modulated by a Gaussian. For each OPA pulse (1 kHz repetition rate), the spectrum of the probe pulse was measured by a 64 element MCT detector providing the ω_3 (probe frequency) dimension. The real part of the Fourier transformation over the coherence time provided the ω_1 (excitation frequency) dimension in the 2D IR spectrum. To avoid the situation when the probe pulse appears in between pump pulses during the coherence time scan, the spectrum with the positive coherence time was mirrored to the negative coherence time. For measuring a frequency-resolved pump-probe spectrum, only one pump pulse was used, with a synchronous chopper inserted into the pump beam path.

All experiments were performed at room temperature of 295±0.5 K. The presence of water content was controlled by measuring the absorption spectrum of the solution before and after each experimental session (~8-10 hours); it appeared to stay negligibly low during the session. The blank pump-probe experiments were performed on the solvent (MeCN) alone, with the obtained signal by a factor of at least 10 lower than that for alcohol solutions, even in the region of the pulse overlap. Therefore, this signal can be safely disregarded.

4.4.2 Molecular dynamics simulations

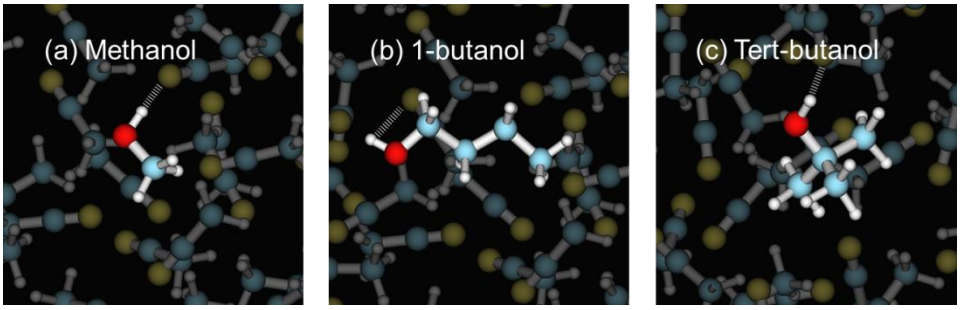

Figure 4.10 Illustration of the molecular dynamics simulations boxes for (a) methanol, (b) 1-butanol, (c) tert-butanol in MeCN. The HBs are depicted by the dash white line. The oxygen atoms are represented in red, the hydrogen in white, the carbons in light blue, and the nitrogen in yellow.

Molecular dynamics (MD) simulations of diluted methanol, 1-butanol, and tert-butanol (as representative alcohols) in MeCN were performed, using the GROMACS 4.6.1 suite.[47] The simulation boxes were composed by 1 molecule of the respective alcohol and 200 molecules of MeCN (Figure 4.10). The interactions between the molecules were described by using the Optimized Potential for Liquid Simulations all-atom (OPLS-AA) force field[48] for both solvent and solute. The Lennard-Jones and Coulombic interactions were truncated at 1.1 nm cutoff. The

long range Coulombic interaction were accounted using the Particle Mesh Ewald (PME) scheme.[49] After initial equilibration, a 5 ns constant volume and temperature of 298.15 K production run was obtained using the Berendsen thermostat.[50] The snapshots were stored at 10 fs intervals, and all bonds were constrained using the LINCS algorithm.[51]

4.4.3 Spectral calculations

The time-dependent vibrational Hamiltonian for the OH stretch[5,52] was generated from the production run, and has the form:

$$H(t) = \omega_{10}(t)B^{\dagger}B - \Delta B^{\dagger}B^{\dagger}BB + \vec{\mu}(t)\vec{E}(t)(B^{\dagger} + B) \qquad \text{(Eq. 4.1)}$$

Here, the $B^{\dagger}$ and B are the bosonic creation and annihilation operators, $\vec{E}(t)$ is the external electric field used to excite the OH oscillator, and Δ is the anharmonicity (fixed at the experimental value of 200 cm^{-1}). This form of the Hamiltonian implies that the harmonic rule is applied for the |1>◊|2> transition dipoles.[5]

The site frequency of the OH stretch $\omega_{10}(t)$ and the transition dipole, $\vec{\mu}(t)$, were calculated for all stored snapshots of the production run, making use of existing electrostatic maps for the OH stretch.[52,53] These relate the electrostatic field E_{OH} created by the force field point charges on the hydrogen atom of the hydroxyl group in the direction along the OH bond, with the site frequency and the transition dipole. We used the electrostatic map developed for the OH stretch of water[52,53], which were built using electronic structure calculations (DFT) of water clusters. Even though this mapping was developed for the OH stretch of water, such approach has previously been successfully applied to alcohols[30,54].

$$\omega_{10}(t) = 3761.6 - 5060.4E_{OH}(t) - 86.225\left(E_{OH}(t)\right)^2 \qquad \text{(Eq. 4.2)}$$

$$x_{10}(t) = 0.1024 - 1.29 \times 10^{-5}\omega_{10}(t) \qquad \text{(Eq. 4.3)}$$

$$\vec{\mu}(t) = (0.71116 - 75.591\, E_{OH}(t))\, \mu_g'\vec{u}_{OH}(t)x_{10}(t) \qquad \text{(Eq. 4.4)}$$

Here, the frequency $\omega_{10}(t)$, OH oscillator displacement $x_{10}(t)$, and electric field $E_{OH}(t)$ have units of wavenumbers, Ångstrøm and E_h/a_0e, respectively. μ_g' is equal to 0.18749*e*, and $\vec{u}_{OH}$ is a unit vector along the OH bond in the direction of hydrogen

All spectra were calculated using the Numerical Integration of Schrödinger Equation (NISE) method[55], in which the time-dependent Schrödinger equation is numerically propagated for the OH stretch time-dependent Hamiltonian thus allowing the calculation of both linear and third-order response functions. An *ad*

hoc vibrational lifetime for the OH stretch of 1 ps was used for appodization. The coherence times were varied from 0 to 640 fs. The response functions were Fourier transformed to obtain the FTIR and 2D IR spectra. Sampling was done at 1 ps intervals along the 5 ns trajectories, giving a total number of 5000 realizations.

4.5 Supporting Information

4.5.1 Determination of the solution concentration range

Analysis of absorption spectra provides the concentration range from which the alcohol molecules tend to form clusters. Figure S4.1 shows the absorption spectra in the spectral range of the OH-stretching mode of all studied alcohols at different molar ratios between alcohol and acetonitrile (MeCN). All obtained spectra show a strong absorption peak at ~3535 cm^{-1} corresponding to the OH-stretching mode[13]. The frequency shift of the OH stretching mode of ~200 cm^{-1} to blue in comparison to the alcohol clusters and bulk alcohols[13,30] indicates that the alcohol molecules stay well separated at the lowest concentration. However, with the increase of concentration, a red shoulder at ~3450 cm^{-1} begins to develop. Following Farwaneh *et al.*[13], this shoulder is ascribed to absorption of coexisting cyclic alcohol trimers (3450 cm^{-1}) and complexes (3450 cm^{-1}), which consist of one MeCN and two alcohol molecules, because HBs between them are stronger than those between the alcohol and MeCN molecules.

To determine the molar ratios where the alcohol molecules are separated, we plot in Figure S4.2 the dependence of OD on the alcohol-acetonitrile molar ratio at the main peak frequency (~3535 cm^{-1}) and at the frequency, which corresponds to absorptions of alcohol oligomers (3400 cm^{-1}). The dependence at 3400 cm^{-1} is quadratic at low molar ratios as expected from bi-molecular interactions. Later it becomes linear which indicates that the dimers concentration is saturated. The inflection point between the two regimes varies from 0.03 to 0.05 for the alcohols studied (0.03 for methanol, 1-propanol, and tert-butanol, 0.04 for ethanol, 1-butanol and 2-methyl-1-propanol, and 0.05 for 2-propanol and 2-butanol). For further experiments the molar ratio of 0.03 was chosen as a compromise between unwanted clustering, the signal-to-noise ratio and alcohol-acetonitrile relative contribution to the 2D-IR signals.

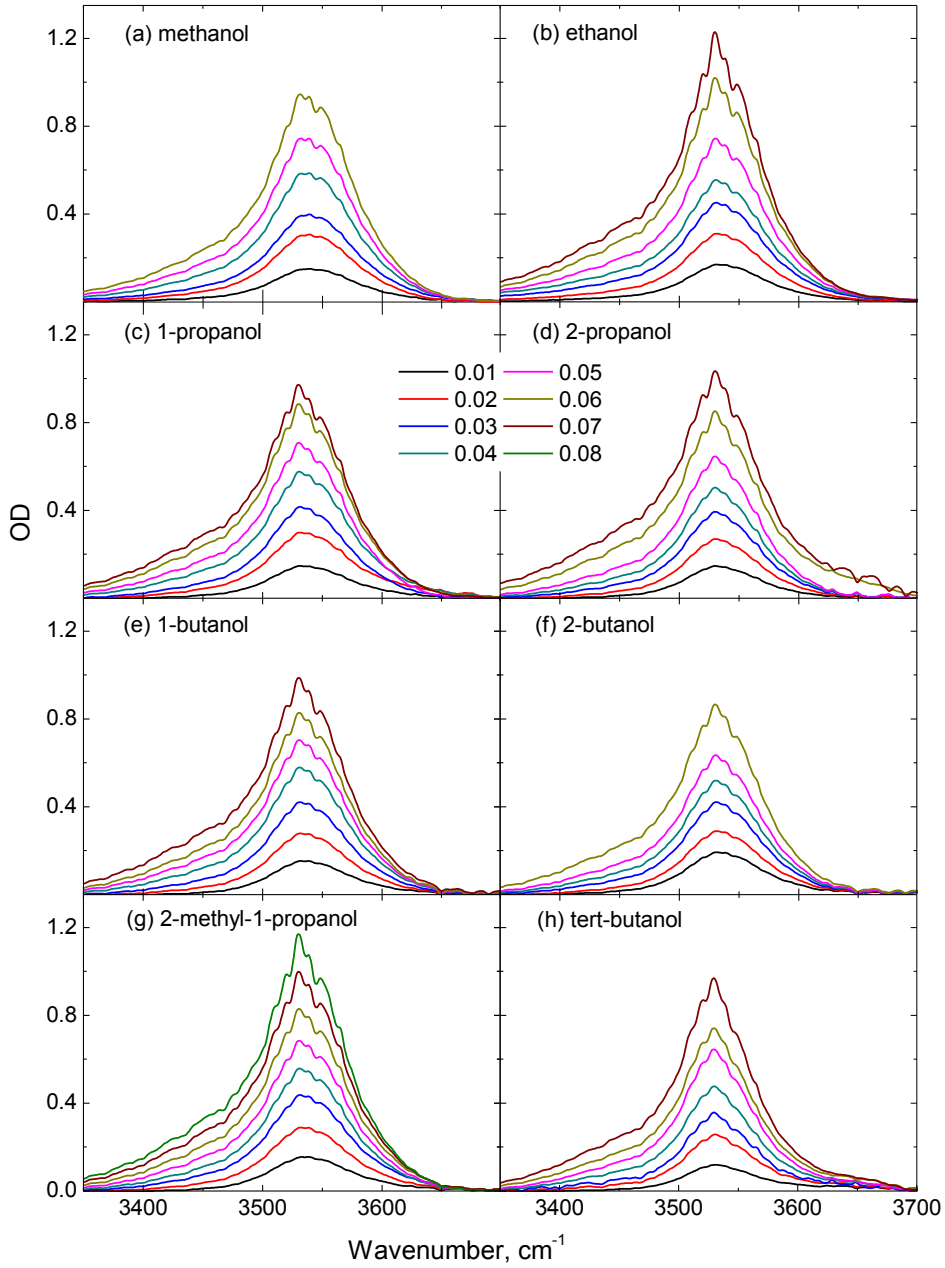

Figure S4.1 Linear absorption spectrum of the OH-stretching region of (a) methanol, (b) ethanol, (c) 1-propnaol, (d) 2-propanol, (e) 1-butanol, (f) 2-butanol, (g) 2-methyl-1-propanol and (h) tert-butanol dissolved in MeCN. Molar ratios of alcohol to MeCN are shown in the legend. Sample thickness is 100 µm.

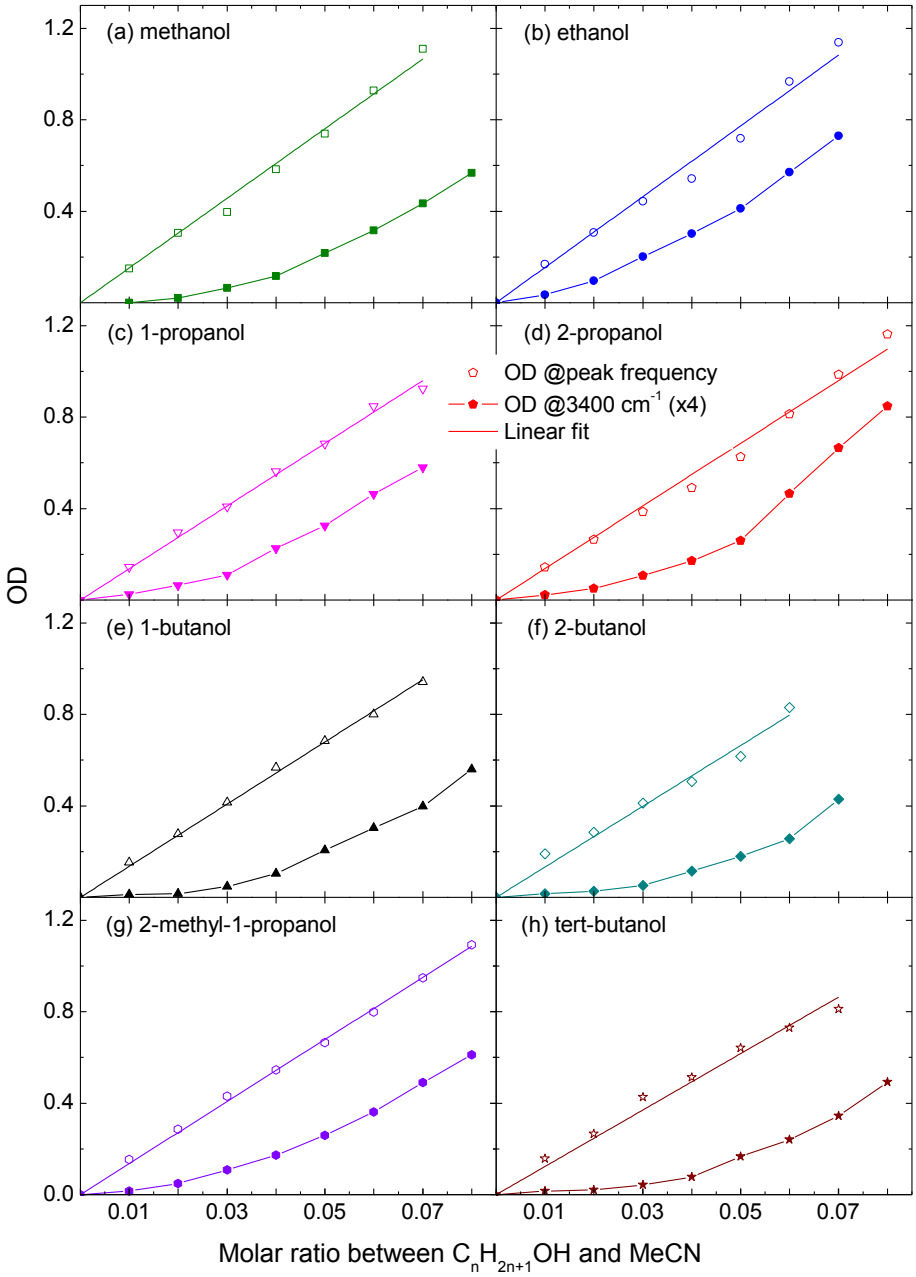

Figure S4.2 Dependence of OD on the alcohol-acetonitrile molar ratio at the frequency OH-stretching mode (3535 cm-1) and at 3400 cm-1 for all studied alcohol solutions: (a) methanol, (b) ethanol, (c) 1-propnaol, (d) 2-propanol, (e) 1-butanol,(f) 2-butanol, (g) 2-methyl-1-propanol and (h) tert-butanol.

4.5.2 Absorption spectra of the samples

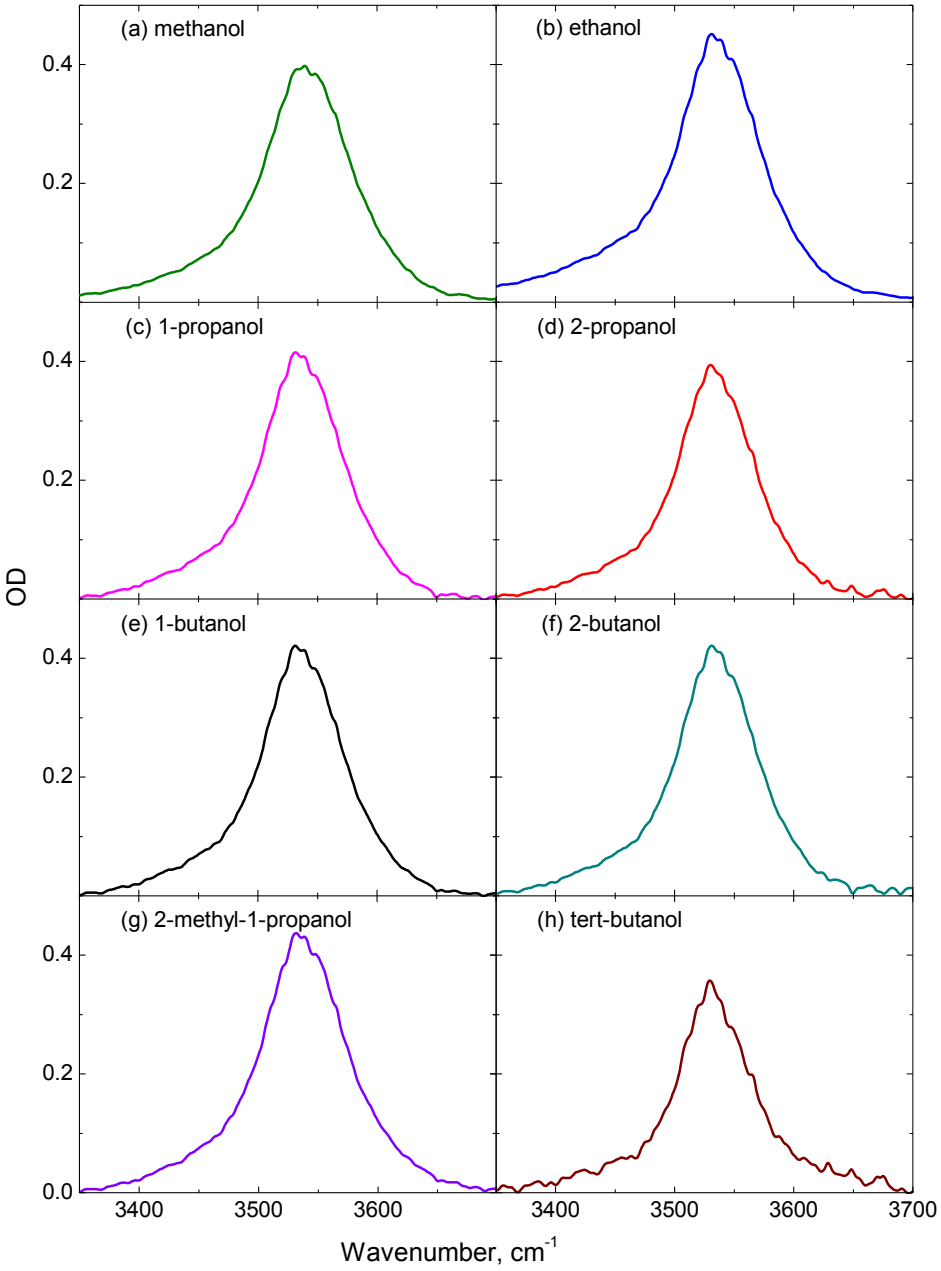

Figure S4.3 Linear absorption spectrum of solutions used in pump-probe and 2D experiments. The molar ratio of alcohols to MeCN is 0.03 and the spectra are shown in the OH stretching region for (a) methanol, (b) ethanol, (c) 1-propanol, (d) 2-propanol, (e) 1-butanol, (f) 2-butanol, (g) 2-methyl-1-propanol and (h) tert-butanol dissolved in MeCN.

4.5.3 Central frequency and width of absorption spectra

To determine the central position of the absorption peaks (Figure S4.4 (a)), its top part at 80% of the maximum level, was fitted with a Gaussian function. The full width at half maximum (FWHM) values were calculated directly from the absorption spectra (Figure S4.4 (b)). Neither value shows a strong dependence on the size of the alkyl chain group (Figure S4.4); however, both central frequencies and widths tend to decrease with an increase of the size of the alkyl chain. In contrast, the calculated central frequencies increase (albeit slightly) while the spectral widths are hardly changed with the increase of the size of the alkyl chain group. This signifies that the classical force fields used are not fully optimized for this type of modelling.

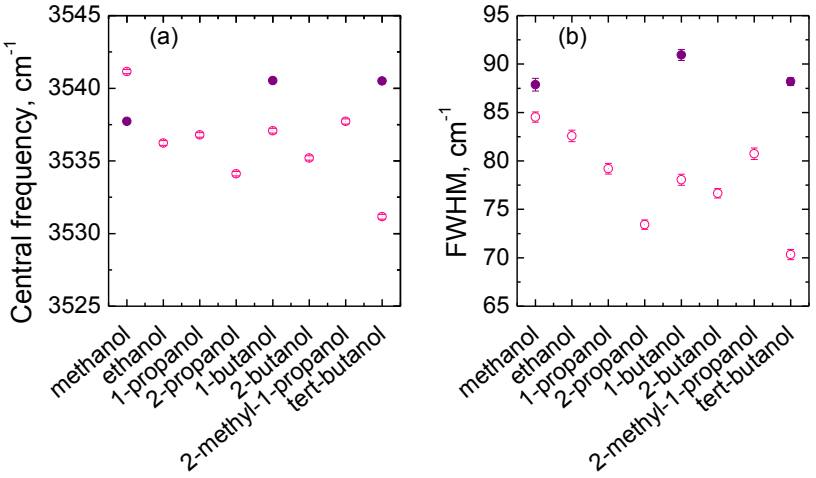

Figure S4.4 (a) Central frequencies and (b) full width half maximum (FWHM) values of the experimental (open circles) and simulated (filled circles) spectra for all studied alcohols.

4.5.4 Pump-probe

Isotropic transient absorption spectra at different delay times and the pump-probe transients at the frequency of maximum bleaching (3535 cm^{-1}) and induced absorption (3370 cm^{-1}) with fits are shown in Figure S4.5 and Figure S4.6, respectively, for all studied alcohols. At short delay times, the isotropic transient spectra are mostly dominated by bleaching (related to |0>-|1> transition) with the peak at ~3535 cm^{-1} and an induced absorption band (related to |1>-|2> transition) at the low frequency side at ~3370 cm^{-1}. The anharmonicity of 170 cm^{-1} was calculated as a frequency shift between the peaks of induced absorption and bleaching/simulated emission.

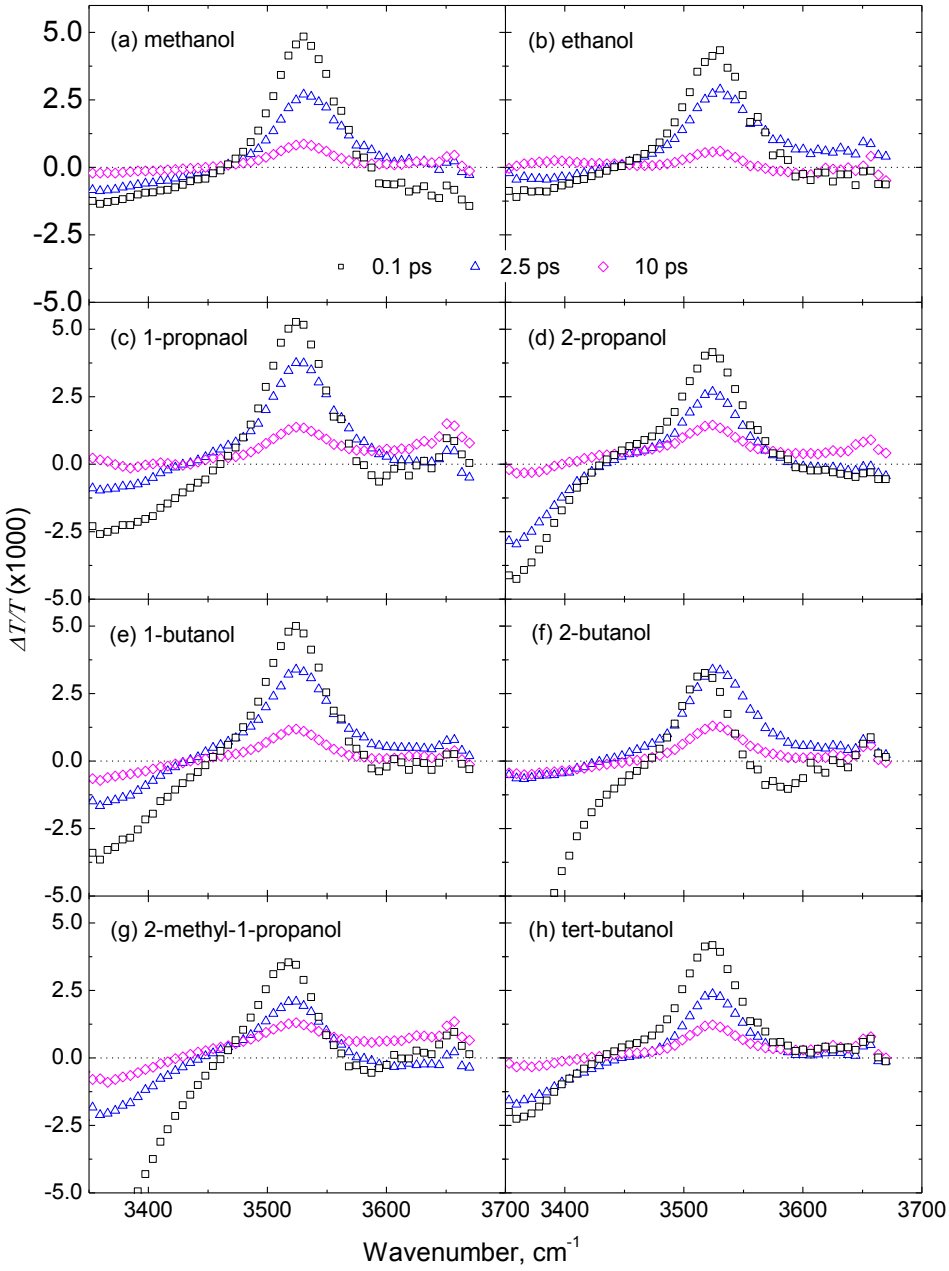

Figure S4.5 Isotropic pump-probe transient spectra at different delay times (shown in the legend) for (a) methanol, (b) ethanol, (c) 1-propanol, (d) 2-propanol, (e) 1-butanol, (f) 2-butanol, (g) 2-methyl-1-propanol and (h) tert-butanol dissolved in MeCN.

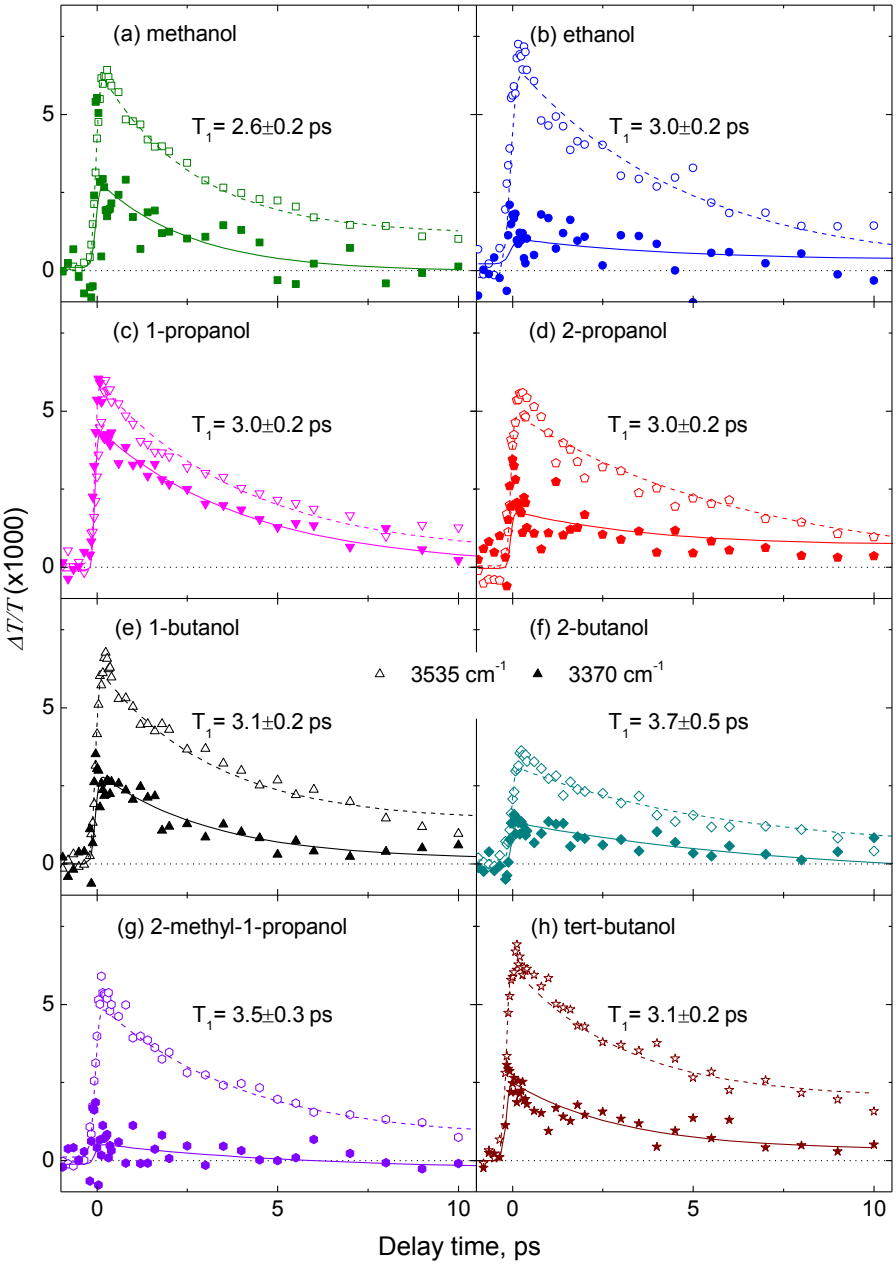

Figure S4.6 Experimental transients (symbols) at bleaching/stimulated emission (3535 cm^{-1}, open circles) and induced absorption (3370 cm^{-1}, filled circles, the sign is inverted) regions for (a) methanol, (b) ethanol, (c) 1-propanol, (d) 2-propano, (e) 1-butanol, (f) 2-butanol, (g) 2-methyl-1-propanol and (h) tert-butanol diluted in MeCN. The fits obtained from a kinetic model (Figure S4.7) are shown by the lines with the corresponding lifetimes T_1 indicated.

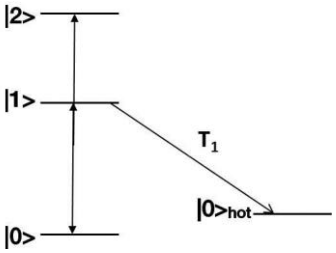

Figure S4.7 Energy level diagram for the three-level kinetic model[6]. The excited |1> state of the OH-stretching mode relaxes to the hot ground state $|0\rangle_{hot}$, which corresponds to the temperature increase in the excitation volume at long times.

The pump-probe spectra, measured at short delay time and long delay time (Figure S4.5, black and magenta symbols, respectively) substantially differ from each other. Such behavior is usually associated with the population relaxation to the "hot" ground state (Figure S4.7) where the deposed into the OH stretch IR energy causes a temperature jump in the local volume due to energy redistribution among low-frequency collective modes[56,57]. To extract the OH stretch lifetime *T*, the pump-probe data for each alcohol was fit with the following function:

$$S(\omega, t) = \left[A(\omega)e^{-\frac{t}{T}} + B(\omega)\left(1 - e^{-\frac{t}{T}}\right)\right] \qquad \text{(Eq. S4.1)}$$

convoluted with a Gaussian apparatus function of ~100 fs width. Here, $A(\omega)$ is the spectral profile of the population contribution represented by a sum of two Gaussian functions:

$$A(\omega) = A_{01}exp\left[-\frac{(\omega - \omega_{01})^2}{2\sigma_{01}}\right] + A_{12}exp\left[-\frac{(\omega - \omega_{12})^2}{2\sigma_{12}}\right] \qquad \text{(Eq. S4.2)}$$

where A_{01} and A_{12}, ω_{01} and ω_{12}, σ_{01} and σ_{12} are the local parameters, stand for the amplitude, frequencies and widths of the |0>-|1> and |1>-|2> transitions, respectively. $B(\omega)$ is the spectral profile of the thermal contribution that was also represented by an *ad hoc* combination of two Gaussians and a baseline.

The model described above was used to derive the lifetime of the OH-stretching mode and the timescale of the thermalization effect (~ 20 ps). Therefore, the 2D IR spectra at waiting times shorter than 5 ps have a negligible thermal contribution.

4.5.5 Temperature jump in the hot ground state

To estimate the temperature jump, the linear absorption spectra of the studied solutions were measures at different temperature and their difference was compared with the transient absorption spectrum at the delay time of 10 ps (Figure S4.8). The temperature jump was estimated as ~0.3-0.5 K. Calculations based on the direct conversion of the absorbed pump energy (~0.9 μJ) into heat in the focal volume of ~4*10^{-7} cm^3 (the beam waist of ~100 μm, the jet thickness of 50 μm) resulted in the temperature jump of ~0.9 K.

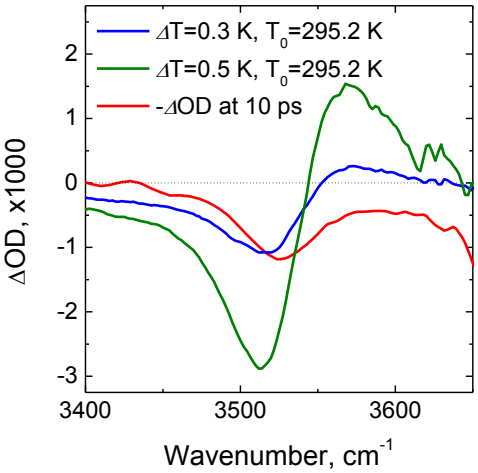

Figure S4.8 The difference absorption spectra of 1-propanol/MeCN solution at two temperatures (blue and green lines) and experimental pump-probe spectrum at the delay of 10 ps (the red line).

4.5.6 2D-IR spectra

2D-IR spectra for all alcohols (in comparison with the experimental ones, if applicable) at a few waiting times of 0 ps, 0.1 ps, 0.5 ps, 1 ps and 3 ps are shown in Figure S4.9. The 2D-IR spectra are similar for all alcohols: at short waiting times the correlation between excitation and probing frequencies is high and, as the result, the 2D-IR spectra are diagonally elongated. Increasing of the waiting time leads to the correlation loss, which makes the shape of the spectrum to change to more round-like.

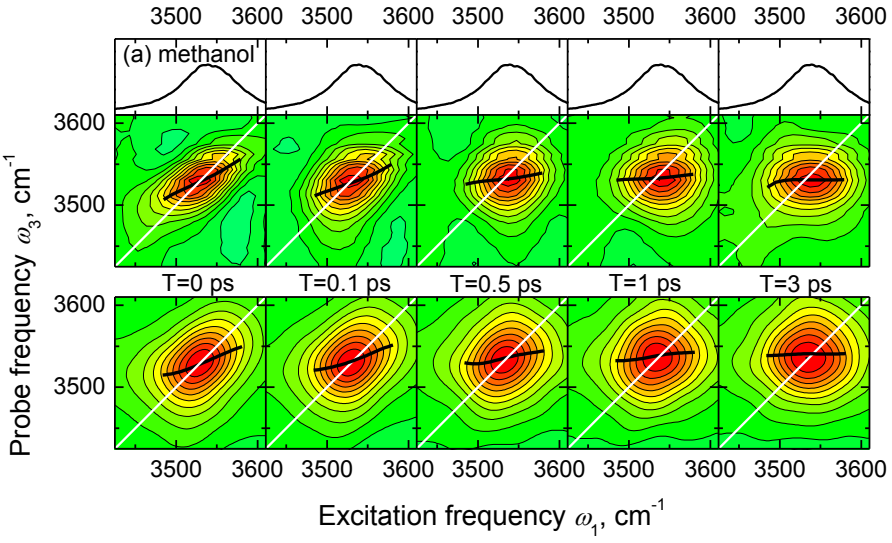
(a) methanol
T=0 ps
T=0.1 ps
T=0.5 ps
T=1 ps
T=3 ps
Probe frequency ω_3, cm^{-1}
Excitation frequency ω_1, cm^{-1}
3500
3600

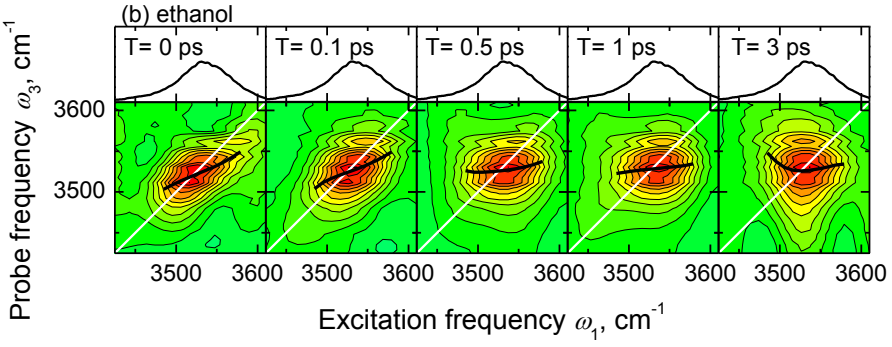
(b) ethanol
T= 0 ps
T= 0.1 ps
T= 0.5 ps
T= 1 ps
T= 3 ps
Probe frequency ω_3, cm^{-1}
Excitation frequency ω_1, cm^{-1}
3500
3600

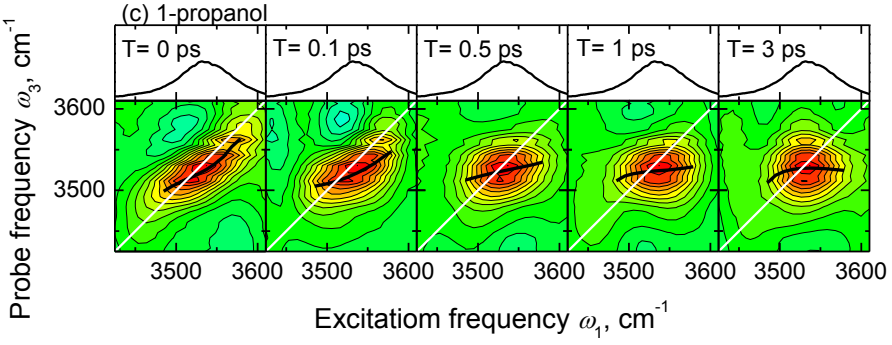
(c) 1-propanol
T= 0 ps
T= 0.1 ps
T= 0.5 ps
T= 1 ps
T= 3 ps
Probe frequency ω_3, cm^{-1}
Excitatiom frequency ω_1, cm^{-1}
3500
3600

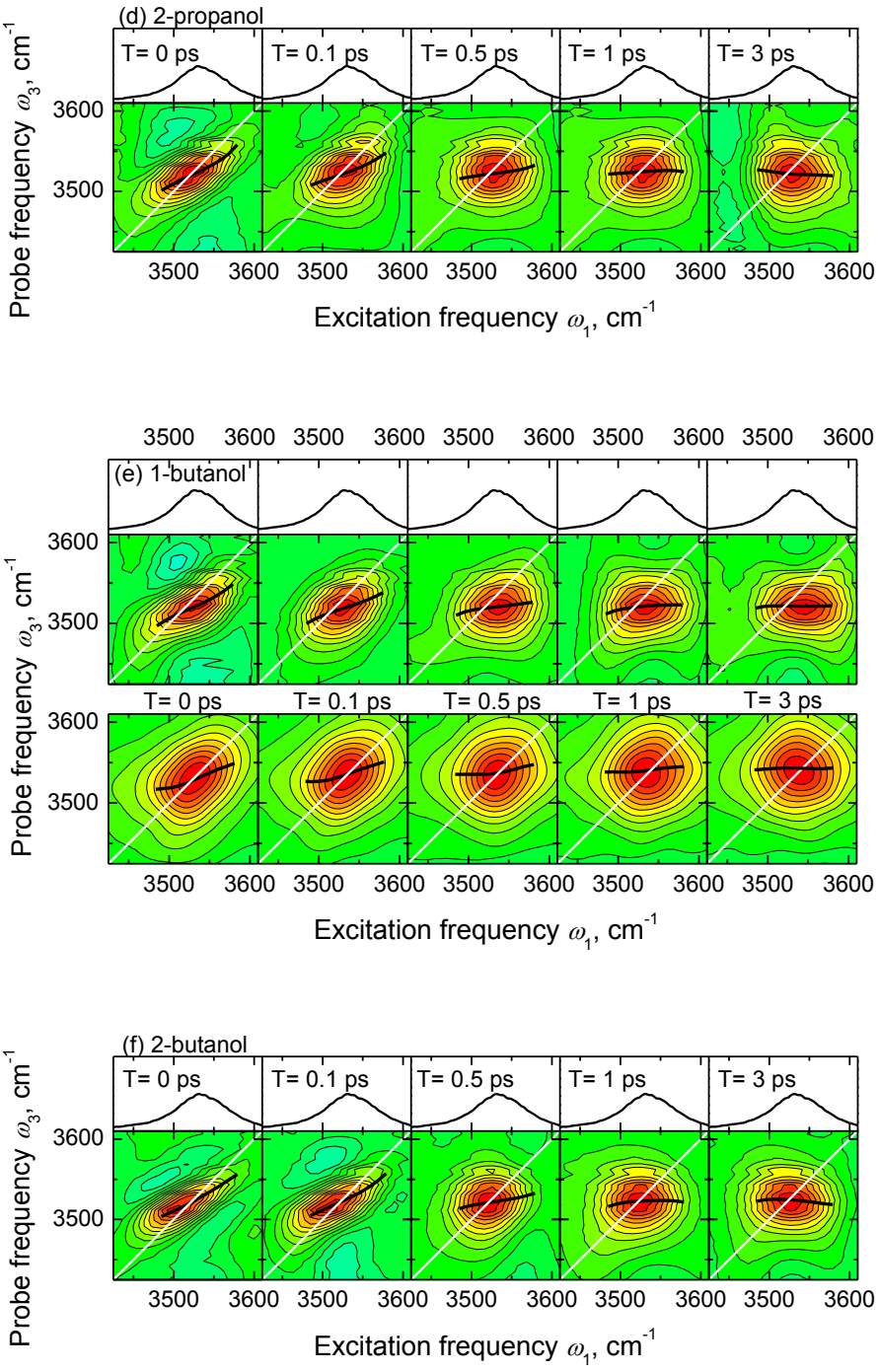
(d) 2-propanol
T= 0 ps
T= 0.1 ps
T= 0.5 ps
T= 1 ps
T= 3 ps
Probe frequency ω_3, cm^{-1}
Excitation frequency ω_1, cm^{-1}
(e) 1-butanol
(f) 2-butanol
3500
3600

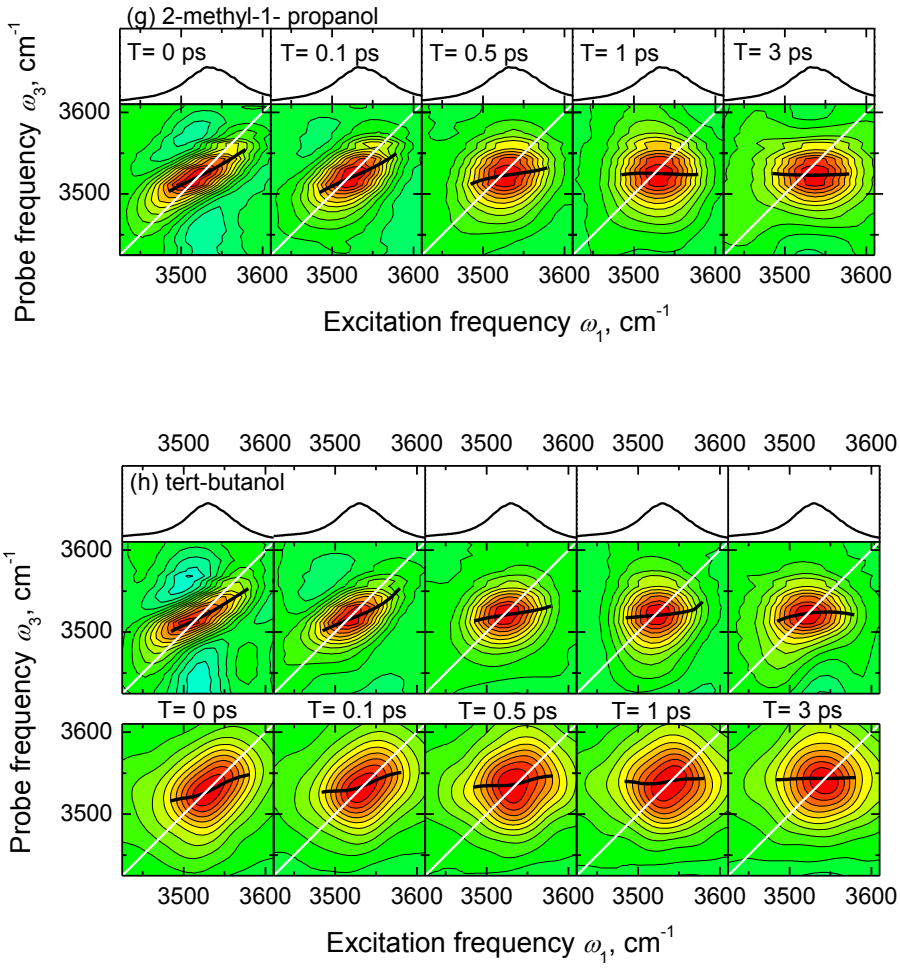

Figure S4.9 Experimental absorption spectra (top panels), experimental (middle panels) and simulated (bottom panels, if applicable) 2D-IR spectra in the OH-stretching mode region for MeCN solution of (a) methanol, (b) ethanol, (c) 1-propanol, (d) 2-propanol, (e) 1-butanol, (f) 2-butanol, (g) 2-methyl-1-propanol and (h) tert-butanol at a few representative waiting times. The 2D spectra are normalized to the maximal amplitude; only the bleaching region is shown. The equidistant contours are drawn with a 10% step of the maximal amplitude. The results of the CLS analysis are depicted by black lines. The simulated spectra (if applicable) are blue-shifted by 50 cm^{-1} along both axes for ease of comparison.

4.5.7 Center Line Slope analysis

To extract the system-bath frequency-frequency correlation function, the center line slope (CLS) analysis[48] was applied in OH-stretching mode region (3485-3580 cm^{-1}, thick black lines in Figure S4.9). Figures S4.10 and S4.11 show the results of the CLS analysis for all and individual alcohols and all alcohols, respectively. To extract the time scales, the obtained CLS dynamics were fitted with bi-exponential

functions (see Figure S4.12 for their parameters). All alcohols show similar behavior with no dependence on the size of alkyl chain group. The following timescales are obtained from the fit to the CLS data: the fast one amounts to ~200 fs (~80% share) and the slow one of ~4 ps (~20% share). With MD simulations at hand, the fast component was attributed to OH-librations while the slow one originates from diffusional motion of the molecule.

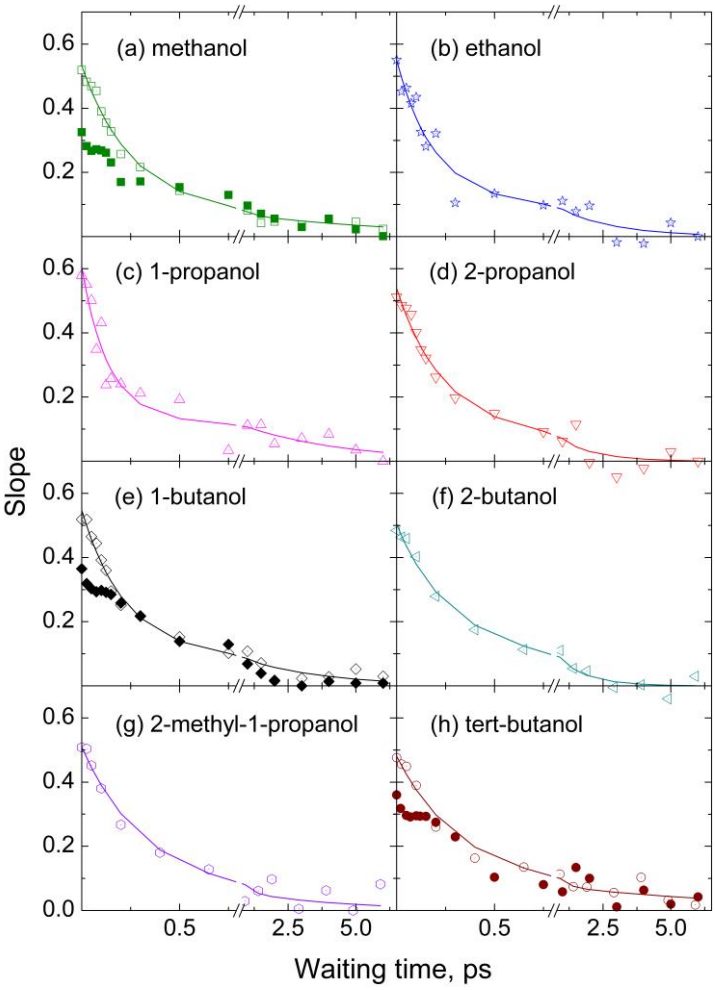

Figure S4.10 Center line slope analysis, obtained from experimental 2D IR spectra for all studied alcohols: (a) methanol, (b) ethanol, (c) 1-propanol, (d) 2-propanol, (e) 1-butanol, (f) 2-butanol, (g) 2-methyl-1-propanol, (h) tert-butanol, obtained from experimental 2D IR spectra. The values of central line slope analysis, obtained from MD simulations for (a) methanol, (e) 1-butanol and (h) tert-butanol, are shown by filled symbols. Biexponential fits are shown by the solid lines; their parameters are summarized in Figure S4.11.

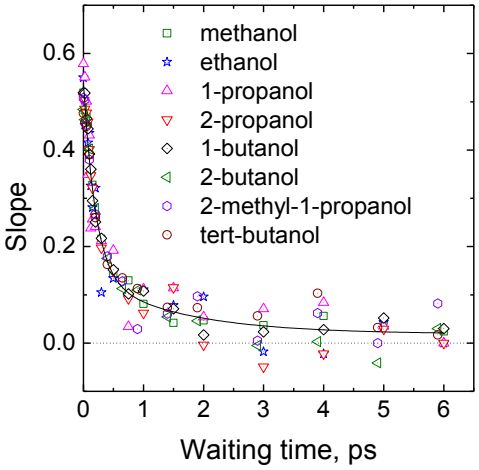

Figure S4.11 The same as in Figure S4.10, but all CLSs are depicted altogether. The averaged biexponential fit is shown by the thin black line.

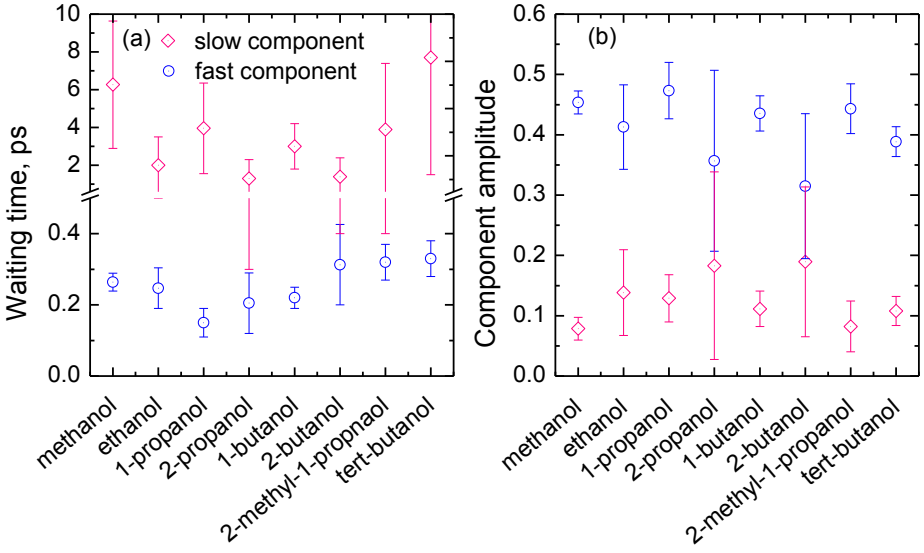

Figure S4.12 Parameters of the biexponential fits to the CLS dynamics (Figure S4.10). (a) decay times, (b) amplitudes.

Author Contributions

ES performed the experiments under the supervision of KS. AC and TLCJ performed all theoretical calculations; MSP supervised the research. The manuscript was written by ES and AC under the supervision of TLCJ and MSP.

4.6 References

(1) Arunan, E.; Desiraju, G. R.; Klein, R. A.; Sadlej, J.; Scheiner, S.; Alkorta, I.; Clary, D. C.; Crabtree, R. H.; Dannenberg, J. J.; Hobza, P.; et al. Definition of the Hydrogen Bond. *Pure Appl. Chem.* **2011**, 83, 1637–1641.

(2) Schuster, P.; Zundel, G.; Sandorfy, C. *The Hydrogen Bond - Recent Developments in Theory and Experiment*; Schuster, P., Zundel, G., Sandorfy, C., Eds.; North-Holland: Amsterdam, 1976.

(3) Wahl, M. C_H…O Hydrogen Bonding in Biology. *Trends Biochem. Sci.* **1997**, 22, 97–102.

(4) Cho, M. Coherent Two-Dimensional Optical Spectroscopy. *Chem. Rev.* **2008**, 108, 1331–1418.

(5) Hamm, P.; Zanni, M. T. *Concepts and Methods of 2D Infrared Spectroscopy*; Cambridge University Press: Cambridge, U.K., 2011.

(6) Ashihara, S.; Huse, N.; Espagne, A.; Nibbering, E. T. J.; Elsaesser, T. Ultrafast Structural Dynamics of Water Induced by Dissipation of Vibrational Energy. *J. Phys. Chem. A* **2007**, 111, 743–746.

(7) Lock, A. J.; Bakker, H. J. Temperature Dependence of Vibrational Relaxation in Liquid Temperature Dependence of Vibrational Relaxation in Liquid H_2O. *J. Chem. Phys.* **2002**, 117, 1708–1713.

(8) Cringus, D.; Bakulin, A.; Lindner, J.; Vöhringer, P.; Pshenichnikov, M. S.; Wiersma, D. A. Ultrafast Energy Transfer in Water - AOT Reverse Micelles. *J. Phys. Chem. B* **2007**, 111, 14193–14207.

(9) Cringus, D.; Lindner, J.; Milder, M. T. W.; Pshenichnikov, M. S.; Vöhringer, P.; Wiersma, D. A. Femtosecond Water Dynamics in Reverse-Micellar Nanodroplets. *Chem. Phys. Lett.* **2005**, 408, 162–168.

(10) Bellamy, L. J.; Pace, R. J. The Nature Oi the Hydrogen Bond in Alcohol:dimers and Polymers. *Spectrochim. Acta* **1966**, 22, 525–533.

(11) Asprion, N.; Hasse, H.; Maurer, G. FT-IR Spectroscopic Investigations of Hydrogen Bonding in Alcohol-Hydrocarbon Solutions. *Fluid Phase Equilib.* **2001**, 186, 1–25.

(12) Mizuno, K.; Miyashita, Y.; Shindo, Y.; Ogawa, H. NMR and FT-IR Studies of Hydrogen Bonds in Ethanol-Water Mixtures. *J. Phys. Chem.* **1995**, 99, 3225–3228.

(13) Farwaneh, S. S.; Yarwood, J.; Cabaço, I.; Besnard, M. Infrared Studies of Hydrogen-Bonding of Methanol in Binary Mixtures with Acetonitrile. *J. Mol. Liq.* **1993**, 56, 317–332.

(14) Asbury, J. B.; Steinel, T.; Fayer, M. D. Hydrogen Bond Networks: Structure and Evolution after Hydrogen Bond Breaking. *J. Phys. Chem. B* **2004**, 108, 6544–6554.

(15) Gulmen, T. S.; Sibert III, E. L. Vibrational Energy Relaxation of the OH(D) Stretch Fundamental of Methanol in Carbon Tetrachloride. *J. Chem. Phys.* **2005**, 123, 204508.

(16) Kwac, K.; Geva, E. A Mixed Quantum-Classical Molecular Dynamics Study of the Hydroxyl Stretch in Methanol/carbon Tetrachloride Mixtures III: Nonequilibrium Hydrogen-Bond Dynamics and Infrared Pump-Probe Spectra. *J. Phys. Chem. B* **2013**, 117, 7737–7749.

(17) Kuen, D. S.; Feierabend, K. J. Cavity-Enhanced Overtone Spectroscopy of Methanol in Aprotic Solvents: Probing Solute-Solvent Interactions and Self-Associative Behavior. *J. Phys. Chem. A* **2014**, 118, 2942–2951.

(18) Laenen, R.; Gale, G. M.; Lascoux, N. IR Spectroscopy of Hydrogen-Bonded Methanol: Vibrational and Structural Relaxation on the Femtosecond Time Scale. *J. Phys. Chem. A* **1999**, 103, 10708–10712.

(19) Piletic, I. R.; Gaffney, K. J.; Fayer, M. D. Structural Dynamics of Hydrogen Bonded Methanol Oligomers: Vibrational Transient Hole Burning Studies of Spectral Diffusion. *J. Chem. Phys.* **2003**, 119, 423–434.

(20) Woutersen, S.; Emmerichs, U.; Bakker, H. J. A Femtosecond Midinfrared Pump-Probe Study of Hydrogen-Bonding in Ethanol. *J. Chem. Phys.* **1997**, 107, 1483–1490.

(21) Yokozeki, A.; Kasprzak, D. J.; Shiflett, M. B. IR-Spectroscopic Studies of Hydrogen-Bonding Solutions: Lineshape Analysis of Ethanol + Hexane System. *Appl. Energy* **2007**, 84, 863–873.

(22) Levinger, N. E.; Davis, P. H.; Fayer, M. D. Vibrational Relaxation of the Free Terminal Hydroxyl Stretch in Methanol Oligomers: Indirect Pathway to Hydrogen Bond Breaking. *J. Chem. Phys.* **2001**, 115, 9352–9360.

(23) Matsumoto, M.; Gubbins, K. E. Hydrogen Bonding in Liquid Methanol. *J. Chem. Phys.* **1990**, 93, 1981–1994.

(24) Nishi, N.; Takahashi, S.; Matsumoto, M.; Tanaka, A.; Muraya, K.; Takamuku, T.; Yamaguchi, T. Hydrogen Bonding Cluster Formation and Hydrophobic Solute Association in Aqueous Solution of Ethanol. *J. Phys. Chem* **1995**, 99, 462–468.

(25) Pagliai, M.; Cardini, G.; Righini, R.; Schettino, V. Hydrogen Bond Dynamics in Liquid Methanol. *J. Chem. Phys.* **2003**, 119, 6655–6662.

(26) Shaw, D. J.; Panman, M. R.; Woutersen, S. Evidence for Cooperative Vibrational Relaxation of the NH-, OH-, and OD-Stretching Modes in Hydrogen-Bonded Liquids Using Infrared Pump-Probe Spectroscopy. *Phys. Rev. Lett.* **2009**, 103, 227401.

(27) Vartia, A. A.; Mitchell-Koch, K. R.; Stirnemann, G.; Laage, D.; Thompson, W. H. On the Reorientation and Hydrogen-Bond Dynamics of Alcohols. *J. Phys. Chem. B* **2011**, 115, 12173–12178.

(28) Venables, D. S.; Schmuttenmaer, C. A. Spectroscopy and Dynamics of Mixtures of Water with Acetone, Acetonitrile, and Methanol. *J. Chem. Phys.* **2000**, 113, 11222–11236.

(29) Gaffney, K. J.; Davis, P. H.; Piletic, I. R.; Levinger, N. E.; Fayer, M. D. Hydrogen Bond Dissociation and Reformation in Methanol Oligomers Following Hydroxyl Stretch Relaxation. *J. Phys. Chem. A* **2002**, 106, 12012–12023.

(30) Shinokita, K.; Cunha, A. V.; Jansen, T. L. C.; Pshenichnikov, M. S. Hydrogen Bond Dynamics in Bulk Alcohols. *J. Chem. Phys.* **2015**, 142, 212450.

(31) Mazur, K.; Bonn, M.; Hunger, J. Hydrogen Bond Dynamics in Primary Alcohols: A Femtosecond Infrared Study. *J. Phys. Chem. B* **2015**, 119, 1558–1566.

(32) Mesele, O. O.; Vartia, A. A.; Laage, D.; Thompson, W. H. Reorientation of Isomeric Butanols: The Multiple Effects of Steric Bulk Arrangement on Hydrogen-Bond Dynamics. *J. Phys. Chem. B* **2016**, 120, 1546–1559.

(33) Ludwig, R.; Zeidler, M. D.; Farrar, T. C. Molecular Dynamics in Lower Alcohols. *Zeitschrift für Phys. Chemie* **1995**, 189, 19–27.

(34) Lock, A. J.; Gilijamse, J. J.; Woutersen, S.; Bakker, H. J. Vibrational Relaxation and Coupling of Two OH-Stretch Oscillators with an Intramolecular Hydrogen Bond. *J. Chem. Phys.* **2004**, 120, 2351–2358.

(35) Bakulin, A. A.; Liang, C.; Jansen, T. L. C.; Wiersma, D. A.; Bakker, H. J.; Pshenichnikov, M. S. Hydrophobic Solvation: A 2D IR Spectroscopic Inquest. *Acc. Chem. Res.* **2009**, 42, 1229–1238.

(36) Kwak, K.; Park, S.; Finkelstein, I. J.; Fayer, M. D. Frequency-Frequency Correlation Functions and Apodization in Two-Dimensional Infrared Vibrational Echo Spectroscopy: A New Approach. *J. Chem. Phys.* **2007**, 127, 124503.

(37) Farag, M. H.; Hoenders, B. J.; Knoester, J.; Jansen, T. L. C. Spectral Line Shapes in Linear Absorption and Two-Dimensional Spectroscopy with Skewed Frequency Distributions. *J. Chem. Phys.* **2017**, 146, 234201.

(38) Dinpajooh, M.; Matyushov, D. V. Non-Gaussian Lineshapes and Dynamics of Time-Resolved Linear and Nonlinear (Correlation) Spectra. *J. Phys. Chem. B* **2014**, 118, 7925–7936.

(39) Roy, S.; Pshenichnikov, M. S.; Jansen, T. L. C. Analysis of 2D CS Spectra for Systems with Non-Gaussian Dynamics. *J. Phys. Chem. B* **2011**, 115, 5431–5440.

(40) Jansen, T. L. C.; Cringus, D.; Pshenichnikov, M. S. Dissimilar Dynamics of Coupled Water Vibrations. *J. Phys. Chem. A* **2009**, 113, 6260–6265.

(41) de Boeij, W. P.; Pshenichnikov, M. S.; Wiersma, D. A. Ultrafast Solvation Dynamics Explored by Femtosecond Photon Echo Spectroscopies. *Annu. Rev. Phys. Chem* **1998**, 49, 99–123.

(42) Cringus, D.; Yeremenko, S.; Pshenichnikov, M. S.; Wiersma, D. A. Hydrogen Bonding and Vibrational Energy Relaxation in Water-Acetonitrile Mixtures. *J. Phys. Chem. B* **2004**, 108, 10376–10387.

(43) Luzar, A.; Chandler, D. Hydrogen-Bond Kinetics in Liquid Water. *Nature* **1996**, 379, 55–57.

(44) Kryachko, E. S.; Nguyen, M. T. Hydrogen Bonding between Phenol and Acetonitrile. *J. Phys. Chem. A* **2002**, 106, 4267–4271.

(45) Yeremenko, S.; Baltuška, A.; de Haan, F.; Pshenichnikov, M. S.; Wiersma, D. A. Frequency-Resolved Pump–probe Characterization of Femtosecond Infrared Pulses. *Opt. Lett.* **2002**, 27, 1171–1173.

(46) Helbing, J.; Hamm, P. Compact Implementation of Fourier Transform Two-Dimensional IR Spectroscopy without Phase Ambiguity. *J. Opt. Soc. Am. B* **2011**, 28, 171–178.

(47) Berendsen, H. J. C.; van der Spoel, D.; van Drunen, R. GROMACS: A Message-Passing Parallel Molecular Dynamics Implementation. *Comput. Phys. Commun.* **1995**, 91, 43–56.

(48) Jorgensen, W. L.; Maxwell, D. S.; Tirado-Rives, J. Development and Testing of the OLPS All-Atom Force Field on Conformational Energetics and Properties of Organic Liquids. *J. Am. Chem. Soc.* **1996**, 118, 11225–11236.

(49) Essmann, U.; Perera, L.; Berkowitz, M. L.; Darden, T.; Lee, H.; Pedersen, L. G. A Smooth Particle Mesh Ewald Method. *J Chem Phys* **1995**, 103, 8577–8593.

(50) Berendsen, H. J. C.; Postma, J. P. M.; van Gunsteren, W. F.; DiNola, A.; Haak, J. R. Molecular Dynamics with Coupling to an External Bath. *J. Chem. Phys.* **1984**, 81, 3684–3690.

(51) Hess, B.; Bekker, H.; Berendsen, H. J. C.; Fraaije, J. G. E. M. LINCS: A Linear Constraint Solver for Molecular Simulations. *J. Comput. Chem.* **1997**, 18, 1463–1472.

(52) Humphrey, W.; Dalke, A.; Schulten, K. VMD: Visual Molecular Dynamics. *J. Mol. Graph.* **1996**, 14, 33–38.

(53) Auer, B.; Kumar, R.; Schmidt, J. R.; Skinner, J. L. Hydrogen Bonding and Raman, IR, and 2D-IR Spectroscopy of Dilute HOD in Liquid D2O. *Proc. Natl. Acad. Sci. U.S.A.* **2007**, 104, 14215–14220.

(54) van der Vegte, C. P.; Knop, S.; Vöhringer, P.; Knoester, J.; Jansen, T. L. C. OH-Stretching in Synthetic Hydrogen-Bonded Chains. *J. Phys. Chem. B* **2014**, 118, 6256–6264.

(55) Liang, C.; Jansen, T. L. C. An Efficient N^3-Scaling Propagation Scheme for Simulating Two-Dimensional Infrared and Visible Spectra. *J. Chem. Theory Comput.* **2012**, 8, 1706–1713.

Chapter 5

Intra- and Intermolecular Contributions to Exciton Dynamics in Star-Shaped Small Molecules

Small organic molecules of the push-pull architecture are rapidly gaining the importance in the organic electronics applications. In densely packed molecular films, both intra- and intermolecular interactions play an essential role for the device performance. Here we study two different molecules, a highly symmetric star-shaped one and its newly synthesized single arm analogue, for their photophysical properties. Both chromophores were dissolved in a solid matrix at different concentrations to vary their separation and therefore the intermolecular coupling. We show that in both molecules the population relaxation accelerates by more than a factor of 10 at shorter intermolecular distances due to self-quenching thereby reducing the exciton survival time. The transient anisotropy dynamics are also quite similar, with their substantial acceleration at shorter interchromophore distances due to exciton diffusion caused by the Förster-like resonance energy transfer. However, the anisotropy values are noticeably lower for the star-shaped molecule because of intramolecular mixing of different polarization states. Finally, a model is presented that accounts for the observed results.

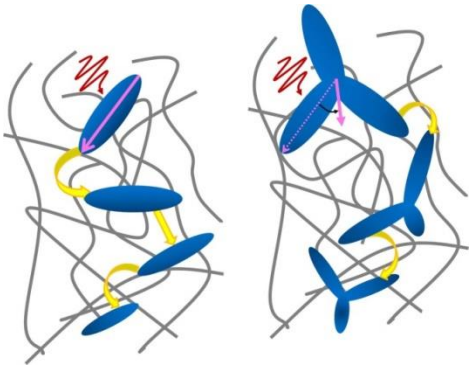

The current chapter is based on the following publication:

Evgeniia Salamatova, Oleg V. Kozlov, Yuriy N. Luponosov, Alexander N. Solodukhin, Victoria Y. Toropynina, Sergei A. Ponomarenko and Maxim S. Pshenichnikov, *Proc. SPIE*.,**2016**, 9923, 99230K.

5.1 Introduction

Organic electronics is a rapidly developing field of science and technology. Organic electronic devices possess number of attractive advantages as light weight, flexibility, simplified mass-scale production etc.[1–4] which makes them indispensable for at least niche applications. The importance of organic electronics is highlighted by a large scale commercial production of organic light-emitting diodes (OLEDs) and intensive research and development of organic solar cells (OSCs)[5–8] and organic field-effect transistors (OFETs)[9–11].

The heart of any organic electronic device is an active layer which is made of an organic semiconductor[12]. Organic semiconductors combine properties of organic materials (solution processability, variety of chemical structures and chemical/physical properties, easiness of processing etc.) with semiconducting behavior[13,14]. However, the electrical and photophysical properties of organic and inorganic semiconductors are essentially different. Due to relatively low dielectric constant of organics (ε~3-4[13,15,16]), the elementary excitations in organic semiconductors at room temperature are not free charges but highly bound electron-hole pairs, the so-called excitons[17,18]. Consequently, the very operation of organic electronic devices relies on dynamics of the excitons.

Push-pull small molecules have been proven as promising candidates as a donor material for OSCs. In particular, the star-shaped small molecules (SSMs) with triphenylamine donor core and dicyanovinyl acceptor end groups have shown a great potential, with OSC efficiency reaching as high as 5.4%[19]. In the OSCs, the SSMs are densely packed in the nm-sized domains which greatly promotes intermolecular interactions[20]. On the other hand, due to high symmetry of the SSM structure, intramolecular energy migration is also important[21]. Therefore, for understanding of the early-time photon-to-charge conversion, it is imperative to distinguish the *inter*- and *intra*molecular contributions to the overall exciton dynamics.

Here, we approach this issue from two different perspectives. First, we remove the molecular symmetry of SSMs by cutting off two out of three arms of the initial SSM (designated as N(Ph-2T-DCV-Et)$_3$)[22,23]. The resulting linear molecule (designated as TPA-2T-DCV-Me) does not possess any symmetry which makes the initial excitation highly anisotropic (Figure 5.1). Second, we vary the intermolecular interactions by dissolving both molecules in a solid polymer matrix at different concentrations. The observables in our experiments are time-resolved photoluminescence (PL) obtained with a streak-camera. We show that both samples demonstrate similar populations dynamics that substantially accelerate at

short interchromophore distances due to self-quenching. Diluted samples of the linear TPA-2T-DCV-Me molecules exhibit a constant anisotropy of 0.4. In contrast, the anisotropy of the diluted N(Ph-2T-DCV-Et)$_3$ samples amounts to a much lower value of ~0.09 which is indicative of ultrafast intramolecular dynamics. As the distance between the chromophores decreases, the transient anisotropy exhibits a decaying behavior with a time constant that rapidly decreases with the decrease of the interchromophore separation. This is indicative of the increasing rate of the Förster-like intermolecular energy transfer.

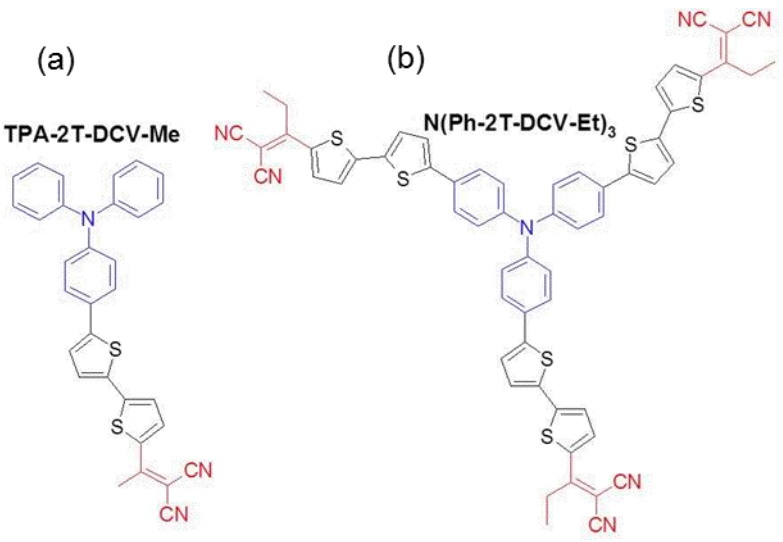

Figure 5.1 Chemical structures of (a) TPA-2T-DCV-Me and (b) N(Ph-2T-DCV-Et)$_3$ molecules.

5.2 Experimental Results

5.2.1 Steady-state absorption and PL spectra

Figure 5.2 shows the absorption and PL spectra of the blends at several representative chromophore separations. The low concentration films exhibit an absorbance peak centered at ~2.5 eV. The decrease of the interchromophore separation results in a pronounced red-shift of the absorption maximum for both molecules. Similarily, the PL spectra are shifted to the red with the decrease of separation. Both effects point toward increased intermolecular couplings[24] as the separation between the chromophors decreases.

The peak positions of the absorption and PL spectra for all studied films are summarized in Figure 5.3 as functions of the interchromophore distance. Both peak positions were determined from fitting of the 10-15% top part of the spectra with a Gaussian function. The absorption and PL maxima of TPA-2T-DCV-Me are

~0.08 eV shifted with respect to N(Ph-2T-DCV-Et)$_3$ bacause of a smaller conjugation length of the former. The absorption shift as a function of separation of ~0.07 eV is noticeably smaller than for PL (~0.3 eV) for TPA-2T-DCV-Me. This results in a graduate increase of the Stokes shift (calculated as the difference beween absorption and PL peak positions) from ~0.42 eV for diluted chromophores to ~0.6 eV for the pristine film.

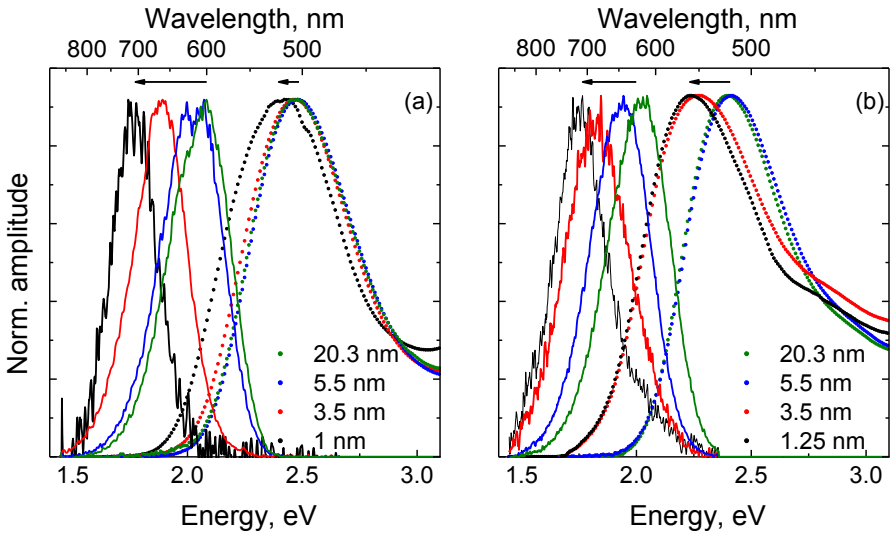

Figure 5.2 Normalized absorption (dotted lines) and PL (solid lines) spectra of the blends of (a) TPA-2T-DCV-Me and (b) N(Ph-2T-DCV-Et)$_3$ in PMMA at several representative interchromophore distances (indicated in the legends).

The results for N(Ph-2T-DCV-Et)$_3$ are somewhat different: the Stokes shift first increases, similarly to the TPA-2T-DCV-Me case, due to a stronger red shift of PL than of that of absorption. However, at the average distance of ~3.5 nm, the absorption shift catches up with PL so that the Stokes shift begins to decrease, to keep on increasing again at the intermolecular distances of ~1.2 nm. This behavior is assigned to clustering of N(Ph-2T-DCV-Et)$_3$ molecules at concentrations above 2:1 molar (4.4 nm), most probably due to π-π stacking[25].

To verify this assumption, we performed the analysis of FWHM of absorption and PL spectra for both chromophores, (Figure 5.4). For the TPA-2T-DCV-Me molecule, the widths change homogeneously with the molecular separation which is indicative of gradually increasing intermolecular interactions. In contrast, for N(Ph-2T-DCV-Et)$_3$ the absorption width remains almost constant for the distances R_{av}≥3.5 nm, and then suddenly increases from 0.6 eV to 0.75 eV. As the distance of 3.5 nm is approximately twice the lateral size of the N(Ph-2T-DCV-Et)$_3$ molecule, we assign such behavior to inhomogeneity of the system where stacked

chromophores coexist with the diluted chromophores. However, as PL from the stacked chromophores is strongly quenched (*vide infra*), the PL width does not change as PL still originates mostly from the deluted chromophores. At the shorter distances the absorption width decreases, to begin increasing again in the pristine film. All these changes correlate well with the Stokes shift irregularities highlighting the fact that the averaged separations of <3.5 nm should be taken with causion because of a clearly nongaussian distribution of the separations.

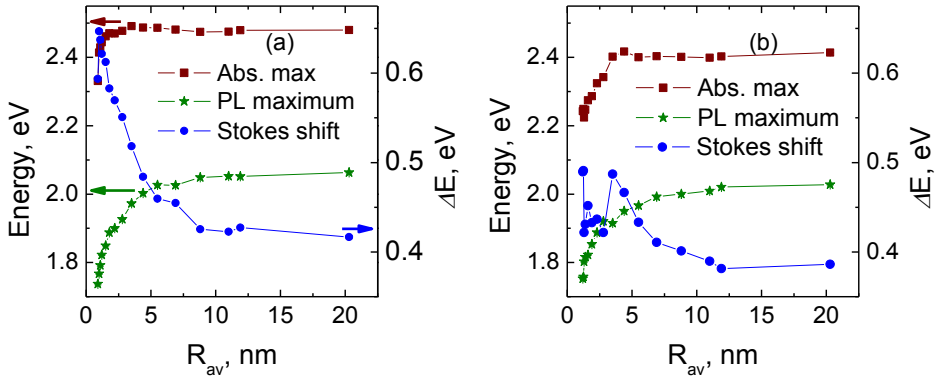

Figure 5.3 Dependence of the absorption (squares) and PL (asterisks) peak positions on the average distance R_{av} between (a) TPA-2T-DCV-Me and (b) N(Ph-2T-DCV-Et)$_3$ molecules. The Stokes shift ΔE (circles) is calculated as the difference between the two peak positions.

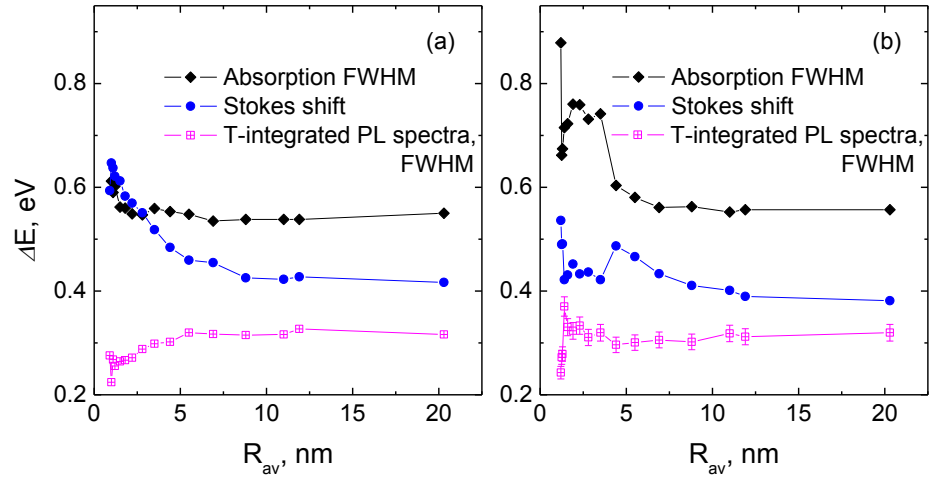

Figure 5.4 Dependence of the widths (at the half-maximum positions, FWHM) of absorption and PL spectra on the average distance between molecules R_{av} and comparison with Stokes shift magnitudes for (a) TPA-2T-DCV-Me and (b) N(Ph-2T-DCV-Et)$_3$. The Stokes shifts from Figure 5.3 are also shown for comparision

Summarizing this section, for both molecules, intermolecular interactions become noticeable at ~8-10 nm distances (i.e. where the Stokes shift ceases to be a constant) and become significant at ~4-5 nm. This agrees well with typical Förster radii[26] of small organic chromophores like dye molecules.

5.2.2 Isotropic PL transients

The isotropic (i.e. population) PL transients for both chromophores are shown in Figure 5.5 for a few representative interchromophore distances. At long distances, the relaxation dynamics are almost monoexponential, with a small contribution (~25-30% weight) of 250 ps (TPA-2T-DCV-Me) and 150 ps (N(Ph-2T-DCV-Et)$_3$) components. The latter is ascribed to a small-amplitude torsional movement of the tiophene rings and/or the dicianovinyl (DCV) acceptor end groups which is more pronounced for the larger N(Ph-2T-DCV-Et)$_3$ molecule. For shorter separations, both times accelerate while the shares of their amplitudes shift in favor of the faster component that begins to dominate in pristine films. This is assigned to the self-quenching effect.

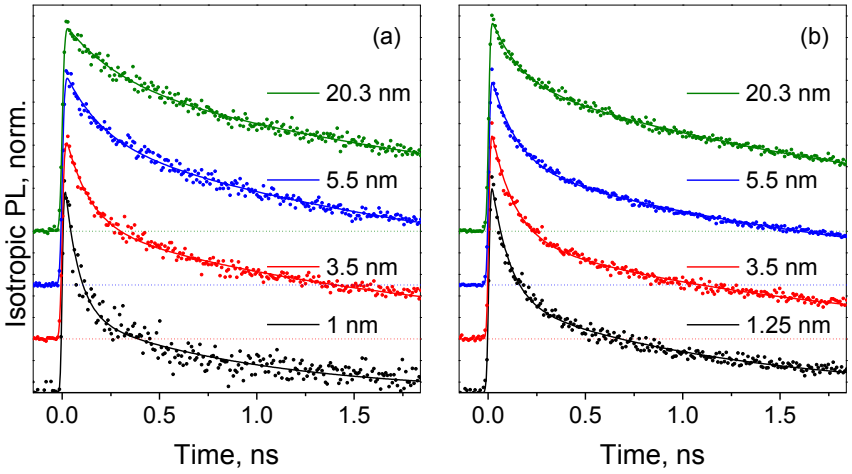

Figure 5.5 Isotropic PL transients of (a) TPA-2T-DCV-Me and (b) N(Ph-2T-DCV-Et)$_3$ samples for several representative interchromophore separations. Dots represent experimental points while the solid lines show biexponential fits convoluted with a Gaussian apparatus function of ~10 ps width. The transients are vertically offset with the dotted lines indicating the zero position.

To quantitize the relaxation dynamics, the transients for all samples were fitted with bi-exponential decay functions, convoluted with the streak-camera response; the fit parameters are shown in Figure 5.6. The population lifetime for well-separated molecules amounts to ~2.5 ns and is virtually identical for both chromophores. This time decreases to ~1 ns in the dense films which indicates that self-quenching affects the long time, too. The short-time component also

accelerates to ~50 ps with the decrease of the interchromophore distance, and its share increases to ~75%. Both effects are consistent with PL self-quenching as the excitation transferres between the chromophores. Interestingly, the fast component the N(Ph-2T-DCV-Et)$_3$ transients is less dependent on intermolecular distance because here both inter- and intra-molecular interactions contributes to the relaxation dynamics.

5.2.3 Transient anisotropy

Anisotropy transients for several representative intermolecular distances are presented in Figure 5.7. At long intermolecular distances, anisotropies for both chromophores do not change with time because the molecules cannot rotate in the solid matrix and different molecules do not communicate to each other. However, the values of anisotropies are very different. In the TPA-2T-DCV-Me case, the anisotropy amounts to r(t)≈0.4 as it should be for the anisotropic medium with random orientations of single dipoles[21,27]. In contrast, for the N(Ph-2T-DCV-Et)$_3$ molecule the anisotropy is much lower, r(t)≈0.09. This is consistent with the symmetry of the molecule as the transient dipole of the initial excitation is quickly (much faster than the experimental resolution of ~10 ps) scrambled due to intramolecular energy exchange [21,28].

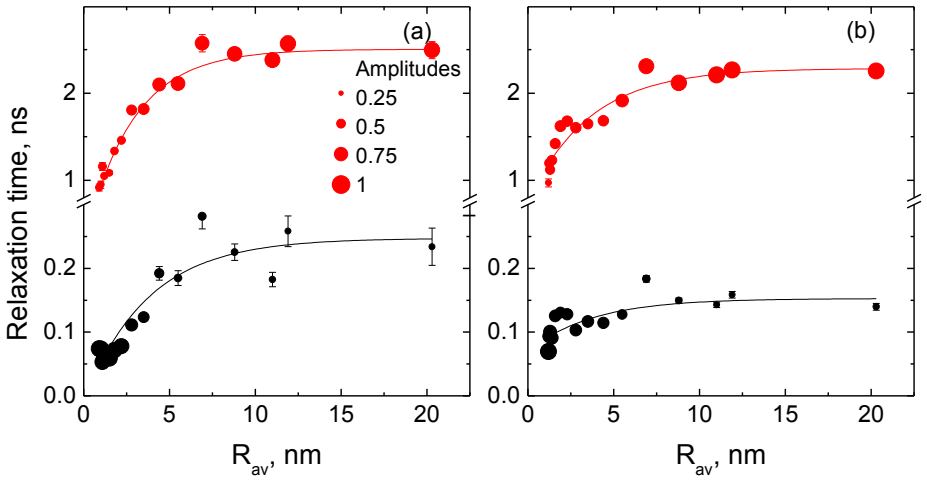

Figure 5.6 Fast (black circles) and long (red circles) time relaxation constants, obtained from the bi-exponential fit, for (a) TPA-2T-DCV-Me and (b) N(Ph-2T-DCV-Et)$_3$ samples. The relative share of each component is proportional to the size of the curcle while the sum of their amplitudes is normalized to unity. The solid lines are guides for the eye.

As the interchromophore separation decreases, the anisotropy begins to decrease in time, which is assigned to the interchromophore energy migration. The initial anisotropy value decreases (Figure 5.8), too, because of the two following

factors. First, due to energetic disorder present, the first downhill step(s) in the energy migration[29-31] becomes too fast to be captured with the 10-ps streak-camera resolution. Second, at very short intermolecular distances the chromophore coupling is so strong that delocalized states are formed with their transient dipole moment quickly scrambled, similarly to the intramolecular N(Ph-2T-DCV-Et)$_3$ case. Note that this effect is not as pronounced for the N(Ph-2T-DCV-Et)$_3$ molecule because of already-faster intramolecular dynamics.

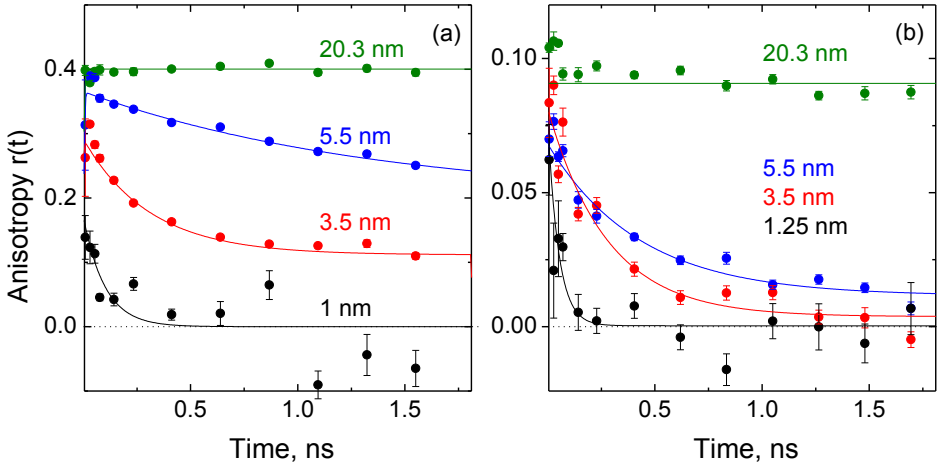

Figure 5.7 Anisotropy transients for (a) TPA-2T-DCV-Me and (b) N(Ph-2T-DCV-Et)$_3$ samples at a few representative concentrations. The monoexponential fits are shown by the solid lines.

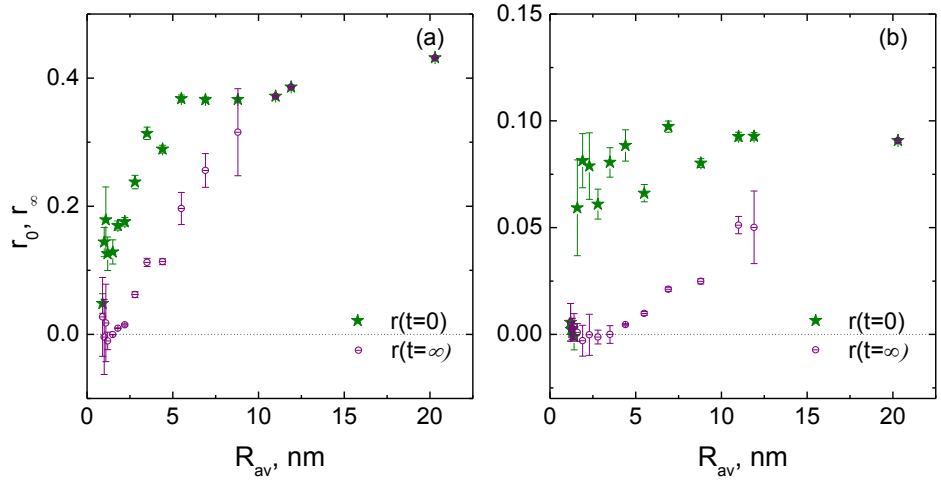

Figure 5.8 Initial r(t=0) = r_0 (asterisks) and final r_∞=r(t=∞) (circles) anisotropies for (a) TPA-2T-DCV-Me and (b) N(Ph-2T-DCV-Et)$_3$ films as functions of the average distance between the chromophores.

Figure 5.9 shows the anisotropy decay times obtained from fitting the anisotropy transients with a single exponent. Only those transients which contain a sufficient dynamical range between the short- and long-time anisotropy values were fitted as otherwise the fitting becomes unstable. The time changes from the ns range for the long chromophore separations to tens of ps range for pristine films. The decay times are similar from both chromophores which is indicative of similar exciton diffusion processes.

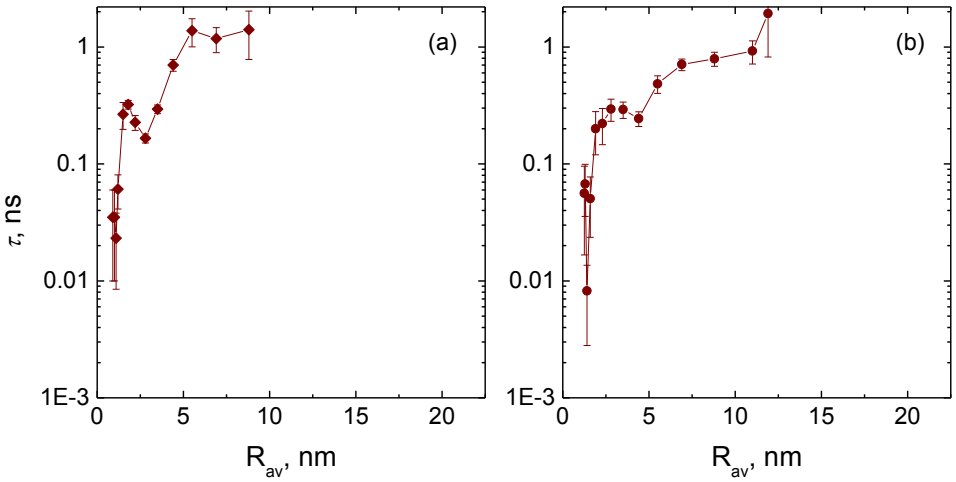

Figure 5.9 Dependence of the anisotropy decay time τ for (a) TPA-2T-DCV-Me and (b) N(Ph-2T-DCV-Et)$_3$ samples on the average distance between molecules.

5.2.4 Discussion

Figure 5.10 schematically depicts the model of exciton diffusion that emerges from our experiments. The initial photoexcitation migrates between the chromophores that are coupled via Förster-like dipole-dipole interactions. If the chromophores are far apart, the coupling that scales as R_{av}^{-6} is weak so that the excitation stays at the same molecule. The difference between the two molecules studied is that in the N(Ph-2T-DCV-Et)$_3$ case the initial excitation direction is scrambled due to intramolecular couplings between the molecular orbitals with different symmetries[21] which leads to the instantaneous (at the experimental time scale) decrease of the initial anisotropy from 0.4 to 0.09. Further on, the directions of the dipole moments do not change in time as the rotational degrees of freedom are inhibited by the solid matrix.

When the chromophore separation is decreased to $R_{av} \approx 8 - 10\,\mathrm{nm}$, the intermolecular coupling increases thereby increasing the Förster probability of the excitation to hop from one molecule to another. As the chromophores are not

aligned in the solid matrix, each hop results in changing of the dipole moment direction, which leads to anisotropy decrease in time. Simultaneously, self-quenching sets up due to final probability of the exciton to die at each hopping step, which results in acceleration of PL decay. Finally, in pristine films of the chromophores, the anisotropy decays monoexponentially to zero with the time constant of ~35 ps. Note that even faster component of the anisotropy is missed by the PL experiments because of the limited experimental resolution but can be recovered in a more complex photoinduced absorption experiment[21,30].

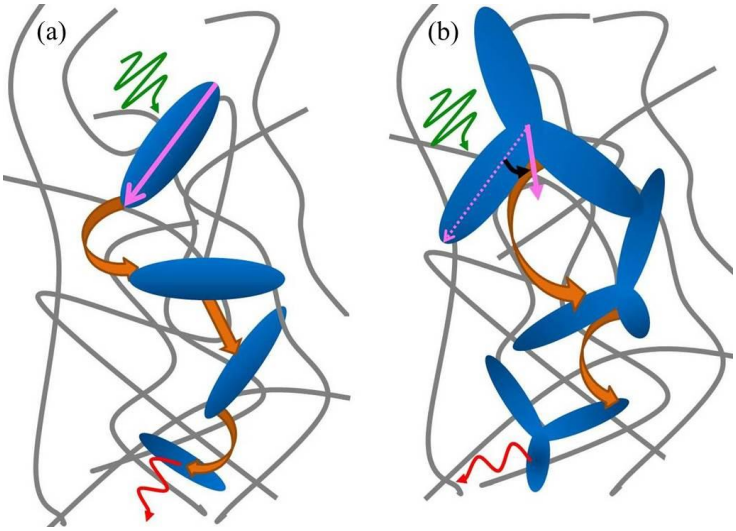

Figure 5.10 Artist representation of inter- and intermolecular anisotropy decay in solid solutions of (a) TPA-2T-DCV-Me and (b) N(Ph-2T-DCV-Et)$_3$ (blue ellipses and stars, respectively). Initial photoexcitation is shown by the green curly arrows; the transient dipole of the excited chromophore is depicted as magenta arrows. Intermolecular exciton diffusion is shown by orange arrows; PL is depicted by the red curly arrows.

5.3 Conclusions

Here we have studied *intra*- and *inter*-molecular contributions to exciton dynamics in small-molecule organic semiconductors. To reduce the *intra*molecular energy transfer occurring in the star-shaped N(Ph-2T-DCV-Et)$_3$ molecule due to its symmetrical architecture, a new molecule, TPA-2T-DCV-Me, has been synthesized. The TPA-2T-DCV-Me is a non-symmetrical analogue of N(Ph-2T-DCV-Et)$_3$ with the same donor core and acceptor end group, and as such inherits most of the photophysical properties of the later. To adjust the intermolecular interactions, the distance between the chromophores was varied by diluting them in

a solid PMMA matrix. Time-resolved PL has been used as a reporter of the photophysical processes in the films, with the isotropic transients and the transient anisotropy to obtain of the population relaxation and transient dipole moment reorientation dynamics, respectively.

The population relaxation dynamics appear to be quite similar in both chromophores. At long chromophore separations, the dynamics are dominated by the lifetime component of ~2.5 ns, with a small faster (~150 ps) contribution (~20%) assigned to twisting of the molecules in the excited state. At shorter chromophore distances, the fast component begins to prevail (~80% of the amplitude), with its time ultimately reduced to ~70 ps in the pristine films. This is assigned to the self-quenching effects that substantially reduce the exciton lifetime and therefore its diffusion length.

The anisotropy dynamics also exhibit the similar trend for both chromophores. For the well-separated chromophores, the constant anisotropies of 0.4 and 0.09 for TPA-2T-DCV-Me and N(Ph-2T-DCV-Et)$_3$, respectively, are observed. The low anisotropy in the highly symmetrical N(Ph-2T-DCV-Et)$_3$ molecule is assigned to the ultrafast intermixing of the degenerate excited, which is absent in the linear TPA-2T-DCV-Me molecule. As the average distance between chromophores decreases down to ~9 nm, the anisotropy begins to decay with the timescale dependent on the interchromophore distance. This is due to the Förster-like intermolecular energy transfer which leads to depolariation of the transient dipole moment as the exciton hopes from one molecule to another. In the densely-packed films, the intermolecular delocalization of the excited states leads to both the two-fold decrease of the initial anisotropy and substantial acceleration (to ~35ps) of the anisotropy decay.

The results presented herein highlight the importance of the chromophore chemical structure, symmetry and intermolecular interactions for the photophysical properties. Each of these parameters have been shown to be crucial for *intra*- and *inter*-molecular energy transfer and, therefore, for the exciton migration. Our findings provide important insights on the structure-property relationship of small molecules, which are of great importance for the rational material design and device engineering.

5.4 Experimental

5.4.1 Sample preparation

Synthesis of TPA-2T-DCV-Me (Figure 5.1(a)) was performed according to the approach elaborated for N(Ph-2T-DCV-Et)$_3$[22,23], using (4-

bromophenyl)diphenylamine instead of tris(4-bromophenyl)amine, and is reported in detail elsewhere[32].

For the experimental study of exciton diffusion in solid solutions, films of both small molecules in the PMMA matrix were prepared at different concentrations (from the molar ratio of 1:50 to pristine films) to control the interchromophore separation. TPA-2T-DCV-Me was dissolved in 1,2- dichlorobenzene at two concentrations of 9.6 g/L and 0.6 g/L to enable the whole range of TPA-2T-DCV-Me distances in the films. For N(Ph-2T-DCV-Et)$_3$, only one concentration of 1.2 g/L was sufficient. The matrix polymer PMMA $(C_5O_2H_8)_n$ (Sigma Aldrich, M_w=120000 g/mol) was also dissolved in 1,2-dichlorobenzene at two concentrations of 150 g/L and 9.4 g/L, again to provide the required range of the interchromophore distances. All solutions were stirred on a hot plate (50°C) of a magnetic stirrer for at least 8 hours. TPA-2T-DCV-Me and N(Ph-2T-DCV-Et)$_3$ solutions were mixed with the PMMA solution at the precalculated molar ratios (Figure 5.11). The mixtures were again stirred on a hot plate (50°C) for at least 40 minutes. The films were prepared by drop casting of 150 µL of the solution onto a microscope cover slide after which the films were left in a fume hood for at least 8 hours for complete drying. The average separation between chromophores diluted in PMMA matrix (Figure 5.11) was calculated from the molar ratios and molar volumes of the chromophores (V_m(TPA-2T-DCV-Me)=376.5 cm^3/mol, V_m(N(Ph-2T-DCV-Et)$_3$)=1015.6 cm^3/mol) and PMMA (V_m(PMMA)=100840 cm^3/mol).

5.4.2 Optical measurements

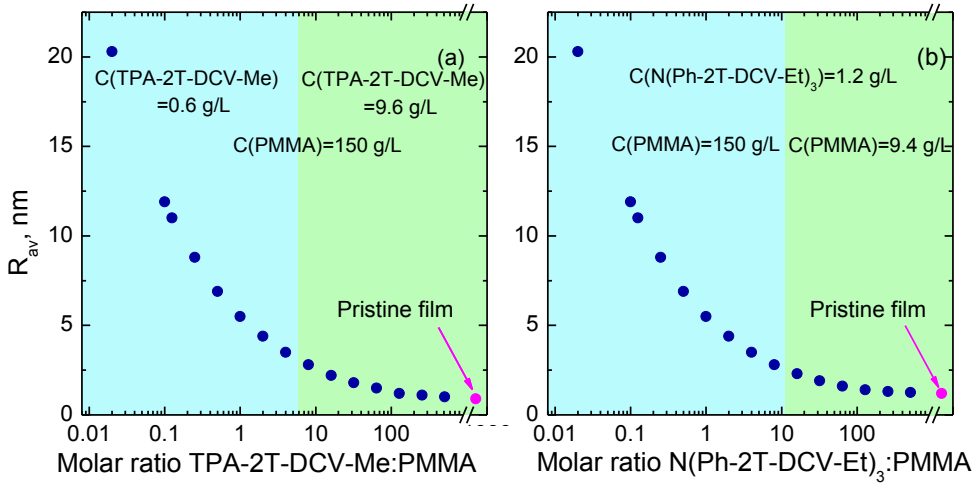

Figure 5.11 Relationship between inter-molecular distance R_{av} of the chromophores and chromophore:PMMA molar ratio. The chromophore:PMMA molar ratio varies from 1:50 to 1:0 (pristine film).

A Hamamatsu C5680 streak-camera was used to obtain the time-resolved PL kinetics (Figure 5.12). A Ti:Sapphire oscillator generated ~100 fs pulse at ~800 nm wavelength with a repetition rate of 76 MHz. The output was coupled onto the photonic crystal optical fiber (Newport, SCG-800) to generate the white-light continuum. After the fiber, a band pass filter centered at 508 nm (20 nm bandwidth) was used to select the excitation wavelength of ~2.44eV. A gradient neutral density filter was placed before the sample to attain ~2.2±0.3 μW excitation power to avoid exciton annihilation effects and sample degradation. For the latter, the excitation spot was also purged with dry nitrogen. The spectral and time resolution of the setup are ~2 nm and 10 ps, respectively.

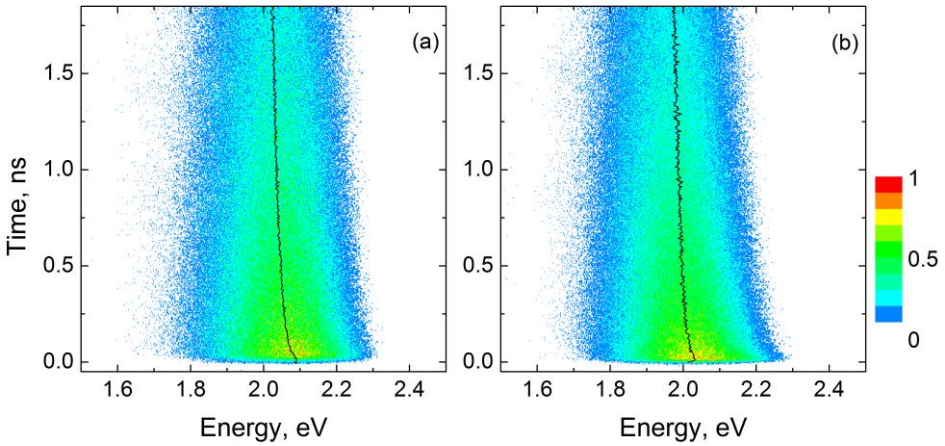

Figure 5.12 Representative 2D PL isotropic maps for (a) TPA-2T-DCV-Me and (b) N(Ph-2T-DCV-Et)$_3$ films for R_{av} = 8.8 nm. Thin black lines correspond to mean frequency.

The PL signal was collected in a 90° geometry with either perpendicular or parallel polarization directions with respect to the polarization of the excitation beam. The PL spectra were obtained by integrating of the time-resolved 2D PL maps (Figure 5.12) over time. No spectral correction for the polychromator and CCD camera was applied. The parallel $I_{\parallel}(t)$ and perpendicular $I_{\perp}(t)$ polarized transients were calculated by integrating PL maps in the 1.6-2.4 eV range. The isotropic *I(t)* and anisotropy *r(t)* transients were calculated as[33]:

$$I(t) = \frac{I_{\parallel}(t) + 2 * I_{\perp}(t)}{3} \qquad \text{(Eq. 5.1)}$$

$$r(t) = \frac{I_{\parallel}(t) - I_{\perp}(t)}{I_{\parallel}(t) + 2 * I_{\perp}(t)} \qquad \text{(Eq. 5.2)}$$

Due to slight misalignments and sample degradation between the parallel and orthogonal polarization measurements, the observed PL intensity could deviate

from the actual value by ±10%. The subsequent correction was applied if needed with the long-time anisotropy as a reference point.

Author Contributions

ES and OVK prepared the samples and performed the experiments; YNL, ANS, VYT, SAP designed and synthesized the molecules; MSP conceived and supervised the research. The manuscript was written by ES under the supervision of MSP.

5.5 References

(1) Kelley, T. W.; Baude, P. F.; Gerlach, C.; Ender, D. E.; Muyres, D.; Haase, M. A.; Vogel, D. E.; Theiss, S. D. Recent Progress in Organic Electronics: Materials, Devices, and Processes. *Chem. Mater.* **2004**, 16, 4413–4422.

(2) Brabec, C.; Scherf, U.; Dyakonov, V. *Organic Photovoltaics: Materials, Device Physics, and Manufacturing Technologies;* Wiley-VCH Verlag GmbH & Co. KGaA, Weinheim, 2011.

(3) Rand, B. P.; Richter, H. *Organic Solar Cells: Fundamentals, Devices, and Upscaling*; Pan Stanford Publishing, Stanford, 2014.

(4) Sekitani, T.; Someya, T. Stretchable, Large-area Organic Electronics. *Adv. Mater.* **2010**, 22, 2228–2246.

(5) Ni, W.; Li, M.; Liu, F.; Wan, X.; Feng, H.; Kan, B.; Zhang, Q.; Zhang, H.; Chen, Y. Dithienosilole-Based Small-Molecule Organic Solar Cells with an Efficiency over 8%: Investigation of the Relationship between the Molecular Structure and Photovoltaic Performance. *Chem. Mater.* **2015***,* 27, 6077–6084.

(6) Zhang, Q.; Kan, B.; Liu, F.; Long, G.; Wan, X.; Chen, X.; Zuo, Y.; Ni, W.; Zhang, H.; *et al*. Small-molecule solar cells with efficiency over 9%. *Nat Phot.* **2015**, 9, 35–41.

(7) An, Q.; Zhang, F.; Sun, Q.; Wang, J.; Li, L.; Zhang, J.; Tang, W.; Deng, Z. Efficient small molecular ternary solar cells by synergistically optimized photon harvesting and phase separation. *Mater. Chem. A* **2015**, 3, 16653–16662.

(8) Li, L.; Xiao, L.; Qin, H.; Gao, K.; Peng, J.; Cao, Y.; Liu, F.; Russell, T. P.; Peng, X. High-Efficiency Small Molecule-Based Bulk-Heterojunction Solar Cells Enhanced by Additive Annealing. *ACS Appl. Mater. Interfaces* **2015**, 7, 21495–21502.

(9) Bisri, S. Z.; Takenobu, T.; Yomogida, Y.; Shimotani, H.; Yamao, T.; Hotta, S.; Iwasa, Y. High Mobility and Luminescent Efficiency in Organic Single-Crystal Light-Emitting Transistors. *Adv. Funct. Mater.* **2009**, 19, 1728–1735.

(10) Hotta, S.; Yamao, T.; Bisri, S. Z.; Takenobu, T.; Iwasa, Y. Organic single-crystal light-emitting field-effect transistors. *J. Mater. Chem. C* **2014**, 2, 965–980.

(11) Komori, T.; Nakanotani, H.; Yasuda, T.; Adachi, C. Light-emitting organic field-effect transistors based on highly luminescent single crystals of thiophene/phenylene co-oligomers. *J. Mater. Chem. C* **2014**, 2, 4918–4921.

(12) Ahmad, S. Organic semiconductors for device applications: current trends and future prospects. *J. Polym. Eng.* **2014**, 34, 279-338.

(13) Kohler, A. *Electronic Processes in Organic Semiconductors: An Introduction*, Wiley-VCH Verlag GmbH & Co. KGaA, Weinheim, Germany, 2015.

(14) Schwarze, M.; Tress, W.; Beyer, B.; Gao, F.; Scholz, R.; Poelking, C.; Ortstein, K.; Günther, A. A.; Kasemann, D.; et al. Band structure engineering in organic semiconductors. *Science* **2016**, 352, 1446–1449.

(15) Torabi, S.; Jahani, F.; Van Severen, I.; Kanimozhi, C.; Patil, S.; Havenith, R. W. A.; Chiechi, R. C.; Lutsen, L.; Vanderzande, D. J. M.; *et al*. Strategy for Enhancing the Dielectric Constant of Organic Semiconductors Without Sacrificing Charge Carrier Mobility and Solubility. *Adv. Funct. Mater.* **2015**, 25, 150–157.

(16) Donaghey, J. E.; Armin, A.; Burn, P. L.; Meredith, P. Dielectric constant enhancement of non-fullerene acceptors via side-chain modification. *Chem. Commun.* **2015**, 51, 14115–14118.

(17) Scheblykin, I. G.; Yartsev, A.; Pullerits, T.; Gulbinas, V.; Sundström, V. Excited State and Charge Photogeneration Dynamics in Conjugated Polymers. *J. Phys. Chem. B* **2007**, 111, 6303–6321.

(18) Würfel, P. Photovoltaic Principles and Organic Solar Cells. *Chim. Int. J. Chem.* **2007**, 61, 770–774.

(19) Min, J.; Luponosov, Y. N.; Ponomarenko, S. A.; Ameri, T.; Li, Y.; Brabec, C. J. Interface design to improve the performance and stability of solution-processed small molecule conventional solar cells. *Adv. Energy Mater.* **2014**, 4, 1400816.

(20) Ponomarenko, S.; Luponosov, Y.; Min, J.; Solodukhin, A. N.; Surin, N.; Shcherbina, M.; Chvalun, S. N.; Ameri, T.; Brabec, C. J. Design of donor-acceptor star-shaped oligomers for efficient solution-processible organic photovoltaics. *Faraday Discuss.* **2014**, 174, 313-339.

(21) Kozlov, O. V.; Luponosov, Y. N.; Ponomarenko, S. A.; Kausch-Busies, N.; Paraschuk, D. Y.; Olivier, Y.; Beljonne, D.; Cornil, J.; Pshenichnikov, M. S. Ultrafast Charge Generation Pathways in Photovoltaic Blends Based on Novel Star-Shaped Conjugated Molecules. *Adv. Energy Mater.***2015**, 5, 1401657.

(22) Luponosov, Y. N.; Min, J.; Solodukhin, A. N.; Chvalun, S. N.; Ameri, T.; Brabec, C. J.; Ponomarenko, S. A. Design of low band gap small molecules with alkyldicyanovinyl acceptor and different donor groups for efficient bulk heterojunction organic solar cells. *SPIE Org. Photonics+ Electron.* **2015**, 9567, 95670W – 95670W.

(23) Min, J.; Luponosov, Y. N.; Ameri, T.; Elschner, A.; Peregudova, S. M.; Baran, D.; Heumüller, T.; Li, N.; Machui, F.; et al. A solution-processable star-shaped molecule for high-performance organic solar cells via alkyl chain engineering and solvent additive. *Org. Electron. physics, Mater. Appl.* **2013**, 14, 219–229.

(24) Kagan, C.; Murray, C.; Bawendi, M. Long-range resonance transfer of electronic excitations in close-packed CdSe quantum-dot solids. *Phys. Rev. B* **1996**, 54, 8633–8643.

(25) Hunter, C. A.; Sanders, J. K. M. The nature of π-π interactions. *J. Am. Chem. Soc.* **1990**, 112, 5525–5534.

(26) Raymo, F. M.; Yildiz, I. Luminescent chemosensors based on semiconductor quantum dots. *Phys. Chem. Chem. Phys.* **2007**, 9, 2036–2043.

(27) Ripaud, E.; Olivier, Y.; Leriche, P.; Cornil, J.; Roncali, J. Polarizability and internal charge transfer in thiophene-triphenylamine hybrid π-conjugated systems. *J. Phys. Chem. B* **2011**, 115, 9379–9386.

(28) Gurzadyan, G. G.; Soci, C.; Lanzani, G. *Ultrafast Dynamics in Molecules, Nanostructures and Interfaces*, World Scientific Publishing Company, Singapore, 2014; pp 169-182.

(29) Menke, S. M.; Holmes, R. J. Energy diffusion in organic photovoltaic cells. *Energy Environ. Sci.* 2014, 7, 499-512.

(30) Mikhnenko, O. V.; Blom, P. W. M.; Nguyen, T.-Q. Exciton diffusion in organic semiconductors. *Energy Environ. Sci.* **2015**, 8, 1867-1888.

(31) Akselrod, G. M.; Prins, F.; Poulikakos, L. V.; Lee, E. M. Y.; Weidman, M. C.; Mork, A. J.; Willard, A. P.; Bulović, V.; Tisdale, W. A. Subdiffusive exciton transport in quantum dot solids. *Nano Lett.* **2014**, 14, 3556-3562.

(32) Kozlov, O. V; Liu, X.; Luponosov, Y. N.; Solodukhin, A. N.; Toropynina, V. Y.; Min, J.; Buzin, M. I.; Peregudova, S. M.; Brabec, C. J.; Ponomarenko, S. A.; et al. Triphenylamine-Based Push-Pull Molecule for Photovoltaic Applications: From Synthesis to Ultrafast Device Photophysics. *J. Phys. Chem. C* **2017**, 121, 6424–6435.

(33) Joseph R. Lakowicz. *Principles of Fluorescence Spectroscopy, 3rd edition*; Springer, New York, 2006, pp 383-412.

Summary

We are surrounded by all kinds of materials. Some of the materials are artificial and some of them are created by nature. Regardless of the origin, all materials consist of atoms, which are bound together to form molecules. There are two types of interactions which can be found at this level: intra- and intermolecular. The understanding of processes occurring during intra- and intermolecular interactions are indispensable for predicting the material properties and for designing the new materials.

In the current work, we address the following question: what kind of interactions – intra- and/or intermolecular ones – determine dynamical properties (e.g., hydrogen-bonding dynamics, energy transfer, exciton diffusion) in different materials such as liquids and solid films. Here we consider the intra- and intermolecular interactions as “conversations” between different vibrational or electronic transitions within one molecule (*intra*molecular) and/or between different molecules (*inter*molecular). Due to impressive advances in experimental physical chemistry, there are a number of tools for obtaining the dynamical and structural information on different timescales. However, the previous studies on liquids and films showed the importance of hydrogen-bonding dynamics, energy transfer and exciton dynamics on femto- (1 fs=10^{-15} s) to nanosecond (1 ns=10^{-9} s) timescales. The most suitable (and often the only) tool for probing such fast structural and dynamical information is ultrafast spectroscopy.

The general principle of ultrafast spectroscopy is the following: the first pulse (the pump) brings the system out of equilibrium, while the second, delayed pulse probes the occurred changes. These changes might be any: changes in absorption, luminescence, reflection, diffraction etc.; here we are mostly concerned with the first two. By measuring such changes as a function of the delay between the pump and the probe pulses, one can determine the timescales of the intra- and intermolecular dynamical processes. To distinguish between intra- and intermolecular contributions, the distance between interacting molecules is varied from densely packed molecules (such as, for instance, in liquids or solid-state films) to spatially-separated molecules (such as in diluted solutions or solid matrices). The spectral signatures obtained experimentally are then confronted with the outcome of theoretical calculations, which opens the way towards unraveling dynamics at the molecular scale.

In the first part of the Thesis, vibrational two-dimensional infrared (2D-IR) spectroscopy (infrared means that the vibrational levels are excited and probed, Figure 1) is used for understanding the dynamical properties of hydrogen-bonded

liquids. The second part of the current work is devoted to the electronic dynamics in novel star-shaped molecules, which have a great potential for modern organic solar cells. As a research tool, time-resolved photoluminescence spectroscopy is used where the pump pulse excites electronic transitions and the resulting photoluminescence is monitored (Figure 1).

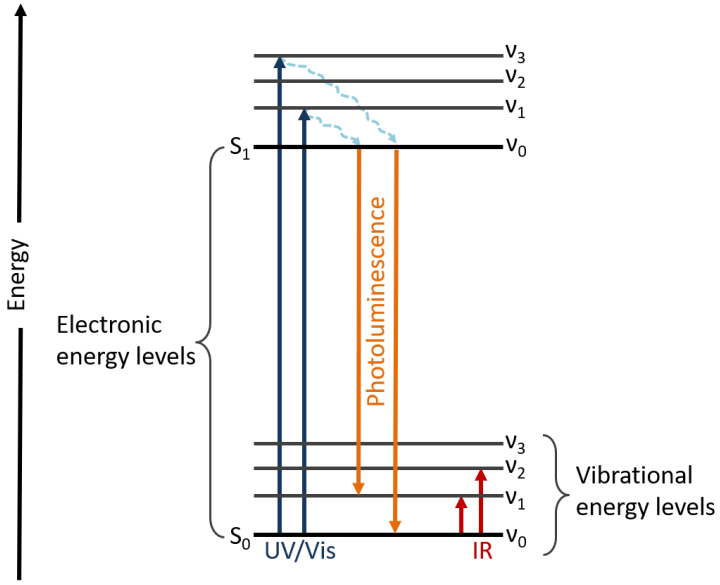

Figure 1 Energy levels diagram of a molecule, where S_n and V_n denote the electronic and vibrational energy states. The red arrows denote vibrational transitions due to absorption of infrared (IR) light; the dark blue arrows correspond to electronic transitions (as the result of absorption of UV/Vis light); the light blue arrows show vibrational relaxation; the orange arrows correspond to the photon emission process (luminescence).

The first system of our interest in Chapter 2 is a model system for an important type of proteins, the so-called intrinsically disordered proteins (IDPs). IDPs are characterized by low structural stability, which allows fast changes between different conformations, that in turn are critical for IDPs' function. The main question of the study is the following: what kind of structures dominates in the model system and how these structures influence intermolecular energy transfer. For mimicking the IDPs structure we – as many others before us – use liquid N-methylacetamide (NMA). The NMA molecule contains a single peptide unit (-CONH-), which is characteristic for all protein structures including those of IDPs. Therefore, NMA molecules interact with each other in a similar way to IDPs. Experimental studies combined with molecular dynamics simulations show fascinating results. Typically, liquids are characterized by high disorder: the molecules librate, rotate, and diffuse all the time. However, in the liquid NMA the

molecules tend to form well-organized structures. The most populated structure looks like a chain of hydrogen-bonded NMA molecules. These structures facilitate intermolecular vibrational energy transfer where the initial IR excitation moves along the hydrogen-bonded chains. Therefore, we can assume that disordered amino acids within IDPs structure tend to form the similar structures, which in turn are preferable for intermolecular energy transfer.

In Chapter 3 we modify the system to make it more relevant to the biological situation: proteins in a water environment. For this, we dissolve NMA molecules in water. In contrast to hydrogen-bonded chains of NMA molecules in the condensed phase, NMA molecules in water tend to form clusters with a hydrophobic core and hydrophilic surface (also known as “hydrophobic collapse”). Moreover, unlike the well-defined pathways of energy migration in bulk NMA (along the hydrogen-bonded chain of NMA molecules), the pathways in the NMA-water mixture have a more stochastic character. The insights gained in this chapter may be of assistance for unraveling the energy transfer pathways as well as preferred structures in biological systems, like proteins surrounded by water.

Chapter 4 concerns another type of basic hydrogen-bonded liquids, the alcohols. Earlier studies on pure alcohols and alcohol clusters showed a strong correlation between dynamical timescales of hydrogen bonding and the size of the alcohol molecules: the larger molecules possess slower dynamics. However, because of the coexistence of intra- and intermolecular interactions in such systems, it was not clear which type of interactions dominates the hydrogen bonding dynamics. We exclude the intermolecular interactions between alcohol molecules by strongly diluting them in a hydrogen bond accepting solvent (acetonitrile). Acetonitrile is chosen (and proven) to prevent clustering of the alcohol molecules at low concentrations. The obtained results show that all studied alcohol-solvent systems, where the solvent is the same and the only difference in interactions is in the intramolecular interactions within the alcohol molecules, have similar dynamics independently of the size of alcohol molecules. Therefore, we conclude that all the observed differences in hydrogen bond dynamics in the pure alcohols and/or alcohol clusters resulted from intermolecular interactions between alcohol molecules. The obtained results are interesting for unraveling the contribution of intra- and intermolecular interactions to hydrogen bonding dynamics in other hydrogen-bonded liquids in bulk and diluted phases.

The last chapter is devoted to the study of exited-state dynamics in solid films, which are based on the star-shaped molecule (SSM) N(Ph-2T-DCV-Et)$_3$ and its linear analog TPA-2T-DCV-Me. These two molecules are used in research solar cell devices with energy conversion efficiencies approaching 6%. The SSM has a

symmetrical shape which facilitates ultrafast energy transfer within the molecule. To circumvent the intramolecular interactions, we studied a linear analog of SSM, which was synthesized in the Institute of Synthetic Polymeric Materials (Russian Academy of Sciences). The intermolecular interactions are controlled by dissolving the two molecules in a solid matrix of acrylic glass (Poly(methyl methacrylate), $(C_5O_2H_8)_n$) at different concentrations. Photoluminescence experiments on the films show that both intra- and intermolecular interactions in SSM are crucial for energy transfer and exciton dynamics. The obtained results help to understand the influence of molecular structure on dynamical properties that in turn can be used for molecular design and further optimization of the efficiency of organic photovoltaic devices.

To summarize, we have studied the interplay of intra- and/or intermolecular interactions in several liquid and solid materials. This work forms a convenient basis for predicting dynamical and structural properties of more complex (bio)molecular systems such as DNA, proteins, and hydrogen-bonded liquids. Furthermore, the obtained results are instrumental in designing new molecules for organic electronics applications.

Samenvatting

We zijn omgeven door allerlei soorten materialen. Sommige van deze materialen zijn kunstmatig, andere van natuurlijke oorsprong. Maar alle materialen bestaan uit atomen, die, samengebonden, moleculen vormen. Er zijn twee soorten interacties mogelijk op dit niveau: intra- en intermoleculaire interacties. Het begrijpen van de processen die gebeuren tijdens intra- en intermoleculaire interacties, is onmisbaar voor het voorspellen van de materiaal eigenschappen en voor het ontwerpen van nieuwe materialen.

In dit proefschrift behandelen we de volgende vraag: welk soort interacties – intra- en/of intermoleculair – bepalen de dynamische eigenschappen (bv waterstofbrug dynamica, energie overdracht, exciton diffusie) in verschillende materialen, zoals vloeistoffen en dunne vaste-stof lagen. Hier beschouwen we de intra- en intermoleculaire interacties als “gesprekken” tussen verschillende vibratie en electronische overgangen, binnen één molecuul (*intra*moleculair) en/of tussen verschillende moleculen (*inter*moleculair). Door de indrukwekkende voortgang in de experimentele fysische chemie, zijn er een aantal middelen beschikbaar voor het verkrijgen van dynamische en structurele informatie op verschillende tijdschalen. Echter, voorgaande studies hebben het belang laten zien van waterstofbrug dynamica, energie overdracht en exciton diffusie op femto- (1 fs = 10^{-15} s) en nanoseconde (1 ns = 10^{-9} s) tijdschalen. Ultrasnelle spectroscopie is de meest geschikte (en vaak enig mogelijke) manier om informatie te verkrijgen over zulke snelle structurele en dynamische processen.

Het algemene principe van ultrasnelle spectroscopie is het volgende: de eerste lichtpuls (de pomp) brengt het systeem uit evenwicht, de tweede vertraagde lichtpuls (de probe) meet vervolgende de opgetreden veranderingen. Deze veranderingen kunnen van alles zijn: veranderingen in absorptie, luminescentie, reflectie, diffractie etc. Hier houden we ons voornamelijk bezig met de eerste twee. Door deze veranderingen te meten als functie van de tijdsduur tussen de pomp en de probe puls, kunnen we de tijdschalen bepalen van de intra- en intermoleculaire processen. Om onderscheid te kunnen maken tussen intra- en intermoleculaire bijdrages aan deze veranderingen, wordt de afstand tussen de interacterende moleculen gevarieerd van dicht opeengestapelde moleculen (zoals bv in pure vloeistoffen en vaste-stof dunne lagen) tot ruimtelijke gescheiden moleculen (zoals in verdunde oplossingen of matrices). De experimentele informatie die zo door spectroscopie wordt verkregen, wordt vergeleken met de uitkomsten van theoretische berekeningen; dit opent zo de deur om de dynamica op een moleculaire schaal te ontrafelen.

In het eerste deel van dit proefschrift wordt vibrationele twee-dimensionale infrarood (2D-IR) spectroscopie gebruikt, om de dynamische eigenschappen te kunnen begrijpen van vloeistoffen met moleculen met waterstofbruggen. Infrarood betekend hier dat de vibratie niveaus worden geëxciteerd en geprobed, zie Figuur 1. In het tweede deel wordt aandacht besteed aan de elektronische dynamica van nieuwe ster-vormige moleculen, die grote potentie hebben voor moderne organische zonnecellen. Als instrument wordt hierbij tijds-opgeloste fotoluminescentie spectroscopie gebruikt, waarbij met de pomp elektronische toestanden worden aangeslagen en waarvan vervolgens de fotoluminiscentie wordt bestudeerd (Figuur 1).

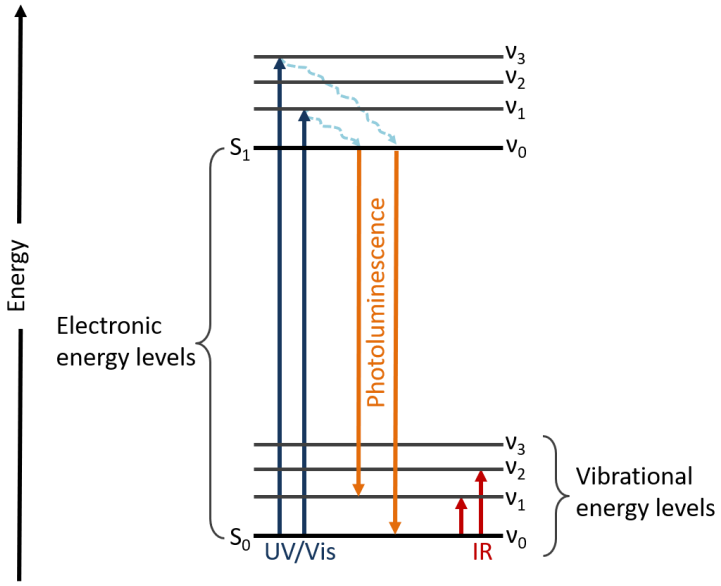

Figuur 1 Energieniveaus van een molecuul, waar S_n en V_n de elektronische en vibratie energieniveaus aanduiden. De rode pijlen zijn de vibratie overgangen door absorptie van infrarood (IR) licht; de donkerblauwe pijlen corresponderen met elektronische overgangen (door absorptie van UV/zichtbaar licht); de lichtblauw pijlen zijn vibratie relaxaties. De oranje pijlen zijn foton emissies (luminiscentie).

Het eerste systeem waar we in geïnteresseerd zijn in hoofdstuk 2, is een model systeem voor een belangrijke klasse van eiwitten, de zogenaamde intrinsiek ongeordende eiwitten (IOE). IOE's worden gekenmerkt door een lage structurele stabiliteit, wat snelle veranderingen tussen verschillende conformaties mogelijk maakt, wat cruciaal is voor de functionaliteit van IOE's. De belangrijkste vraag van dit onderzoek is welke structuur het meest voorkomt in het modelsysteem en hoe deze structuren van invloed zijn op de intramoleculaire energieoverdracht. Om de structuur van IEO's na te bootsen, gebruiken we – zoals velen voor ons – vloeibaar N-methylacetamide (NMA). Een NMA molecuul bevat een enkele peptide eenheid

(-CONH-) die karakteristiek is voor alle eiwit structuren, inclusief de IOE's. Daardoor interacteren NMA moleculen op eenzelfde manier als IOE's. Experimenteel onderzoek, gecombineerd met moleculaire dynamica simulaties, laten fascinerende resultaten zien. Normaal zijn vloeistoffen erg ongeordend: de moleculen libreren, roteren en diffunderen de hele tijd. In vloeibaar NMA hebben de moleculen echter de neiging om goed geordende structuren te vormen. De meest voorkomende structuur lijkt op een keten van NMA moleculen, verbonden door waterstofbruggen. Deze structuur is goed voor intramoleculaire vibratie energie overdracht, waarbij de initiele infrarood excitatie zich beweegt langs de keten van door waterstofbruggen verbonden NMA moleculen. Hierdoor kunnen we aannemen dat ongeordende aminozuren in IEO structuren de neiging hebben om soortgelijke structuren te vormen, die goed zijn voor intramoleculaire energieoverdracht.

In hoofdstuk 3 veranderen we het NMA systeem om het meer relevant te maken voor biologische situaties: eiwitten in een waterige omgeving. Hiervoor lossen we NMA moleculen op in water. In kontrast met de ketens van door waterstofbruggen verbonden NMA moleculen in de pure vloeistof, hebben NMA moleculen in water de neiging om clusters te vormen, met een hydrofobe kern en een hydrofiel oppervlak (staat ook bekend als "hydrofobe instorting"). Bovendien vormen de paden voor energieoverdracht in een NMA-water mengsel een meer grillig patroon; dit in tegenstelling tot de goed-gedefinieerde paden in puur NMA, langs de ketens. De in dit hoofdstuk verkregen inzichten kunnen behulpzaam zijn bij het ontrafelen van energie overdracht paden in biologische systemen zoals eiwitten omringd door water, alsmede hun voorkeurs structuren.

Hoofdstuk 4 bekijkt een ander type van door waterstofbruggen verbonden moleculen, namelijk de alcoholen. Eerder onderzoek aan pure alcoholen en alcohol clusters heeft een sterke correlatie laten zien tussen de dynamische tijdschalen van waterstofbrug verbindingen en de grootte van de alcohol moleculen: de grotere moleculen vertonen een langzamere dynamica. Echter, door de co-existentie van intra- en intermoleculaire interacties in zulke systemen, was het niet duidelijk wat de belangrijkste interactie was in de waterstofbrug dynamica. We hebben de intermolekulaire interactie tussen de alcohol moleculen uitgesloten, door ze sterk te verdunnen in een waterstofbrug-accepterend oplosmiddel (acetonitrile). We gebruiken acetonitrile omdat dit (bewezen) clustering voorkomt van alcohol moleculen bij lage concentraties. De verkregen resultaten laten zien dat voor alle bestudeerde alcohol-oplosmiddel systemen (waar het oplosmiddel hetzelfde is en het enige verschil in interactie de intramoleculaire interactie binnenin de alcohol moleculen is), de dynamica overeenkomt, onafhankelijk van de grootte van de alcohol moleculen. We concluderen daarom dat alle geobserveerde

verschillen in waterstofbrug dynamica in pure alcoholen en/of alcohol clusters het resultaat is van intermoleculaire interacties tussen de alcohol moleculen. De verkregen resultaten zijn interessant om de bijdragen van intra- en intermoleculaire interacties aan de waterstofbrug dynamica te ontrafelen voor andere door waterstofbruggen verbonden vloeistoffen, zowel puur als verdunt.

Het laatste hoofdstuk is gewijd aan het bestuderen van de aangeslagen toestand dynamica in dunne films die het ster-vormige molecuul (SVM) N(Ph-2T-DCV-Et)$_3$ bevatten, of het lineaire analoog TPA-2T-DCV-Me. Deze twee moleculen worden gebruikt in research zonnecellen, met een energie conversie efficiëntie die de 6% benadert. Het SVM molecule heeft een symmetrische vorm, wat een ultrasnelle energie overdracht binnenin het molecuul vergemakkelijkt. Om de intramoleculaire interacties te omzeilen, hebben we het lineaire analoog van de SVM bestudeerd. Dit is gesynthetiseerd in het Institute of Synthetic Poymeric Materials (Russian Academy of Sciences). De intermoleculaire interacties worden gecontroleerd door de twee moleculen op te lossen in een vaste matrix van acryl glas (Poly(methyl) methacrylate, $(C_5O_2H_8)_n$) met verschillende concentraties. Fotoluminescentie experimenten aan deze films laten zien dat zowel intra- als intermoleculaire interacties in SVM's cruciaal zijn voor de energie overdracht en de exciton dynamica. De verkregen resultaten helpen om te begrijpen wat de invloed van de structuur van moleculen is op de dynamische eigenschappen. Dit kan dan gebruikt worden voor het moleculaire ontwerp en verdere verbetering van de efficiëntie van organische fotovoltaische devices.

Samenvattend hebben we de wisselwerking bestudeerd van intra- en/of intermoleculaire interacties in verscheidene vloeibare en vaste materialen. Dit werk vormt een geschikte basis om de dynamische en structurele eigenschappen te voorspellen van meer complexe (bio)moleculaire systemen, zoals DNA, eiwitten en vloeistoffen met waterstofbruggen. Verder zijn de verkregen resultaten belangrijk voor het ontwerpen van nieuwe moleculen voor organisch-elektronische toepassingen.

Acknowledgements

Looking back to 2013, I remember my first impression of the Netherlands when I came for an interview: a lot of flat and green fields, many cows and warm sun. I managed to catch all sunny days of that summer and when someone told me that it is usually rainy, cloudy or windy, I surely did not believe it (yes, I was naïve). Now I even cannot count how many times I was completely wet or gave up to cycle against the wind. However, I have pleasant memories about my stay in Groningen, because all these years I was surrounded and supported by amazing people, who made my PhD life interesting and exciting.

First of all, I would like to thank Professor Maxim Pshenichnikov. Maxim, thank you for giving me an opportunity to be a part of the OCMP group. As some may remember, I was supposed to work on the project entitled “Channel Proteins seen through Multidimensional IR Spectroscopy”. Five years ago I was able to synthesize a protein for this project and you promised to teach me spectroscopy. Now I have no clue about protein synthesis, but I feel confident in laser labs. Under your guidance, I learned a lot of stuff not only about science but also about daily life. Truly speaking I cannot find the right words to express my gratitude for your help and support during my PhD. Thank you.

I want to thank my co-promotor Thomas La Cour Jansen for showing and explaining to me the world of theoretical calculations. They were very helpful for understanding what exactly happens in our systems. Without your guidance, a sufficient amount of this thesis would not exist.

Next, I wish to acknowledge the members of the reading committee: Ronnie Hoekstra, Huib Bakker and Klaas Wynne. Thank you very much for your help and the time you spent to read and assess my thesis.

Each chapter of this thesis is a result of close collaboration. Therefore, I want to thank my collaborators. Thomas L.C. Jansen and Ana Cunha, I cannot imagine my papers and thesis without your theoretical calculations, models, and our discussions. Sander Woutersen, Robbert Bloem and Steven Roeters, thank you for hosting me in your lab to perform the NMA experiments. I would like to thank Sergey Ponomarenko and his group for synthesizing the molecules, which were studied in the last chapter.

Coming back to the OCMP group. Ron, thank you for everything, I still keep your painted flowers. I really miss our small talk and non-scientific conversations. I wish you all the best in America and hopefully we will have a chance to meet again.

Any scientific group is a complicated mechanism and there are people, who maintain the most important aspects. I am talking about technicians and secretaries. All credit for the beautiful 2D spectra and their analysis in this book goes to our technician Foppe de Haan. Foppe, your software is great! It helped to get my degree in 5 years instead of 7 (or even more). I am so grateful for your instant help with everything (my setup, computer, software, macros, translation to/from Dutch and I can continue this list for another 17 pages). Ben, under your supervision I built my first laser setup, it was an amazing experience. Jeannette, you guided me through paperwork during the hiring process and in spite of the fact that you are not a secretary of OCMP group for the last 4 years, I could always ask for your advice and help. Henriet, I admire your competence and willingness to help, thank you for the help with paperwork, conferences, and administrative support. In short, I am very glad to work in the same group with all of you.

Next, I want to thank all members (former and current) of the OCMP group. Almis and Katya, you showed me how many activities I can find in Groningen. Vlad, we never worked together, however, we crossed at different events. Toni, you are a super positive and smart guy, it was a pleasure to share the office with you. Keisuke, thank you for the help with super complicated 2D-IR setup. Qi, it was nice knowing you and your family. Björn, thank you for supporting any crazy idea (like visiting the funfair, going to pool or stealing a bottle of wine from FOM's dinner), I really enjoyed our time together and our scientific and non-scientific discussion. I hope we will be in touch in the future. Nilesh, thanks for the positive atmosphere during coffee breaks and lunches. Chia-Lin, thanks to you I know many things about Taiwan and Taiwanese people, good luck with the defense! Sonya, I am very happy that we shared the office during your short project. I think it was a good start for our friendship and I strongly believe that I will visit you in Japan sometime. Jan, you are a great guy; you laughed at my jokes and you liked them (at least I have no reason to doubt), so I like you:))) Anna, Timen, Ronnie and Kevin, thank you for being a part of the OCMP group and for the time we spent together. Nong and Benedito, unfortunately, I had no chance to know your better, but I am sure that you will enjoy your time in Groningen.

From the faculty of Science and Engineering I want to thank Aisha, Jamo, Leonid, Vova, Artem, Kumar, Laaya, Anna B., Ana C., Edita, Marianna, Megan, Vakeel, Alisa, Valentina, Fabiola, Tiago, Ruslan, Sampson, Mustapha, Jorge, Arunesh (sorry, if I forgot someone) for their support and all small talk in corridors and cafeteria.

A special thanks goes to Top Master Nanoscience 2013-2015 cohort: Natasha, Wytse, Xu, Dima, Sasha, Tenzin, Arijit, Jing, Xinkai, Hendrik, Azadeh, Chen,

Henrieke and Geert. Going back to 2013, I was sure that master's exams were the last exams in my life (remember, that I was naive back then). Thank you for the help with preparation for the characterization of nanomaterials tests and for everything after that: dinners, parties, BBQ and coffee meeting. All of you are cool and wonderful people, so I even feel happy that I had to pass all four exams together with you. Thank you for being my friends and support during these 5 years and special thanks to my paranymph Natasha.

Another amazing group of people in my life is tennis team SPR mix 2. Ger, Richard, Georgette, Mia, Cristina, Stefano and Peter, there are not enough words to express my happiness to be your teammate. We spent eight Saturdays together under rain, sun, and wind playing tennis and at least one Sunday eating a nice dinner; I appreciate every day that we spent together. Thank you for all your support, positive and "Davai, davai", when I needed it. Thanks for the interesting stories and sharing your life experience with me. Unfortunately, I will not play competition with you again (but who knows, never say "never"), but I will do my best to support you next year! And thanks to the tennis section for SPR mix 1 and other people, with whom I played during those three years.

I want to thank SPR tennis not only for team SPR-mix 2 but also for Anastasia. Nastya, we met during a tennis practice and I consider that day as a start point of our friendship. We come from the same region, you visited my hometown; I think that is the reason why we have a lot of in common. Thank you for sharing your knowledge about the gastronomic world of Groningen and for typical girl's pastime: shopping. If you move to London, then wait for me to visit.

This part I will write briefly, otherwise, it will take another one hundred pages. Oleg, Julius and Arthur, we are OCMP team colleagues who became close friends. Julius, you are the first person with whom I talked in the group. On the first day, we discussed Claude Monet and Édouard Manet, on the other days we discussed everything in this world. Thank you for being the best office mate in my PhD life and being my friend beyond our office. I know, that you will find the right words and advice for me at any time. Oleg, we started out PhD on the same day. Truly speaking, I am disappointed, that we will not become Drs on the same day… We spent so much time together just walking, talking, doing something new in our lives (like playing in the casino on Christmas eve). I really miss all of it. Arthur, a couple of weeks we lived together, we went to dance classes together, we played tennis together, and as a decent man, you have to marry me after all this :). Anya, you are not a physicist at all, however, you became an integral part of our group. Since the first day of our acquaintance, I cannot stop to admire your positivity and love of life. I wish you and your husband all the best. Guys, thank you for being with me almost

till the end of my PhD, thank you for the support and all life experience I got. And many thanks to the Internet, because we can stay in touch.

Katya, we did our master projects at the same group, however, to become real friends we needed to move to different countries. I am a very lazy person; however, I was ready to travel 4.5 hours one way to Hannover for spending a weekend with you (you did the same, but you are not lazy at all). Thank you for these weekends, thank you for the trips to Germany and Austria. And I do not think that I can find the proper words to express my gratitude for everything you did for me. I am happy to be your friend!

Lena and Masha, our friendship dates back to 2012, when we started to live together in a student house. You are the best neighbors I can imagine. After six years, we are still in touch and I cannot imagine my life without you. Lena, you became my closest and dearest friend. Thank you for supporting me in anything and anywhere! I know, that it was a perfect match). Masha, I like your creativity and kindness to me and as I told before you are the best neighbor and friend I can imagine). Thank you for all dinners and talks, with you I am a happy 22-year old girl again.

Asya and Vera, you are not only the best doctors I know but also great friends. Thank you for all our meetings in Volgograd and Moscow, for coffees and pizzas. With you I forget about all worries and problems as it was in 2007 when we met in “Integral”.

The last parts of my acknowledgments I want to devote to the most special people in my life. Vanya, I cannot thank you enough for all of your love and support. It means the world to me. You knew about all my ups and downs and despite anything you believed in me. Without you I would never have finished my PhD and this book. I am happy next to you and I am grateful to our alma mater for our meeting.

Finally, I would like to thank my family for their support. Дорогая моя семья, эту книгу я посвящаю вам! Я это редко говорю, но я вас всех очень люблю, хоть мы все и безумно разные. Саша, ты до сих пор выполняешь обязанности старшего брата- спасибо тебе за это. Огромное спасибо тебе и твоей жене Люде за все наши встречи в Волгограде и спасибо за маленькую Анну Александровну, которую я безгранично люблю и на правах тети могу баловать и поучать. Вика, любимая сестра, ты самый что ни на есть человек, который втянул меня в это PhD. Ты нашла данную позицию и замотивировала попробовать свои силы. В итоге все получилось, как и другие вещи, за которые ты берешься. Отбрось сомнения, сестра! Дима, младший брат, в тебе столько мудрости и основательности, что я порой сомневаюсь, что ты

младший из нас четырех. Спасибо тебе за все, я уверена, что тебя и Альбину ждет счастливая и долгая семейная жизнь. Братья и сестра простите за мои косяки в детстве и юношестве. Отец, без тебя не было бы меня.

Мама! Порой кажется, что всех слов мира мало, чтобы описать, как ты для меня дорога. С первых дней жизни ты поддерживала мои стремления и мой выбор. Ты верила в меня тогда, когда у меня опускались руки. И все мои заслуги, включая эту книгу и степень, были бы невозможны без тебя. Я не знаю, куда занесет меня судьба, но я знаю, что ты всегда будешь рядом. Спасибо тебе за всё!